OPTIMIZATION PROCESS FOR CONFIGURATION OF FLEXIBLE JOINED-WING

THESIS

Cody C Rasmussen, Captain, USAF
AFIT/GAE/ENY/04-M14

DEPARTMENT OF THE AIR FORCE
AIR UNIVERSITY

AIR FORCE INSTITUTE OF TECHNOLOGY

Wright-Patterson Air Force Base, Ohio

AFIT/GAE/ENY/04-M14

OPTIMIZATION PROCESS FOR CONFIGURATION OF FLEXIBLE JOINED-WING

THESIS

Presented to the Faculty

Department of Aeronautics and Astronautics

Graduate School of Engineering and Management

Air Force Institute of Technology

Air University

Air Education and Training Command

In Partial Fulfillment of the Requirements for the

Degree of Master of Science in Aeronautical Engineering

Cody C Rasmussen, BS

Captain, USAF

March 2004

AFIT/GAE/ENY/04-M14

OPTIMIZATION PROCESS FOR CONFIGURATION OF FLEXIBLE JOINED-WING

Cody C Rasmussen, B.S.

Captain, USAF

Approved:

Robert A. Canfield Thesis Advisor	Date
Anthony N. Palazotto Committee Member	Date
Joerg D. Walter Committee Member	Date

AFIT/GAE/ENY/04-M14

Abstract

This study established a weight optimized configuration design of a joined-wing sensor-craft. The joined-wing aircraft concept fulfills a proposed long-endurance surveillance mission that contains an antenna structure embedded in the wing skin. The analysis was completed utilizing structural optimization, aerodynamic analyses, and response surface methodology.

A sample of 74 joined-wing configurations were weight optimized. Each optimized structure was determined through a change of skin, spar, and rib thickness in the wing box by determining trimmed maneuver and gust conditions for critical flight mission points. Since the joined-wing concept has non-linear deformation characteristics, the structural optimization used both strain and buckling limits. The collection of the optimized data points was combined to create a response surface to predict the best joined-wing geometric configuration. Each configuration varied one of six key geometric variables. The geometric configuration variables included front wing sweep, aft wing sweep, outboard wing sweep, joint location, vertical offset, and thickness to chord ratio.

Table of Contents

List of Figures

List of Tables

List of Symbols

Symbol	Definition
α	Angle of Attack, Resizing Exponent
β	Response Surface Coefficient
δ	Aft-Wing Twist Angle
ρ	Air Density
ε	Strain
σ	Stress
Λ	Wing Sweep Angle
μ_g	Wing Mass Ratio
μ	Micro
a	Slope of $C_L - \alpha$
c	Wing Chord Length
f	Aerodynamic Pressure
ft	Feet
g	Acceleration Due to Gravity, Inequality Constraint
h	Equality Constraint
k	Structural/AVTIE Fuel Ratio
ksi	Thousand Pounds per Square Inch
m	Meters
q	Dynamic Pressure

Symbol	Definition
r	Resultant Forces
s	Seconds
t	Element Thickness
x	Cartesian Coordinate, Thickness Design Variables
y	Cartesian Coordinate, Response
z	Cartesian Coordinate
u	Displacement in Cartesian Coordinates
u_g	Gust Velocity
v	Displacement in Cartesian Coordinates
w	Displacement in Cartesian Coordinates, Downwash
A	Aerodynamic Influence Coefficient Matrix
B	Shape Function Derivative, Breguet Scalar
C	Specific Fuel Consumption
D	Drag
E	Modulus of Elasticity
F	Forces
K	Stiffness Matrix, Gust Alleviation Factor
L	Lift
M	Mass Matrix
N	Shape Function
P	Aerodynamic Forces

Symbol	Definition
Pa	Pascals
Q	Net Aerodynamic Influence Coefficient Matrix
R	Range, Regression
S	Span, Wing Surface Area, Integration Matrix
V	Velocity, Volume
W	Weight
X	Sample Value

Acknowledgements

I would first like to thank my thesis advisor, LtCol Robert Canfield, for his extensive help, support, and wisdom throughout this challenging process. I would also like to thank Dr. Max Blair, from the Air Force Research Laboratory, and Jeremiah Allen, from Wright State University, for their efforts in developing a brilliant software tool. Additionally, I want to thank Jack Castro, Cassandra Raddigan, and Erwin Johnson, from the MSC.Software Corporation, for their solutions to unsolvable problems. Finally I would like to thank my wife for all of her emotional support.

Cody C Rasmussen

OPTIMIZATION PROCESS FOR CONFIGURATION OF FLEXIBLE JOINED-WING

I. Introduction

1.1 Overview

Sensor-craft is a conceptual aircraft based on an Air Force need for advanced, long-endurance tactical surveillance using current and future sensor packages. A potential vehicle design is a joined-wing configuration that could lead to improved radar capabilities, increased aerodynamic performance, and structural weight savings. The Air Force Research Laboratory, Air Vehicles Directorate, leads the sensor-craft conceptual design study.

A joined-wing aircraft is a vehicle with an aft-wing smoothly joined with the front wing. The front wing is rooted with the fuselage while the aft wing is rooted at the top of the vehicle's tail. Typically, the front wing is swept back and the aft wing is swept forward. The front and aft wings are not typically joined at their tips and thus an outboard wing extends past the joined section. Figure 1.1 displays an illustrative joined-wing concept and Figure 1.2 shows the half wing analytical model at various angles.

Since the aft and front wings are connected, each wing can behave as a support strut for the other depending on load conditions, wing sizing, and geometry. Typically, the aft wing resists the lifting bending moment by undergoing a majority of axial compression. Relieving of the bending moment may decrease the amount of material needed in certain areas of the wing, but the axial compression may involve premature wing buckling. Axial loads may require more wing structural material overall to resist buckling and may negate weight reduction benefits [24].

Figure 1.1 Sample Total Joined-Wing Configuration Concept

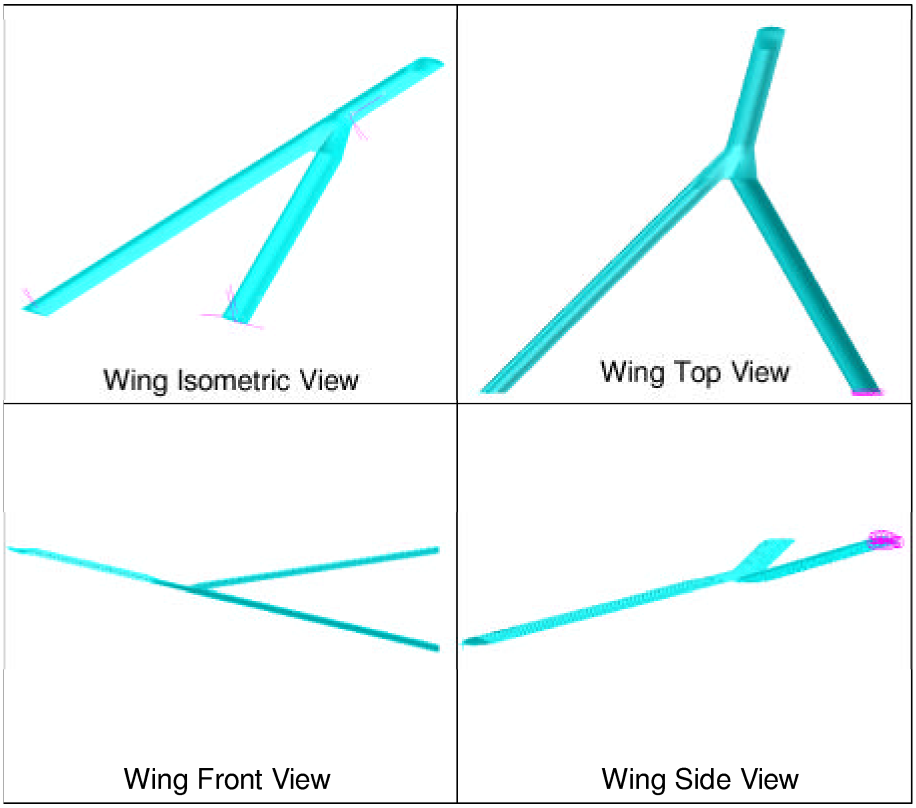

Figure 1.2 Various Joined Wing Viewing Angles

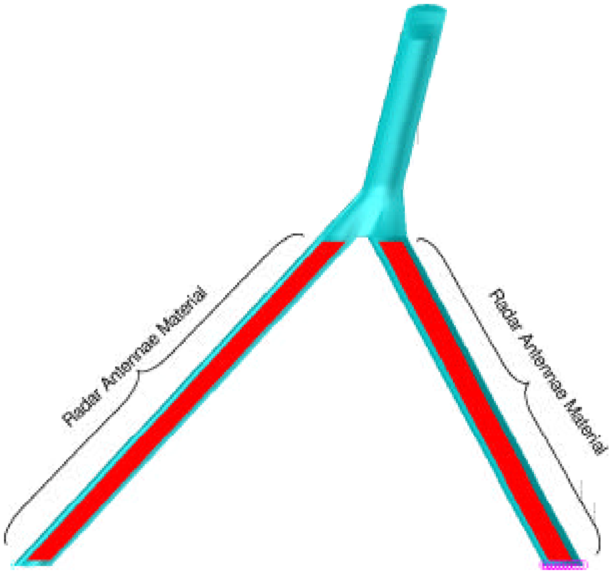

Figure 1.3 Radar Antennae Location

The present joined-wing sensor-craft concept includes a wing span of 68 m. The front, aft, and outboard wings have a chord of 2.5 m. The joint section of the wing has a variable chord ranging from 5.625 m to 2.5 m. This allows a smooth joining of the front and aft wing to the transition to the single outboard wing. The airfoil shape is an LRN-1015. This airfoil shape is similar to airfoils used on Unmanned Air Vehicles such as the Global Hawk [1].

The sensor-craft concept includes radar antennae in both the forward and aft wings (shown in Figure 1.3). This produces an extremely large radar aperture which can provide surveillance using Ultra High Frequencies. This level of radar capability can even provide foliage penetration to create an image for the warfighter below a canopy of vegetation [15].

A suggested mission profile for a sensor-craft includes a gradual ingress to 55,000 feet, a 24 hour loiter from 55,000 feet to 65,000 feet over a critical surveillance location, and finally a gradual egress to ground level [1, 15]. Figure 1.4 shows an assumed mission history profile.

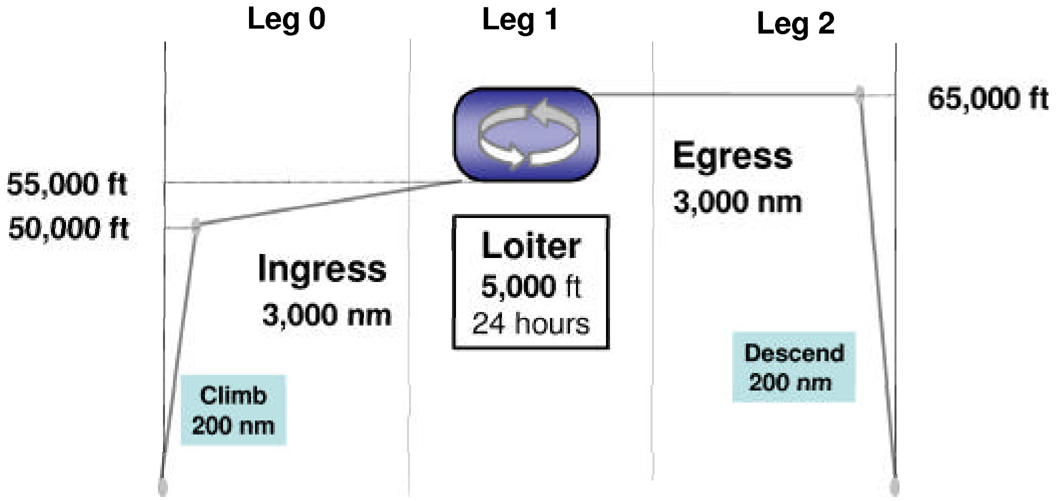

Figure 1.4 Notional Mission History Profile

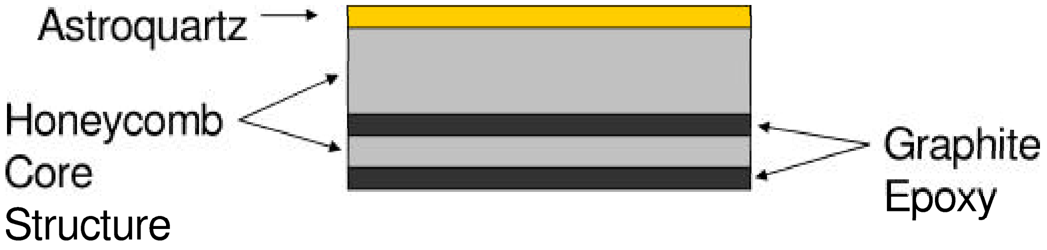

Figure 1.5 Conformal Load-Bearing Antennae Structure (CLAS)

Conveniently, a portion of the radar antennae can be used as load bearing material and provides significant weight savings over classic aircraft material. The composite includes a sandwich of Graphite/Epoxy, Carbon foam core, and Astroquartz [19] as shown in Figure 1.5. The Graphite/Epoxy layers bear the majority of the loads. The Astroquartz provides protection against external environmental effects and is an electromagnetically clear material for the radar antennae to transmit and receive through.

The coupling of aerodynamics and structural analysis is a complex problem. Since the flow of air changes with the deflection of a wing and the loads on a structure change with the flow of air, an aeroelastic optimization proves to be inaccurate if only one type of analysis is completed at a time. To combine the two types of analyses, FlightLoads [16] was used in conjunction with the NASTRAN structural optimization [10] mode.

Creating a number of joined-wing configurations and the respective grids for aeroelastic optimization can be a tedious task. However, by using an Adaptive Modeling Language (AML) [21], the user can create multiple grid configurations easily by providing general geometric information. Dr. Max Blair developed the Air Vehicles Technology Environment (AVTIE) to specifically utilize AML for the joined-wing aircraft concept [1].

1.2 Research Objective

This research focused on an overall understanding of the behavior of various geometric configurations of the joined-wing vehicle concept. Six key geometry defining variables were varied to develop multiple joined-wing configurations. These included front wing sweep, aft wing sweep, outboard wing sweep, joint location, vertical offset of the aft-wing root, and airfoil thickness to chord ratio. Structural optimization, aerodynamic analysis, and response surface methodology were combined to determine what the weight optimum joined-wing configuration is and how each key geometry configuration variable defined that optimal configuration.

1.3 Recent Collaboration

The Air Force is currently conducting studies to explore the design of an unmanned joined-wing sensor-craft. The Air Force Research Laboratory (AFRL/VA) is working with Lockheed, Boeing, and Northrop-Grumman to complete these studies. Such levels of initial design studies include sensor integration, subsystem configuration, concept refinements and description, and modeling and simulation.

This study included collaboration with Boeing on the feasibility of the structural model and FlightLoads aerodynamic model. As a part of this collaboration, structural effects such as buckling and non-linear deformations have been confirmed to be critical for the design of the Boeing joined-wing concept, as well as the current version examined here.

1.4 Methodology Overview

The optimization is two-tiered. The first tier included finding an optimal weight for each configuration through gradient-based structural optimization methods. For each geometric aircraft configuration, a structural and aerodynamic analysis was completed and combined to provide a total mission load history. A weight optimized solution was found by varying spar, rib, and skin thicknesses of the wing structure to determine the optimal material distribution to sustain gust, maneuver, and impact loads. The next tier of optimization utilized an approximation method covering the entire design space. This was done by creating a response surface based on weight-optimized configurations. The overall process is shown in Figure 3.14.

An automated process was devised to complete a series of structural and aerodynamic simulations to optimize a single-point joined-wing design (tier one). Utilizing this process, simulations were conducted on a range of configurations beyond the single-point baseline configuration (tier two). This provided a greater understanding of aeroelastic response to joined-wing configuration changes [15].

Recent analyses have shown that a typical joined-wing configuration exhibits large geometric non-linearity below the critical buckling eigenvalue. Non-linear analysis is critical to correctly modeling some, if not all, joined-wing sensor-craft configurations. In addition, it has been shown that buckling is a critical constraint factor. This study sought a weight optimized design that is safe from buckling and does not exceed yield strain limits. Four different critical mission points were analyzed for each particular configuration. Each mission load set was combined to form a complete structural analysis in which wing weight was minimized for the total mission range.

The analysis for a flexible wing was conducted within NASTRAN, since it is fully integrated between its aerodynamic package (FlightLoads) and its structural and optimization package (NASTRAN). More than one run was conducted to account for fuel weight changes and for instantaneous gust analyses.

1.5 Assumptions/Limitations

In past joined-wing studies, the finite element model of the vehicle included an unrealistically large number of spars and ribs inside the wing or it was assumed to be a simple plate model [14, 15]. Roberts' model had a large number of ribs and spars in order to determine where the material should be placed in a joined-wing configuration. His results led to the conclusion that a two spar wing is the proper configuration to use in joined-wing construction [15]. This study built on Roberts' model, but reduced the number of spars and ribs. The front, aft, and outboard wings contain an industrial standard two-spar configuration at 10% chord and at 80% chord. The previous spar/rib configuration is shown in Figure 1.6. The new spar/rib configuration is shown in Figure 1.7. The joint section of the wing contained a total of six spars where two spars from each wing continue through the joint. The joint section spars were located at 5%, 10%, 40%, 55%, 80%, and 90%. The spar/rib configuration of the joint section is displayed in Figure 1.8.

The number of ribs were reduced so that the skin panels surrounded by spars and ribs had more of a square shape rather than an elongated rectangular shape. Even though the number of spars and ribs were reduced, the number of finite elements were increased to preserve element aspect ratios. In the rear of the wing, the aft spar included elements that were narrow and long. To improve the aspect ratio of these skewed elements, the total number of elements across the entire model was increased so that each element was nearly square.

The wing box was the primary load bearer and was the only designable part of the wing. Material outside the wing was not designed. Large transverse shear may

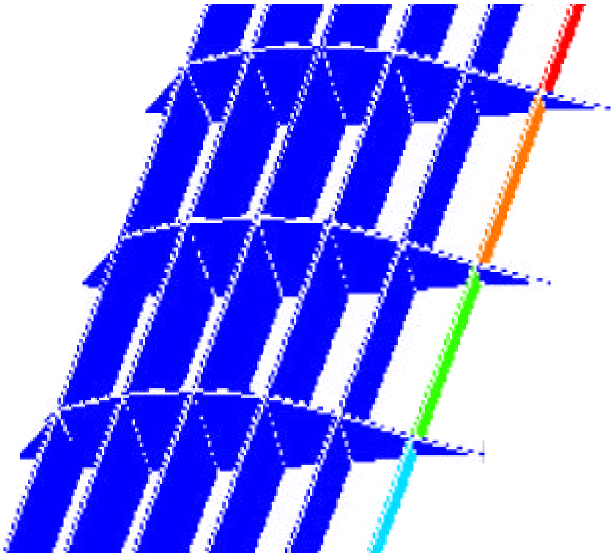

Figure 1.6 Previous Spar/Rib Configuration in the Front, Aft, and Outboard Wing Sections

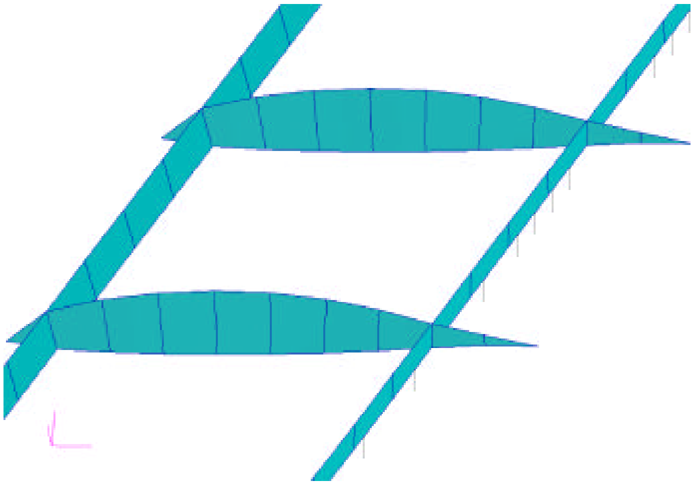

Figure 1.7 Updated Spar/Rib Configuration in the Front, Aft, and Outboard Wing Sections

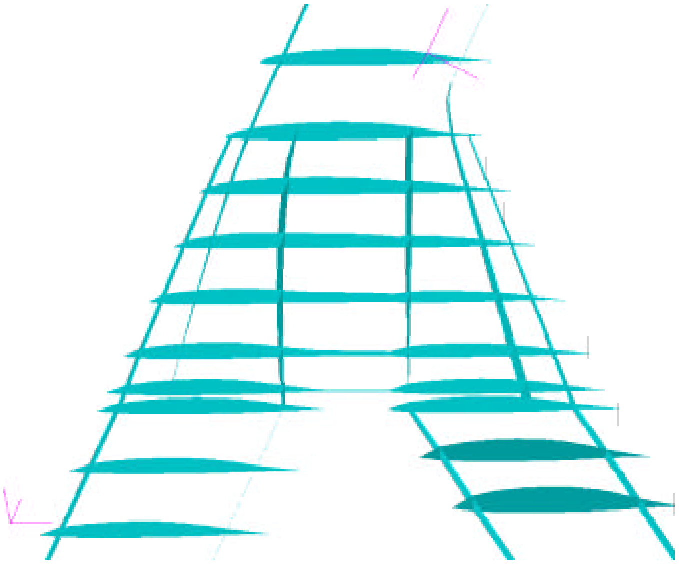

Figure 1.8 Updated Spar/Rib Configuration Joint Wing Section

occur in the non-stiff finite elements that are behind the furthest aft spar in a wing section. To prevent significant airfoil shape changes in the aft of the wing, rigid body elements were used to maintain airfoil camber and shape forward of the front spar and behind the aft spar on every wing section (Figure 1.9). The skin elements that were surrounded by rigid body elements were not designed, but instead were given a very low modulus of elasticity to avoid their bearing load and having high strain. Even though non-stiff material was used in these skin elements, the airfoil could not lose its shape due to the rigid body elements maintaining the airfoil shape and the spars and skins maintaining the wing box shape. This may add some directional stiffness to the wing.

The FlightLoads aeroelastic analysis involves a finite element model where a series of rigid body elements represent the fuselage of the structure. Near the center of gravity of the vehicle, the entire aircraft is allowed to pitch and vertically accelerate. This allows a pivot point for the FlightLoads routine to balance forces. FlightLoads uses the doublet-lattice method to calculate aerodynamic forces on the structure [16]. The doublet-lattice method can only estimate linear aerodynamic

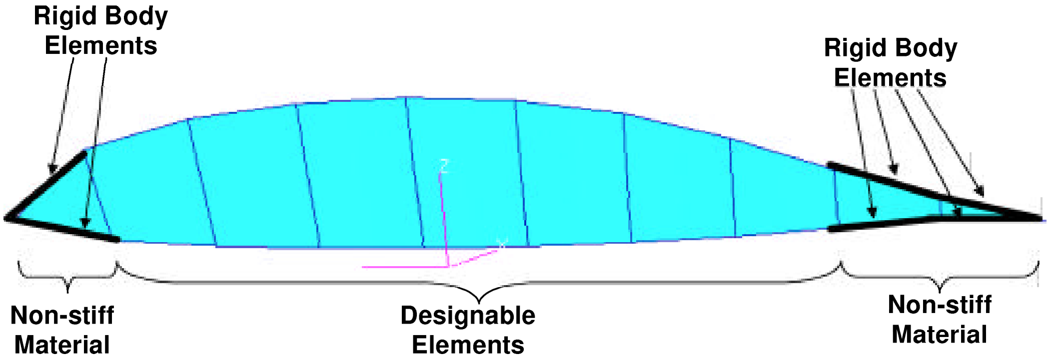

Figure 1.9 Placement of Rigid Body Elements and Material in Rib

loads. Due to linear aerodynamics limitations, FlightLoads neglects follower force effects of air loads being adjusted for large displacements and rotations.

Drag was not modeled in FlightLoads. For a high aspect ratio vehicle, such as the joined-wing concept, the lift over drag ratio is on the order of 20 or greater [13,15]. A fixed lift over drag ratio was assumed. In addition, the climb and descent of the vehicle were not modeled in the FlightLoads environment. It was assumed that at the beginning of ingress, the vehicle was at 50,000 ft. Similarly, at the end of egress, the altitude of the vehicle was at 50,000 ft immediately before landing.

CLAS was not used throughout the entire wing. It was only used in the skins of the front and aft wing (Figure 1.3). The joint and outboard sections of the wing use only the Graphite/Epoxy material. The Graphite/Epoxy plies are defined by design variables in the NASTRAN optimization routine. The Graphite/Epoxy plies were simplified in the model to be represented as four designable plies orientated at 0°, 45°, -45°, and 90° from each wing's longitudinal axis. The material was assumed to have linear properties under all strain and buckling limits. Under these conditions, any level of large deflections and large strains were allowed within the structural analysis.

The fuel mass distribution was taken from a baseline case from the AVTIE work environment. The inertia relief effect of the distributed fuel mass was modeled as a static load in the negative vertical direction. From these static loads sets, the fuel weight was modified and scaled to different magnitudes, given any particular joined-wing weight configuration in any stage of its flight. In addition, the fuel weight was scaled for any point in the mission profile using the Breguet range equation

$$R = \left(\frac{V}{C}\right)\left(\frac{L}{D}\right)\ln\left(\frac{W_a}{W_b}\right) \tag{1.1}$$

where R is the mission leg range, V is velocity, L/D is the lift over drag ratio, and Wa/Wb is the total change in weight ratio over the mission range. An extensive description of the fuel weight scaling is described in Appendix A. For the impact case, the only loads applied were the static fuel and structure weight. The landing gear, fuselage, and tail were not modeled in the impact load case.

A factor of safety of 1.5 was applied to all design constraints. For the Graphite/Epoxy, the ply strain limit was 0.0050 $\mu\varepsilon$. With a factor of safety of 1.5, the maximum strain for any ply in any subcase was 0.00333 $\mu\varepsilon$. The buckling eigenvalue is defined as the fraction of applied load required to make the structure buckle. A limit that the calculated buckling eigenvalue must be greater than 1.5 was applied. This means that the structure could not buckle until the load was 1.5 times greater than the applied load case. Roberts determined that a design or analysis of a joined-wing model must include non-linear deformation structural effects [15]. By using buckling eigenvalue limits, the majority of non-linear deformations can be avoided.

1.6 Furthering Joined-Wing Work

The most relevant recent work to this study includes Roberts' masters thesis. Roberts analyzed and verified the unique structural qualities of the joined-wing sensor-craft [15]. His analysis of the joined-wing included a highly manual and labor-intensive optimization of a single point baseline configuration. This study incorporated lessons learned from Roberts and completed 74 optimized configurations.

As part of lessons learned, this study utilized a two-spar configuration in the main wing sections to make a more realistic wing substructure. In addition, this study utilized FlightLoads to model the aerodynamic loads instead of PANAIR. By using FlightLoads, the NASTRAN optimization analysis and aerodynamic analysis was fully integrated and automated.

Automating the integration between aerodynamics and structural optimization was necessary to facilitate the overall optimization of multiple configurations. A significant portion of this study was devoted to developing an integrated process for generating different grid points for different configurations, running three separate optimization phases, and recalculating aerodynamic loads between optimizations. Finally, since Roberts determined that non-linear deflections are key, buckling was added as a constraint in the optimization.

1.7 Implications and Overview

The generation of a response surface that defines the weight behavior across a variety of joined-wing configurations can provide future designers a general basis for which to fabricate a joined-wing sensor-craft. A proper understanding of joint location, wing sweep angles, wing offsets, and airfoil characteristics are essential for basic conceptual airframe design.

Chapter 2 reviews past research completed on the joined-wing aircraft and discusses key effects that are included in this study. Key effects such as unique structural design, structural non-linearity, aeroelastic coupling, and configuration design are covered.

Chapter 3 discusses the methodology and theory involved to generate each optimized configuration and the response surface. The chapter reviews the theory behind finite elements, buckling using finite elements, non-linear deflections using finite elements, and finding aerodynamic loads using aerodynamic panel elements. The chapter shows what configuration variables were used, how to generate gust and impact loads, what materials were used, and what software environments were used. In addition, chapter 3 explains the process for generating gust and impact loads, the process for generating a single optimized configuration, and the process for generating a response surface to find the overall optimal configuration.

Chapter 4 shows the results from generating the response surface and discusses the discovered iterations and trends. Chapter 5 discusses the conclusions drawn from the results.

II. Literature Review

2.1 Introduction

This chapter reviews past research conducted on the unique effects of the joined-wing aircraft. This research built the basis for the current configuration design study.

The next section of this chapter discusses the distinct structural design aspects of the aircraft to include unique placement of material for different stiffening effects and buckling sensitivity. The joined-wing coupling section includes a discussion of the coupling of the structural and aerodynamic analyses of the joined-wing aircraft. The non-linearity section discusses the structural non-linearity behavior of a joined-wing aircraft with a large wing span and the optimization of such a joined-wing structure. The final portion of this chapter discusses the vehicle's geometric configuration design where major configuration variables like joint location vary.

2.2 Basic Structural Design Aspects

Wolkovich proposed a joined-wing design with potential weight savings and aerodynamic benefits as early as 1986 [24]. He pointed out that the inclined plane of the joined-wing causes a forward bending moment about the vertical axis. This is shown in Figure 2.1. To counter this bending moment, Wolkovich stated that the structural material distribution should be as far away from the inclined bending plane as possible, which means the upper leading edge and lower trailing edge of a joined-wing must contain the most structural material possible [24]. This is shown in Figure 2.2.

Gallman and Kroo examined a joined-wing configuration to meet the mission requirements of a medium-range transport aircraft [3]. They used a simplified aluminum wing box structure in the finite element model. This simplified model was

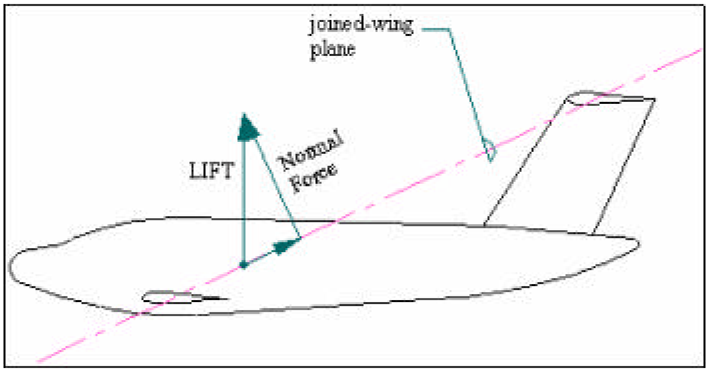

Figure 2.1 Joined-Wing Bending Plane with Vertical Offset

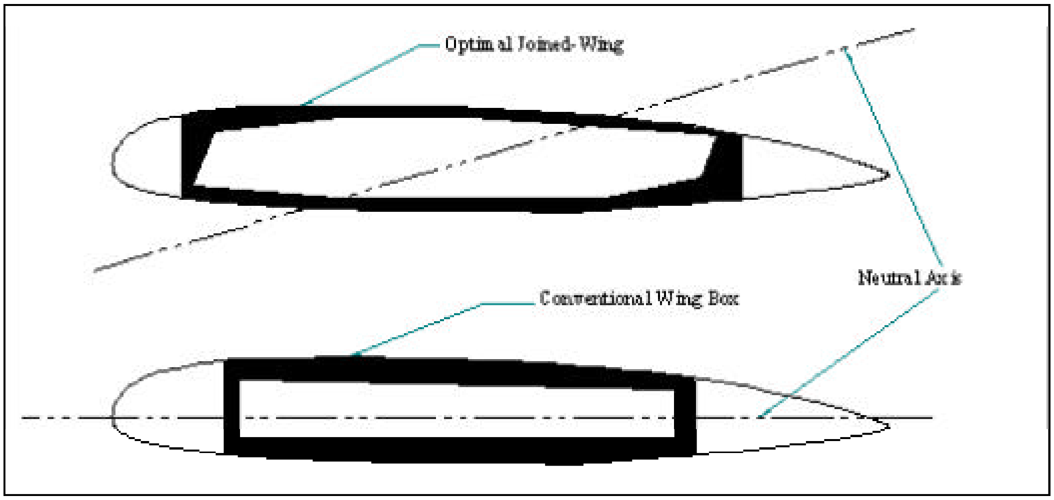

Figure 2.2 Joined-Wing Box Structural Mass Distribution

optimized for a minimum weight under gust load conditions. They used zero fuel weight due to the increased load factor caused by a gust under this flight condition. When Gallman and Kroo included buckling as a design constraint in their analysis, the weight increased by 13%. This led to a higher Direct Operating Cost when compared to a Boeing 727 [3]. However, they conceded, “a different set of mission specifications and design assumptions may produce joined wings that perform significantly better”. This current research includes gust loads as well as taxi-crater impact, landing and steady maneuver load cases.

2.3 Joined-Wing Coupling of Structural and Aerodynamic Effects

In 1984, NASA Ames Research Center began a study to research the possibility of building a joined-wing airplane. NASA intended the aircraft to be a proof-of-concept demonstrator [20]. The researchers discovered that even with extensive aerodynamic design, the wind tunnel model still exhibited an unstable stall characteristic. The stall characteristic was improved with vortilions installed on the wind tunnel model, but a flight test vehicle was never built. It should also be noted that there was no structural optimization design performed. The horizontal tail structure was strengthened with additional material where buckling was predicted.

Extending research on the NASA Ames feasibility study, Lin, Jhou, and Stearman examined the joint configuration with the NASA wind tunnel model [7]. They employed linear finite element analysis and experimental analysis on the wind tunnel model. The NASTRAN analysis indicated a lower root bending moment than the experimental results. The authors attributed this difference to the absence of friction in the finite element model. They concluded that the rigid wing-joint had the best structural characteristics. The sensor-craft concept used in this study assumed the use of a rigid joint configuration. It also included a preliminary concept of the rib and spar configuration at the wing-joint.

Livne surveyed past joined-wing research and attempted to provide a direction for future studies. He concluded that the joined-wing configuration creates complex interactions between aerodynamics and structures [8]. Livne advocated the use of a multi-disciplinary design approach to simultaneously design aerodynamics and structures. This current study integrates structural and aerodynamic design into a single process.

Lee and Chen conducted research on non-linear aeroelasticity. To do this, they divided non-linear systems into sub-linear systems, which can be discretized and handled in a straight-forward manner [6]. They used the joined-wing concept to demonstrate this effect, since the joined-wing concept is a highly non-linear aeroelastic structure. The topic areas covered aeroelastic non-linearity, control system non-linearities, and buckling as a non-linear structural effect. They strongly concluded that buckling is an important effect to account for, when designing a joined-wing aircraft. In this study, buckling will be considered in all optimizations.

Nangia, Palmer, and Tilmann analyzed the effects of forward swept outboard wings on a joined-wing aircraft [12]. They compared lift distribution curves for various outboard wing sweep angles. They found that a forward swept outboard wing moves the vehicle's center of pressure and neutral point more forward and closer to the vehicle's center of gravity. This induced a more even distribution of lift forces on the front and aft wings. In addition, the distribution across the span of the wing was more elliptical than an aft swept outboard wing and produces a more traditional spanwise lift distribution. This proved that a forward swept outboard wing may be more feasible than only an aft swept outboard wing. A full range of outboard wing sweep angles were explored in this study.

2.4 Joined-Wing Structural Non-Linearity

Blair and Canfield proposed an integrated design method for joined-wing configurations [1]. Blair developed a geometric model and user interface using the Adaptive Modeling Language. The model can be analyzed for structural or aerodynamic characteristics through external software. They concluded that non-linear structural analysis is important to accurately capture the large deformations that occur in this joined-wing configuration.

Recent work conducted by Roberts, Canfield, and Blair included a single-point configuration design of an aluminum joined-wing that was made safe from buckling by using non-linear analysis [15]. Deformations were found to be over ten times as great as those found using linear structural analysis for a structurally optimized, aerodynamically stable structure. This current research expanded and automated this analysis and weight optimization process to facilitate the process of conducting multiple analyses on multiple configurations made of composite materials. This provided understanding into aeroelastic effects for various configuration changes.

Patil conducted a single analysis of a similar joined-wing configuration. Major differences were that the joint location was closer to the wing root and the wing was in a horizontal plane (small vertical offset) [14]. Patil showed relatively close linear and non-linear deformations. This could be caused from a closer joint location where the stiffer joined-wing might behave similarly to a non-joined-wing. A non-joined-wing aircraft with a long outboard wing has a deeper wing box with larger thicknesses. Hence, non-linear deformations calculations are closer to linear deformations. This research explored various configurations which might show the transition points between linearity and non-linearity. For example, the aft-wing compression will disappear without a vertical offset and would thus eliminate aft-wing buckling.

2.5 Configuration Design

Weisshaar and Lee explored configuration changes of a joined-wing aircraft with respect to flutter speed using Rayleigh-Ritz and finite element modeling [5,23]. The most noteworthy results are how the joint location and sweep angle affect the joined-wing design. Sweep angles from 30° to 45° were examined using parametric methods. In general, as the sweep angle rose for a fixed span size, the flutter dynamic pressure increased. In addition, as the joint location moved from the middle of the wing to the tip of the wing, the flutter dynamic pressure decreased slightly. A sweep angle of 30° displayed a smaller flutter dynamic pressure than a sweep angle of 45°. This current research explores parametric configuration changes like Weisshaar and Lee, except it is optimized for flexible static air loads throughout the mission profile instead of conducting a flutter analysis for a single point in the flight envelope.

III. Methodology

3.1 Aircraft Geometry Configuration Variables

Each geometric configuration was defined by six key independent design variables. From these variables and from a set of equality constraints, the entire wing configuration was determined. Figure 3.1 depicts a typical joined-wing planform configuration used in this study, and Table 3.1 lists the relevant geometric variables to determine the range of configurations.

All three separate sweep angles were used to define wing geometry. Front wing sweep angle (Λ_{ib}) involved changing the angle the front wing makes with the fuselage. The outboard wing sweep angle (Λ_{ob}) varied the angle of the wing part that extends from the joint to the tip. Aft wing sweep angle (Λ_{ia}) defined the forward swept angle the aft wing creates with the fuselage. The joint location $[S_{ib}/(S_{ib} + S_{ob})]$ involved varying the intersect point where the front wing coincides with the aft wing. For consistency in comparing configurations, the span $S_{tot} = (S_{ib} + S_{ob})$ was set to be constant at 32.25 m. The vertical offset of the aft wing intersection to fuselage (z_{fa}) was the vertical distance between where the aft wing root is connected to the vertical tail and where the front wing connects to the fuselage. Finally, the thickness to chord ratio (t/c) of a standard airfoil varied to represent actual geometric changes in wing box size (vertical stretch of airfoil). All chord lengths were set constant to meet requirements that a radar array is to be imbedded in the wing.

The equality constraints included configuration parameters that are dependent on the six key design variables discussed above and shown in Table 3.2. Since the span is constant, the outboard span was expressed in terms of the joined location design variable.

$$S_{ob} = S_{tot}\left(1 - \frac{S_{ib}}{S_{ib} + S_{ob}}\right) \tag{3.1}$$

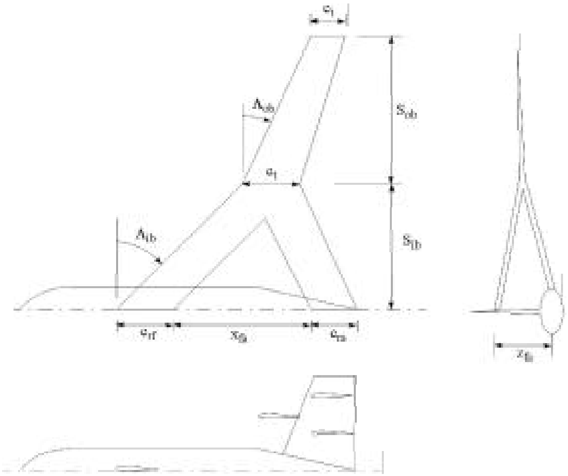

Figure 3.1 Planform Configuration Variables

Variable	Name	Size
$S_{ib}/(S_{ib}+S_{ob})$	Joint Location	Varies
$S_{ib}+S_{ob}$	Total Span Length	32.25 m
c_{rf}	Chord at Front Root	2.50 m
c_{ra}	Chord at Aft Root	2.50 m
c_m	Chord at Intersection	2.50 m
c_t	Chord at Tip	2.50 m
t	Airfoil Thickness	Varies
x_{fa}	Horizontal Offset	Varies
z_{fa}	Vertical Offset	Varies
Λ_{ib}	Front Wing Sweep	Varies
Λ_{ia}	Aft Wing Sweep	Varies
Λ_{ob}	Outboard Wing Sweep	Varies

Table 3.1 Baseline Configuration Parameters

The inboard span was then specified in terms of the outboard span.

$$S_{ib} = S_{tot} - S_{ob} \tag{3.2}$$

The horizontal offset was placed in terms of the front and aft sweep angles and the inner offset

$$x_{fa} = x_{fa-inner} + S_{ib} \left(\tan\left(\Lambda_{ib}\right) + \tan\left(\Lambda_{ia}\right)\right) \tag{3.3}$$

where the inner offset ($x_{fa-inner}$) was defined as the distance between the front and aft wing at the joint root. The inner offset was set as a constant (0.625 m).

3.2 Upper bound and Lower Bound Constraints

Each of the six key design variables has a defined range where it is feasible. This limits the analysis to reside within a reasonable scope.

The front and aft wing sweep angles are constrained by the system's radar coverage requirements. The radar contained within the wings must provide 360 ° of coverage around the vehicle. The maximum change in electromagnetic beam steering angle from the normal direction of the wing at which the end-fire radar can properly receive/transmit is approximately 60 °, also knows as the grazing angle [19]. This implies that the front and aft wings must have a sweep angle within 30 ° to 60 ° to achieve complete coverage. The aft wing is forward swept, but the sweep notation will be positive instead of negative. As shown in Figures 3.2 and 3.3, there is always 360 ° coverage as long as the front and wing sweep angles are within 30 ° and 60 °. For configuration exploration, the aft wing was allowed to have 0 ° sweep to create a center of pressure that is more forward than aft. The center of pressure must be at the center of gravity for forces to balance and the vehicle to trim. A more forward center of pressure creates a stronger stability moment in the pitching direction.

The horizontal offset was not an independent design variable for this problem, since both the front and aft sweep angles define the horizontal offset distance. In

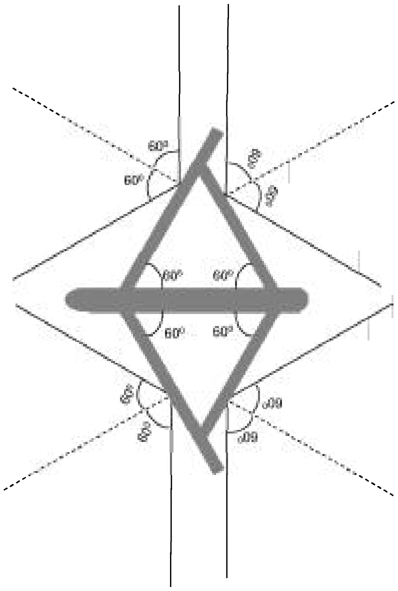

Figure 3.2 Radar Coverage for 30 Degree Sweep Angle

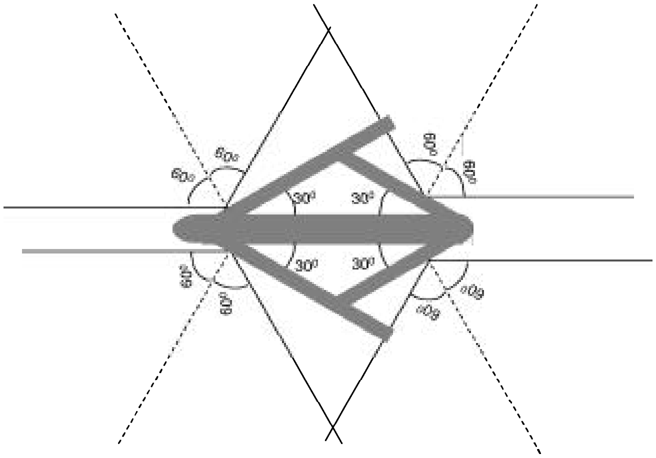

Figure 3.3 Radar Coverage for 60 Degree Sweep Angle

Variable	**Variable Description**	**Lower Bound**	**Upper Bound**
Λ_{ib}	Front Wing Sweep	30°	60°
Λ_{ia}	Aft Wing Sweep	0°	60°
Λ_{ob}	Outboard Wing Sweep	-30°	60°
$S_{ib}/(S_{ib}+S_{ob})$	Joint Location	0.5	0.9
z_{fa}	Vertical Offset	0.0 m	10.0 m
t/c	Thickness over Chord Ratio	10.6%	20%

Table 3.2 Design Variable Bounds

addition, the outboard wing sweep angle ranged from -30° to a maximum of 60°. Again, the forward outboard wing sweep allowed for a more forward center of gravity producing more stability in the pitching direction.

The fractional joint location changed from 0.5 to 0.9. At 1.0, the aft wing and front wing are joined at the tip. A maximum joint location of 0.9 was established so that an outboard wing exists for every configuration. A joint location less than 0.5 was not used. This left enough room for the radar array to reside within the front and aft wings.

The thickness to chord ratio (t/c) ranged from 0.106 to 0.20. The upper and lower bounds are set outside current typical aircraft configurations due to unique qualities of the joined-wing aircraft. Since the wings are offset, the twisting and bending inertias are not typical. Unique t/c ratios can prove to be more lightweight, since the bending axis is tilted, not horizontal. A thicker wing produces more drag, but drag analysis was neglected in this study due to assuming a fixed lift over drag ratio.

The vertical offset of the root location of the front and aft wings ranged from 0.0m to 10m. A vertical offset of 0.0m defines a front and aft wing within the same horizontal plane. This prevents the aft wing from residing lower than the front wing. An offset of 10m keeps the vertical offset from growing to the extent where the tail wing becomes so large that the fuselage and tail weight assumption should be considered false. Table 3.2 lists all upper and lower bounds for each design variable.

	Ingress	**Loiter**	**Egress**
Range	5550 km	N/A	5550 km
Duration	N/A	24 h	N/A
Velocity	177 m/s	177 m/s	177 m/s
Mach #	0.6	0.6	0.6
Altitude	50,000 ft	65,000 ft	50,000 ft
C (SFC)	2.02E-4 s^{-1}	1.79E-04 s^{-1}	2.02E-4 s^{-1}
Dynamic Pressure	2599 Pa	1269 Pa	2599 Pa
Wa/Wb	1.233	1.907	1.233

Table 3.3 Baseline Aerodynamic Parameters

3.3 Mission Profiles

The Air Vehicles Technology Integration Environment (AVTIE) uses AML coding to provide an interface for PANAIR and NASTRAN and ability to generate a variety of geometric configurations. The AVTIE master interface contains information about the mission profile (altitude, airspeed, fuel consumption rate, etc.). The mission profile reflects the current Global Hawk surveillance mission requirements. AVTIE separates the mission into three categories: ingress, loiter, and egress. Table 3.3 displays the aerodynamic properties used [15]. AVTIE used this information to provide the weight of the remaining fuel at any point in the mission. The sensor package (payload) had an estimated mass of 2200 kg.

Each mission category (ingress, loiter, and egress) has a respective total change in weight fraction (W_a/W_b), which is determined through the Breguet range equation (Equation 1.1). Using the information from Table 3.3, and by assuming a constant lift over drag ratio, the total fuel weight can be determined for a determined structural weight. Reference Appendix A for more information on calculation and scaling of fuel weight.

Roberts utilized eleven mission load sets in his analysis which covered virtually every part of the mission profile. He showed that four critical mission points drove over 95% the design space [15]. The four critical cases included two maneuver cases

Mission Load #	Load Type	Mission Category	Cat. Complete
1	**Maneuver**	**Ingress (0)**	**0%**
2	Maneuver	Ingress (0)	50%
3	Maneuver	Loiter (1)	0%
4	Maneuver	Loiter (1)	50%
5	Maneuver	Egress (2)	0%
6	Maneuver	Egress (2)	50%
7	**Maneuver**	**Egress (2)**	**98%**
8	Level-Gust	Egress (2)	98%
9	**Turbulent-Gust**	**Egress (2)**	**98%**
10	**Taxi Impact**	**Pre-Ingress**	**0%**
11	Landing Impact	Egress (2)	100%

Table 3.4 Mission Load Sets

(beginning and end of mission), one gust case (turbulent gust), and one impact case (before take-off taxi).

The four critical load sets identified by Roberts were used for a gradient based design method using NASTRAN. Proper aerodynamic load sets were obtained from FlightLoads for each respective mission category. Appropriate fuel weight forces were applied for percent mission complete. Gust loads were created using a calculated change in angle of attack induced by the gusts. The taxi impact load case is a non-aerodynamic load set which only factors fuel weight. The highlighted mission loads in Table 3.4 are the applied critical mission sets that were used in the configuration analysis.

3.4 AVTIE Model and Environment

The Adaptive Modeling Language, developed by TechnoSoft Inc., allows the researcher to develop a model with defined geometric relationships [21]. Blair and Canfield have developed the Air Vehicles Technology Integration Environment (AVTIE) [1], which provides a user interface to the AML software capabilities. AVTIE converts the geometric model into data files which can be manipulated into a complete NASTRAN optimization run.

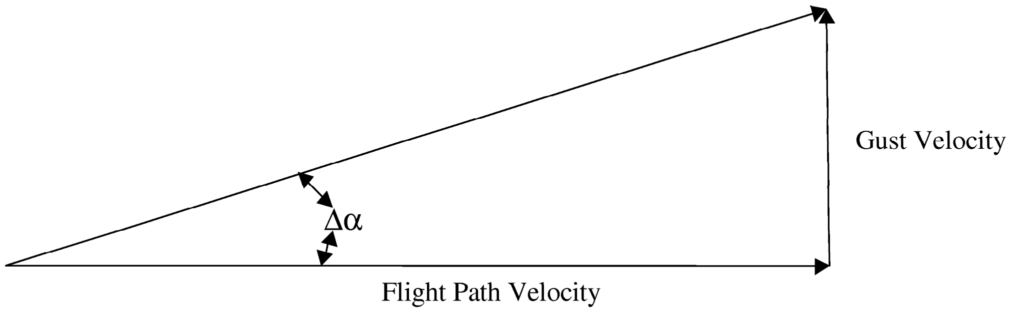

Figure 3.4 Gust Velocity Component

3.5 Gust Loading

The gust loading analysis used in this study was assumed to be an instantaneous effect. In order to create static loading information for the structural optimization, an instantaneous effect was appropriate.

The vehicle was considered to be flying at straight and level flight where no current vertical acceleration exists. In a worst case scenario, the aircraft would instantaneously hit a vertical gust wind component resulting in a net change in angle of attack of the aircraft (Figure 3.4). The change in angle of attack of the vehicle would result in a change in lift. This usually would result in a higher load factor than the most serious maneuver load cases. As shown in Equation 3.4, as the gust velocity (U_g) increases, $\Delta\alpha$ increases. Through Equation 3.5, the lift linearly increases with the change in angle of attack.

$$\Delta\alpha = \frac{U_g}{V} \tag{3.4}$$

$$\Delta L = \frac{1}{2} C_{l_\alpha} \Delta\alpha \rho V^2 S \tag{3.5}$$

The effective change in angle of attack does not always reflect what is shown in Equation 3.4. An alleviation factor represents gust loading more accurately. This occurs because an airplane in flight will gradually approach a gust condition [4].

The change in angle of attack with alleviation is defined as

$$\Delta\alpha = \frac{KU_g}{V} \tag{3.6}$$

Where the alleviation factor [4] is defined as

$$K = \frac{0.88 \cdot \mu_g}{5.3 + \mu_g} \tag{3.7}$$

The alleviation factor depends on the mass ratio, μ_g, which is defined by the airplane mass properties and wing loading factors.

$$\mu_g = \frac{2W}{S\rho C_{l_\alpha} cg} \tag{3.8}$$

The critical load case was at the end-of-mission situation where the fuel is almost completely consumed and the fuel weight is minimal. If the fuel weight is minimal, the fuel will not alleviate the lift forces on the aircraft.

There are three key gust situations which need to be analyzed when determining sufficient wing structures [4]. The first is a cruise gust situation where the vehicle is flying at a pre-determined cruise speed. The second is a turbulent gust case where the vehicle is flying at a speed lower than the cruise speed (43 knots less) [4]. The third is a dive gust case where the vehicle is pitching downward. The significant differences between these gust situations are the assumed gust velocities (U_g) and vehicle velocities (V). For cruise gust, U_g is 50 ft/s, for turbulent gust, U_g is 66 ft/s, and finally for dive gust, U_g is 30 ft/s [4]. Roberts determined that the critical gust case is the turbulent gust situation where the vertical gust velocity component is the largest [15].

As the vehicle's altitude decreases, the density increases and the dynamic pressure increases. This results in a dramatically increasing change in lift, determined from Equation 3.5. The gust velocities decrease above 20,000 ft and do not change from 20,000 ft down to ground level [4]. From the above information, the worst gust case can occur when an aircraft is flying at 20,000 ft, in a turbulent situation, at the end of its mission with almost empty fuel bays.

The instantaneous gust loading is completed in FlightLoads by constraining current trim variables. This will induce a situation on the vehicle that would represent proper gust loading. Since two variables must always be free in a FlightLoads analysis, load factor and pitch rate are allowed to change where angle of attack and the aft twist angle is fixed from the 1.0G load case. Load factor and pitch rate are two variables that change under gust conditions.

3.6 Maneuver and Impact Loading

The maneuver loading cases involve assuming an aerodynamic lift distribution where the net magnitude is 2.5 times the total weight of the aircraft (including fuel). This results in a 2.5G pull-up maneuver. In the structural optimization, the included maneuver load sets were at the beginning-of-mission and at the end-of-mission. The maneuver load at the beginning-of-mission did not have the same fuel weight alleviation as the end-of-mission case. The alleviation of the fuel/structure weight is depicted notionally in Figure 3.5. The fuel alleviation at the end-of-mission is almost non-existent since almost all the fuel is expended. Figure 3.6 shows how the fuel alleviation is much less at the end-of-mission. However, the total lift load at the end-of-mission is smaller than at the beginning since the total weight of the aircraft is less. Different load profiles will exist at both mission cases and should be included in the structural optimization.

The impact loading while taxiing on the ground and landing are significant to include in the analysis since they are negative loads which pull down on the wing instead of pulling up during flight. It was assumed that a taxiing impact of 1.75 times the weight and a landing impact of 3.0 times the weight is appropriate [15]. Since both cases are similar, only the critical case is necessary to include in the

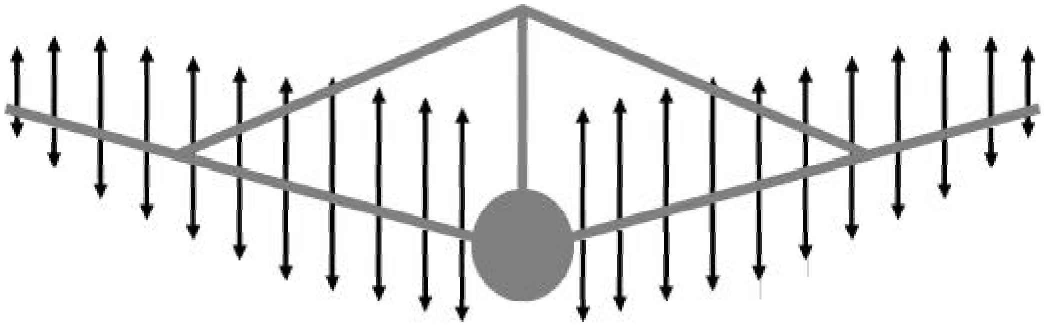

Figure 3.5 Beginning-of-Mission Maneuver Loading

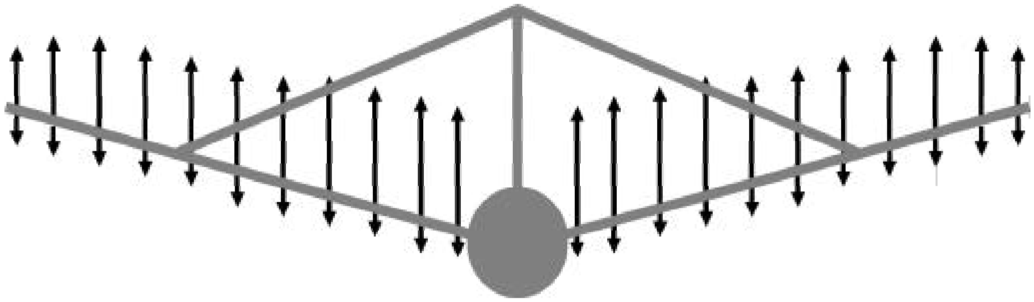

Figure 3.6 End-of-Mission Maneuver Loading

optimization. The taxiing situation is the critical case because the vehicle is full of fuel which will result in a much higher downward force occurring at take off than during landing. This loading distribution is shown in Figure 3.7. Since there is no alleviation in any direction for impact loading, the taxiing impact is the most critical case for strain relationships.

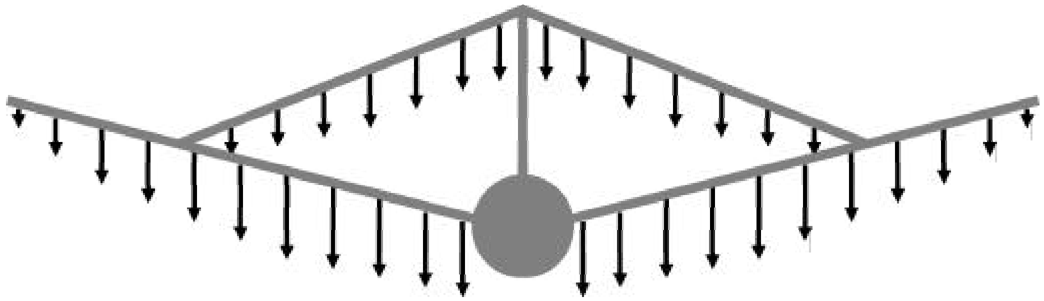

Figure 3.7 Joined-Wing Only Under Fuel/Structure Weight Loads

Property	English Units	SI Units
E_x	22130 ksi	1.53E+11 Pa
E_y	2150 ksi	1.48E+11 Pa
ν_{xy}	0.3	0.3
G_{xy}	600 ksi	4.14E+9 Pa
t_{ply}	0.0056 in	0.142 mm

Table 3.5 Graphite Epoxy: IM7/977-3 Material Properties

3.7 Materials

Composite material was used throughout the joined-wing structure. In the front and aft wing skins, CLAS materials were used to represent radar placement. The CLAS contained Astroquartz, graphite/epoxy, and carbon foam. The Astroquartz allows for clear radar transmission through the wings and was placed at the top of surface of the CLAS. The Astroquartz was offset by using carbon foam (Figure 1.5). The IM7/977-3 graphite/epoxy material supported most of the load due to its high stiffness and strength. Properties of the graphite/epoxy material are shown in Table 3.5 [19].

Since the graphite/epoxy material supported almost 100% of the load, the graphite/epoxy material was the only designable material in the joined-wing structure. The strain limit for a graphite/epoxy ply is 0.005 $\mu\varepsilon$. Applying a factor of safety of 1.5, the strain limit in the optimization model was 0.00333 $\mu\varepsilon$. The plies were oriented at 0 °, 45 °, -45 °, and 90 °. The number of graphite/epoxy plies was determined by the design variables discussed in Section 3.13. As shown in Table 3.6, graphite/epoxy is more than three times as stiff as Astroquartz. Eighteen plies of Astroquartz were used in the CLAS material [15].

The face sheets around the core were not modeled ply by ply in the NASTRAN optimization model. As mentioned in the Assumptions/Limitations section, the Graphite/Epoxy plies were modeled as only four large grouped plies to reduce the

Property	English Units	SI Units
E_x	6800 ksi	4.68E+10 Pa
E_y	1340 ksi	9.23E+9 Pa
ν_{xy}	0.36	0.36
G_{xy}	720 ksi	4.96E+9 Pa
t_{ply}	0.0055 in	0.140 mm

Table 3.6 Astroquartz II/RS12-B Material Properties

number of design variables. In addition, the ply offset that was produced by having Carbon Foam between a set of Graphite/Epoxy plies, was not provided in the model. This is a justified assumption since the sandwich construction design is a local detail governed by panel buckling. Local buckling was not included as a design constraint in this analysis. Posts that connect the top and bottom skins of the model were included to prevent local buckling from occurring in the optimization model.

3.8 Linear Finite Element Statics

Linear finite element theory states that the global stiffness matrix $[K]$ multiplied with the nodal degrees of freedom $\{d\}$, equals the applied resultant forces $\{r\}$.

$$[K_L]\{d\} = \{r\} \tag{3.9}$$

The displacement field $\{u\}$ is determined by assuming a displacement shape function $[N]$ and multiplying it by the nodal degrees of freedom $\{d\}$.

$$\{u\} = [N]\{d\} \tag{3.10}$$

The derivative of the shape functions $[B]$, as defined in a two-dimensional element, can be shown as

$$[B] = \begin{bmatrix} \frac{d}{dx} & 0 \\ 0 & \frac{d}{dy} \\ \frac{d}{dy} & \frac{d}{dx} \end{bmatrix} [N] \tag{3.11}$$

The relationship between strain and displacement is

$$\{\epsilon\} = [B]\{d\} \tag{3.12}$$

which is a key constraint in the optimization analysis. The relationship between stress and strain is established as

$$\{\sigma\} = [E]\{\epsilon\} \tag{3.13}$$

where $[E]$ is the elastic constant.

Through substitution of Equations 3.10, 3.11, and 3.13, into the expression for strain energy, the linear stiffness matrix can be calculated over a two-dimensional quadrilateral area [2].

$$[K_L] = \int_{-b}^{b} \int_{-a}^{a} [B]^T [E] [B] \, t dx dy \tag{3.14}$$

Likewise, for a volumetric element:

$$[K_L] = \int [B]^T [E] [B] \, dV \tag{3.15}$$

3.9 NASTRAN Buckling Theory and Application

Buckling refers to the loss of stability of an equilibrium configuration without fracture or separation of the material [2]. Buckling is influenced by two key parameters, stiffness of the structure and stress stiffening. Stress stiffening occurs under the influence of membrane forces. As a structure undergoes deformation, the structure can actually stiffen if the forces are in the correct direction. Bending deformation is reduced when membrane forces are compressive rather than tensile. The stress stiffness is defined as

$$[K_\sigma] = \int\int [G]^T \begin{bmatrix} \sigma_x I & \tau_{xy} I & \tau_{xz} I \\ \tau_{xy} I & \sigma_y I & \tau_{yz} I \\ \tau_{xz} I & \tau_{yz} I & \sigma_z I \end{bmatrix} [G]\, dxdy \tag{3.16}$$

where I is an identity matrix and $[G]$ is defined as

$$[G] = [\partial][N] \tag{3.17}$$

where $[\partial]$ is the derivative operator through all shape functions [2, 17].

Through determination of the stress stiffness matrix and the structural stiffness matrix, the buckling eigenvalue problem can be defined as:

$$\{[K] + \lambda[K_\sigma]\}\{D\} = 0 \tag{3.18}$$

where λ is the eigenvalue that defines the load multiplier that will result in the structure buckling and $\{D\}$ is the buckling eigenvector and the nodal degrees of freedom.

The lowest buckling eigenvalue was the constraint of interest in the optimization problem. A load lower than 1.5 times the applied model load results in buckling occurring before the established factor of safety.

3.10 Non-Linear Theory and Application

As established by Roberts, non-linear deflections are crucial when designing a joined-wing aircraft. It was assumed in this study that the stress stiffness involved in buckling accounts for a large portion of the non-linear structural deflections [15]. The optimization model considers buckling as a constraint. Non-linear structural deflections occur when stress stiffening occurs, when forces change with deflections, or when material has strained beyond its yield limit and can no longer be considered linear [2]. For this analysis, the material is not allowed to strain beyond its yield limit; therefore, material non-linearities can be ignored. Aerodynamic forces change with wing deflections, especially when applied to the joined-wing aircraft. Forces that change with deflections must be looked at in this study. Stress stiffening, or rather stiffness matrix updating, is an important facet of the joined-wing aircraft.

From the Linear Finite Elements Statics section, the differential internal forces are defined through the linear stiffness matrix.

$$dF = [K_L]\, du \tag{3.19}$$

The non-linear differential internal force is defined by an additive stiffness matrix which is called the tangent stiffness matrix

$$dF = [[K_L] + [K_R] + [K_\sigma]]\, du \tag{3.20}$$

where $[K_R]$ is the stiffness due to large rotation and $[K_\sigma]$ is the stiffness due to stress stiffening [17].

The shape function derivative, or rather the strain-displacement matrix, also becomes an additive matrix that is split into linear and nonlinear parts

$$\bar{B} = [B_L] + [B_N] \tag{3.21}$$

where $[B_L]$ is the linear portion and $[B_N]$ is the non-linear portion of the element matrix. Using the linear and non-linear strain-displacement matrix terms introduced in Equation 3.21, the non-linear rotation matrix becomes

$$K_R = \int \left[[B_L]^T [N] [B_N] + [B_N]^T [N] [B_N] + [B_N]^T [N] [B_L] \right] dV \tag{3.22}$$

The derived tangent stiffness matrix can then be used to develop non-linear deflections and strains.

3.11 FlightLoads Theory and Application

The integration of structural, optimization, and aerodynamic analysis accounts for the important coupling effects. The use of aerodynamic panel elements integrated with the NASTRAN finite element model was key [16]. As discussed in Section 2.3, the coupling of flexible structures and aerodynamic loading is an essential part of the joined-wing analysis.

The proposed sensor-craft concept is a subsonic aircraft. The Doublet-Lattice method is the proper aerodynamic paneling method for subsonic aircraft [16]. The aerodynamic model defines a set of aerodynamic influence coefficients. The downwash is defined as

$$\{w_j\} = [A_{jj}] \left\{ \frac{f_j}{\bar{q}} \right\} \tag{3.23}$$

where $[A_{jj}]$ is the aerodynamic influence coefficient matrix which is a function of reduced frequency, f_j is the pressure on the j^{th} lifting element, and $\bar{q}$ is the flight dynamic pressure. The substantial differentiation matrix which incorporates deflections is defined as

$$\{w_j\} = \left[D^1_{jk} + ikD^2_{jk}\right] \{u_k\} + \left\{w^g_j\right\} \tag{3.24}$$

where D^1_{jk} is the real part and D^2_{jk} is the imaginary part of the differentiation matrix, $\{u_k\}$ are the displacements at aerodynamic grid points, and $\left\{w^g_j\right\}$ is the static aerodynamic downwash from trim variables. The forces can then be determined from integrating the aerodynamic pressures

$$\{P_k\} = [S_{kj}] \{f_j\} \tag{3.25}$$

where $[S_{kj}]$ is the integration matrix.

Equating Equations 3.23 and 3.24, and then solving and substituting f_j into Equation 3.25 results in a net aerodynamic influence coefficient matrix

$$[Q_{kk}] = [S_{kj}]\,[A_{jj}]^{-1}\left[D^1_{jk} + ikD^2_{jk}\right] \tag{3.26}$$

Splining is the method of relating the structure and the aerodynamic model. It is the methodology used to relate grid point deflections to the deflections of aerodynamic grid points. The aerodynamic grid point deflection can be shown as

$$\{u_k\} = [G_{kg}]\,\{u_g\} \tag{3.27}$$

where $[G_{kg}]$ is the spline interpolation matrix and $\{u_g\}$ are the grid point deflections. The vector $\{u_g\}$ is the set of global degrees of freedom corresponding to the element degrees of freedom in the vector $\{d\}$ from the Linear Finite Element Statics discussion section. The net aerodynamic influence coefficient matrix can be expressed in structural deflections through the spline interpolation matrix (Equation 3.27)

$$[Q_{gg}] = [G_{kg}]^T\,[S_{kj}]\,[A_{jj}]^{-1}\,[D_{jk}]\,[G_{kg}] \tag{3.28}$$

By using Equations 3.25 and 3.28, structural deflections can be placed in terms of aerodynamic influence matrices and stiffness matrices

$$[K_{gg} - \bar{q}Q_{gg}]\,\{u_g\} + [M_{aa}]\,\{\ddot{u}_g\} = \bar{q}\,[Q_{ax}]\,\{u_x\} + \{P_g\} \tag{3.29}$$

where $[M_{aa}]\,\{\ddot{u}_g\}$ is the mass-inertia term, $\bar{q}\,[Q_{ax}]\,\{u_x\}$ is the aerodynamic trim term, and $\{P_g\}$ are the applied forces. For this study, the fuel weight was not included in the mass-inertia term. It was included as an applied force in $\{P_g\}$.

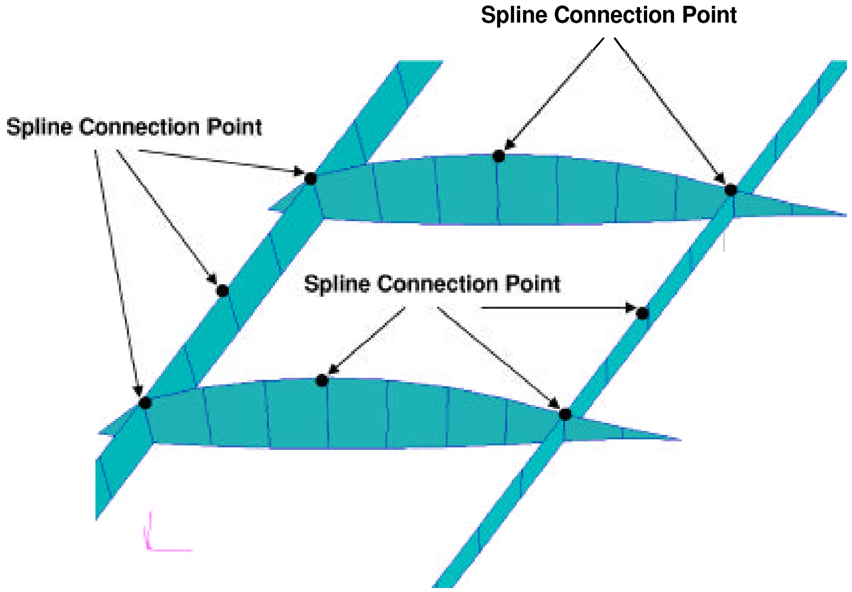

Figure 3.8 Spline Locations Used in Aerodyanmic Model

The splines were connected to grids on the substructure so that the integrated aerodynamic forces were properly transferred through stiffer points in the wing box. The splines were only connected to the top portion of the wing since the wing box will transfer forces from the top part of the wing box to the bottom through the spars and ribs. The locations of the spline connection points are shown in Figure 3.8.

The aerodynamic panels were distributed as shown in Figure 3.9. The front-wing, aft-wing, joint-wing, and outboard-wing sections were each assigned ten rows and ten columns of aerodynamic panels for a total of 100 panels for each wing section. Each wing section was modeled equally due to an equal number of aerodynamic panels for each wing section. Additionally, the camber of the LRN-1015 airfoil was included in the aerodynamic influence matrix.

The main trim control mechanisms were angle of attack and aft-wing twist angle for the maneuver load cases. The FlightLoads model was allowed to change these two mechanisms to trim for lift load factor and for zero pitching moment of the aircraft. The aft-wing was assumed to structurally twist to facilitate pitch trim.

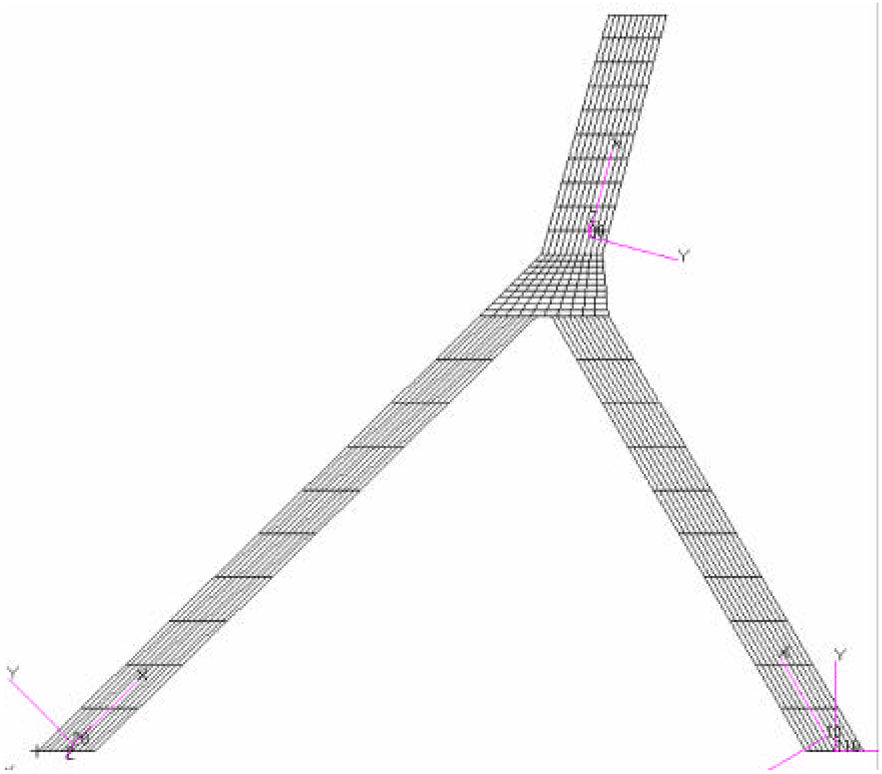

Figure 3.9 Aerodynamic Paneling

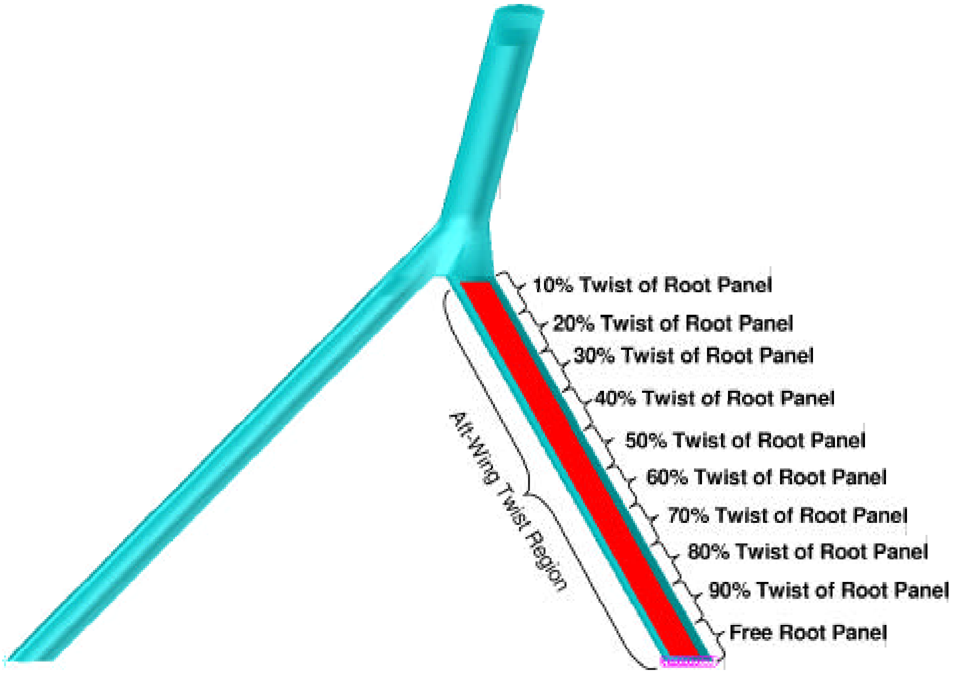

Figure 3.10 Linearly Tapered Aft-Twist Control Mechanism

The aft-twist mechanism was linearly tapered. The aft-wing-twist mechanism was unique, since it involved a tapered inclination angle from the aft wing root to the joint section. The twist that occurred at the root of the aft wing controlled or governed the twist throughout the remaining span of the aft wing. The aft-wing was broken up into 10 separate panels. The first panel (0%-10% aft-wing span) of the aft-wing span was allowed to twist freely. The second panel (10-20% aft-wing span) was forced to twist 90% of the first panel. The panels continued in this pattern through the length of the aft-wing (Figure 3.10).

3.12 NASTRAN Optimization Theory and Application

Design optimization is the process of generating an improved design. The process includes using sensitivity analysis to search for a minimized or maximized objective function which is held to a certain set of constraints. Sensitivity analysis is a process that computes the rates of changes of responses to design parameters [10]. An optimization problem is first defined by the objective function

$$F\left(\vec{x}\right) \tag{3.30}$$

which is subject to inequality constraints:

$$g_j\left(\vec{x}\right) \leq 0 \qquad j = 1, ..., n_g \tag{3.31}$$

and side constraints:

$$x_i^l \leq x_i \leq x_i^u \qquad i = 1, ..., n \tag{3.32}$$

where the design variables are properties of the model:

$$\vec{x} = [x_1, x_2, ..., x_n] \tag{3.33}$$

The design variables in this model were the element thicknesses. By varying the thicknesses of the ribs, spars, and skins of the wing, the wing was able to resist strain and buckling effects, which were applied as inequality constraints. The side constraints were defined as a minimum and maximum gauge for each composite ply.

For this study, the goal was to find the lightest joined-wing aircraft. The objective function was the weight of the aircraft and the goal was to minimize the objective function. In NASTRAN, the weight objective function was defined by calculating the weight of both the designable finite element material and the centralized mass points. The concentrated masses defined non-wing characteristics such as fuselage, engine, tail, and payload weight. The assumed mass size and mass location of each non-wing structural part are listed in Table 3.7 [15]. The Payload location was the only mass that was flexibly defined as a design variable in the single configuration optimization model to ensure static aerodynamic stability.

Joined-Wing Part	**Mass (kg)**	**Initial CG x-location**	**Flexible?**
Fuselage	2180.0	Centered Front & Aft Wing	No
Fuselage Fuel	40.0	Centered Front & Aft Wing	No
Engine	1760.0	Center of Aft Wing Root	No
Payload	3440.0	2.0 m Forward of Front Wing Root	Yes
Vertical Tail	100.0	Center of Aft Wing Root	No

Table 3.7 Assumed Concentrated Masses of Non-Wing Structures

The inequality constraints were defined as strain and buckling limits. The optimizer stepped toward a design point which did not exceed a certain composite strain limit and would not be lower than a certain buckling eigenvalue. These were the main driving constraints that kept the aircraft from being extremely lightweight.

Generally speaking, the sensitivity analysis defines gradients where the optimization will step towards an optimum solution. NASTRAN uses analytical expressions to define local search gradients. The approximating functions are Taylor series expansions of the objective function and the applied constraints. The Taylor series expansion is only a linear approximation:

$$\tilde{f}(x^0 + \Delta x) = f(x^0) + \left[\frac{df}{dx}\right]_{x^0} \cdot (\Delta x) \tag{3.34}$$

where x^0 is the current design variable value, Δx is the step size, and $\left[\frac{df}{dx}\right]_{x^0}$ is the first derivative value at x^0. Utilizing Equation 3.34, the approximations of the objective and constraint functions in vector form become

$$\tilde{F}(\vec{x}^0 + \Delta\vec{x}) = F(\vec{x}^0) + [\bigtriangledown F]_{\vec{x}^0} \cdot (\Delta\vec{x}) \tag{3.35}$$

$$\tilde{g}_j(\vec{x}^0 + \Delta\vec{x}) = g_j(\vec{x}^0) + [\bigtriangledown g_j]_{\vec{x}^0} \cdot (\Delta\vec{x}) \tag{3.36}$$

This method was used in numerical optimizations. NASTRAN conducted a finite element analysis which, in conjunction with Equations 3.35 and 3.36, created a

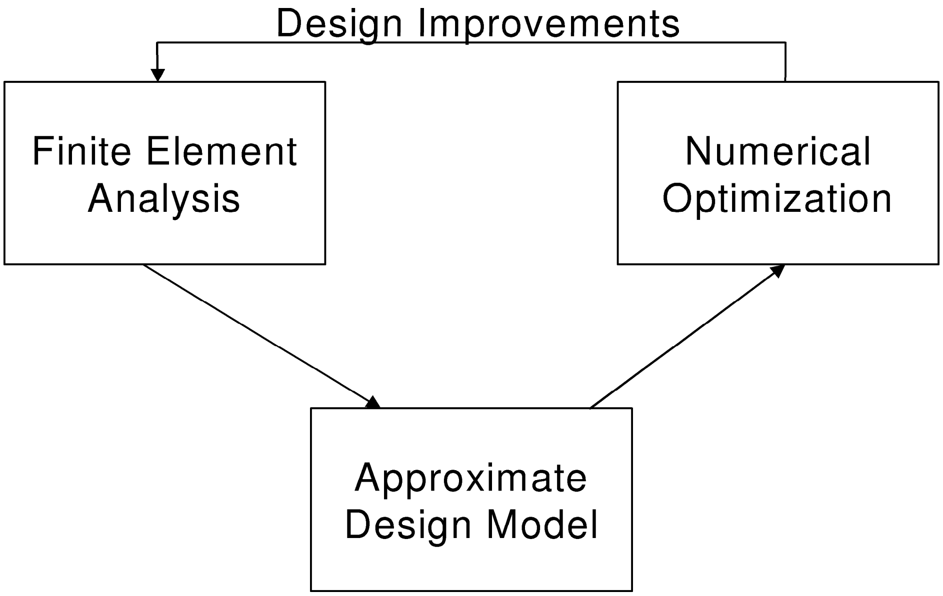

Figure 3.11 Coupling of Numerical Optimization and Finite Element Analysis

locally defined design model. NASTRAN then used standard numerical methods on the approximate model to define a new and better design model for the next finite element analysis [22]. Since the approximate model can only be defined locally, the new finite element design space had different levels of constraints and objective definitions. To ensure that optimizer stays near the approximate model, move limits were imposed on the physical variables (element thicknesses). The coupling of the finite element analysis and the numerical optimization is shown in Figure 3.11.

The above process continued until a maximum number of design improvements were reached or the solution converged to a point where the maximum constraint only exceeded its limit by no more than 0.5% and the weight change was less than 0.001 kg.

3.13 Single Configuration Weight Minimization Process

Due to NASTRAN software limits, buckling analysis could not be applied to a static aerodynamic analysis within a single run. In addition, information for an instantaneous gust load case could not be gathered until a previous run for 1.0G cruise was completed. Since the gust cases and buckling cases were proven to be critical, these had to be included in the configuration design. Three separate phases were accomplished to obtain a single optimized point with a full instantaneous gust and buckling analysis.

The first phase included standard FlightLoads trim cases for maneuver loads and static vehicle weight accounting for impact load sets. The gust loads were not included in the first phase. A 1.0G trim case was used to prepare for the next phase's instantaneous gust case. Loads for all relevant cases were generated from a sample PanAir model and then applied in the first run for initial estimate purposes only. The first phase set up the initial problem and weight estimates.

The second phase included the same maneuver static trim and impact load sets as before except the static trimmed forces from the first run were applied as buckling load sets for buckling analysis. In addition, changes in angles of attack for the instantaneous gust cases were calculated and then added as increments to 1.0G trim angle of attack in phase two. Instantaneous gust loads were applied in this phase through FlightLoads analysis, but the loads could not be applied to a buckling analysis until the gust loads from FlightLoads were post-processed as static loads.

Phase three included regular maneuver data, instantaneous gust information, and impact data for both static aerodynamic analysis and buckling analysis. Loads from an instantaneous gust case were applied to a buckling analysis.

NASTRAN computed element displacements and strains due to the load conditions. User-defined design variables were employed to resize each element within the wing-box structure, utilizing both a strain and buckling analysis.

The NASTRAN optimizer resized each element to provide the minimum weight using gradient based design. The optimizer worked under the constraints that all elements must have a 1.5 maximum factor of safety applied to the allowable fiber strain and a buckling limit load of 1.5 times the design load.

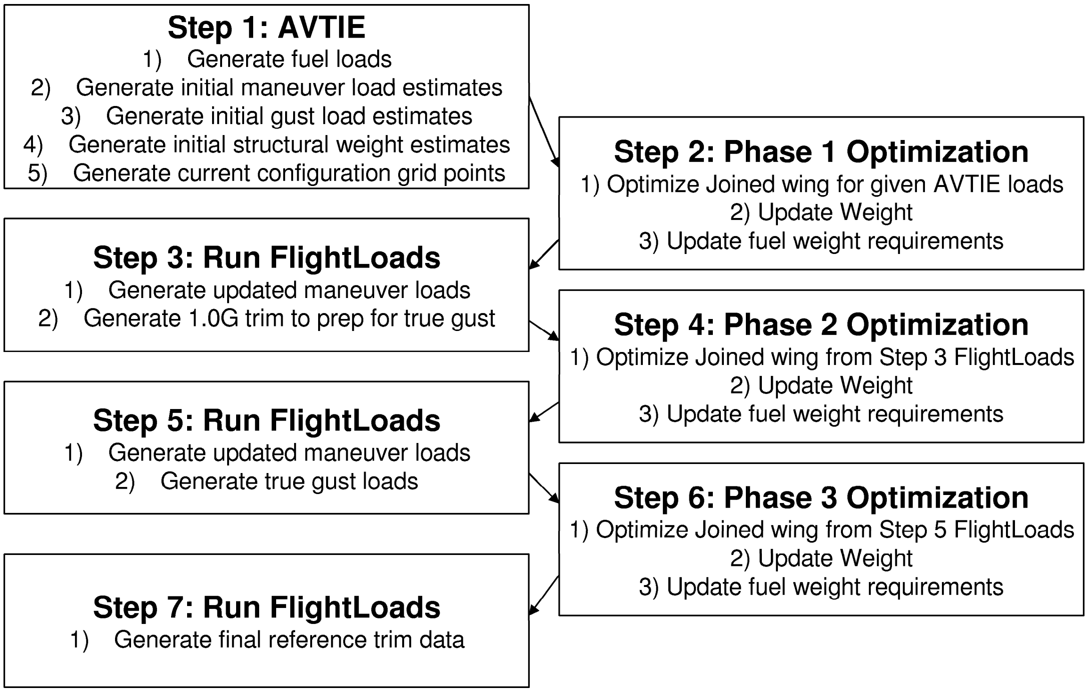

Figure 3.12 AVTIE, FlightLoads, NASTRAN Optimization Phasing Process

Since the NASTRAN design model included over 22,800 thickness design variables, a design space reduction had to exist. The thickness variables were estimated in terms of independent variables in the form of polynomial curve fits

$$t_i = C_0 + C_1 x_i + C_2 x_i^2 + C_3 x_i^3 \tag{3.37}$$

where x is represents the normalized spanwise location of the designable element and $x = 0$ is at the wing section root and $x = 1$ is at the tip of the wing section. The curve fits were separated by part location. For example, the front wing skins were sized by a different polynomial than the outboard wing spars. In addition, each composite ply was controlled by separate polynomials. For a third order polynomial curve fit, there were 528 independent design variables.

A higher order polynomial curve more closely fits a fully strained design. A higher order curve fit will be able to "turn" more and better fit an element by element design and will be capable of a lower minimized weight. However, a lower

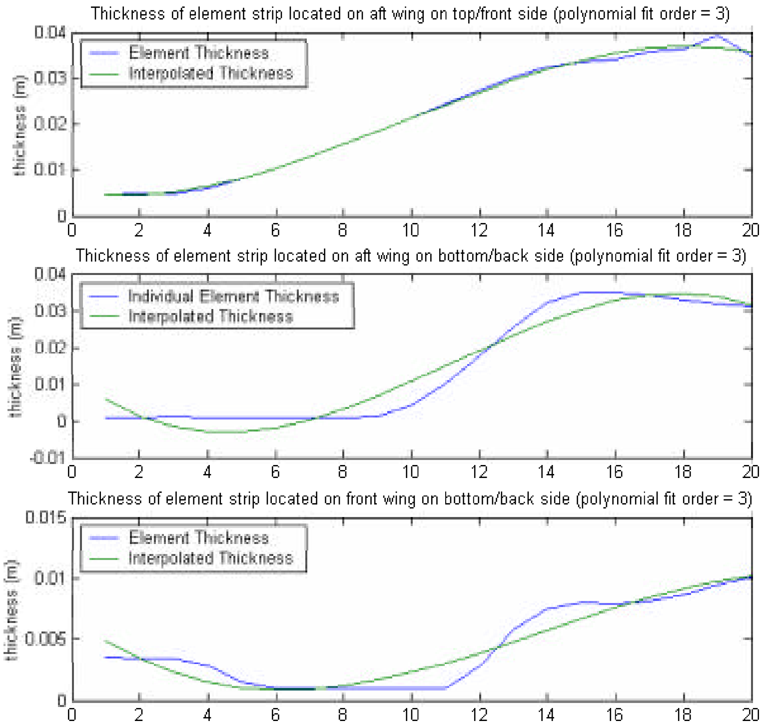

Figure 3.13 Third Order Interpolation Curve Fit of Recent Fully Strained Optimized Structures

order curve fit will improve optimization run times, because there are fewer design variables. A balance between lower and higher order was found by comparing thickness distribution profiles from Roberts' fully strained model [15]. As shown in Figure 3.13, a third order polynomial interpolation curve fit came very close to Roberts' model, while it ran the optimization within a reasonable amount of time. By using polynomial curve fits, most points on the curve were thicker than the minimum thickness allowed for a fully strained design. The model became a conservative model due to the extra material used.

The curve fits were used in several chordwise strips in each wing section. As part of establishing flexibility in the design model, the strip of elements just aft of the leading spar and the strip of elements just forward of the trailing spar were controlled by separate polynomial curves. This ensured that the unique joined-wing material placement noted by Wolkovich was allowed to occur in the optimization [24].

Through the combination of linear strain and buckling analysis, the final thicknesses in the weight optimized design was compared to a non-linear fully strained design. A non-linear analysis of the final optimized configuration was completed to check error magnitude.

3.14 Response Surface Methodology

A response surface is a geometric representation of a response function [11]. For this study, a sample of various configuration data points were created to produce a function which represented weight with respect to six key variables as shown in Table 3.2. A second order response surface was created by sampling the entire design space.

As an example, a simple response surface can be defined as:

$$\hat{y} = \beta_0 + \beta_1 x_1 + \beta_2 x_2 \tag{3.38}$$

where β_i are the experimentally evaluated coefficients and x_i are the design variables [11]. Since β is defined through experimental means, a certain number of design variable samples need to be taken such that the response surface closely fits the observed experimental values. β is determined as:

$$\hat{\beta} = \left(X^T X\right)^{-1} X^T y \tag{3.39}$$

where X is an $n \times p$ matrix and y are the observed responses. Here, n is the sample number, or rather, the number of observed responses and p is the number of coefficients [11].

The R^2 value is the response surface regression fit value which objectively defines how well the response surface fits the observed design space. R^2 is defined through:

$$R^2 = \frac{\hat{y}^T \hat{y} - n\bar{y}^2}{y^T y - n\bar{y}^2} \tag{3.40}$$

where $\hat{y}$ are the fitted responses and $\bar{y}$ is the average observed value.

3.15 Configuration Optimization Process

To find an optimized joined-wing configuration, a design of experiments was created. Due to long analysis times for a single configuration, a limited number of configurations were used to find an overall optimized wing set.

Classical function minimization techniques could not be used in this study due to the large processing size of the weight optimization techniques and lack of aerodynamic structural gradients. A sample set of various configurations were used to create response surfaces for the system. Classical minimization techniques were utilized on the response surface since the optimal point was easily determined from a second order response surface.

The optimization was conducted as a two step process. A set number of configurations was created using the AVTIE interface. A weight optimized aircraft weight was found for each wing configuration using FlightLoads and NASTRAN structural optimization. MatLab [9] [18] was used as an integration tool between all the aforementioned software packages. MatLab pre and post processed all AVTIE, FlightLoads, and NASTRAN optimization runs. The MatLab process is discussed in Appendix B.

The main goal of this study was to obtain general relationships between each pair of configuration design variables. A total of 15 relationship combinations exist for six independent design variables where only a maximum of two design variables were compared for each combination. The sampling space used to generate the response surface is symmetric across a two-design variable comparison. Only two-level design variable interactions were allowed in the response surface equation. In addition, the equation is second order for each individual design variable. Taking the set of minimized weights for all configurations, a function in terms of the configuration design variables was created using response surface methodology.

$$f = C_0 + \sum_{i=1}^{6} C_i x_i + \sum_{j=1}^{6} \sum_{k=1}^{6} C_{jk} x_j x_k \tag{3.41}$$

From this function, with its determined coefficients, classical minimization optimization techniques were used to extrapolate an optimized configuration solution. The overall configuration optimization process is shown in Figure 3.14.

Four sample configuration points were taken for each combination to create the first 60 response surface data points. The four data points were at 70.7% of the maximum and 70.7% of the minimum of each variable in each two variable combination. This sampling matches the two-level interaction terms assumed in the response surface function (Equation 3.41). Additionally, each variable was sampled at its maximum and minimum while maintaining the other configuration design variables at their midpoint (12 data points). These samples follow the non-interaction terms of the assumed response surface. Finally, two baseline data points were used. One baseline configuration set all six design variables to their midpoints. The other baseline data point was the configuration used in Roberts' study. The two baseline data points were the 73^{rd} and 74^{th} configuration data points which resulted in a total of 74 total data points to create the final response surface. A two-dimensional sample space example is shown in Figure 3.15. The sampling space is circular around the center point. This results in a constant radius away from the center of the design space.

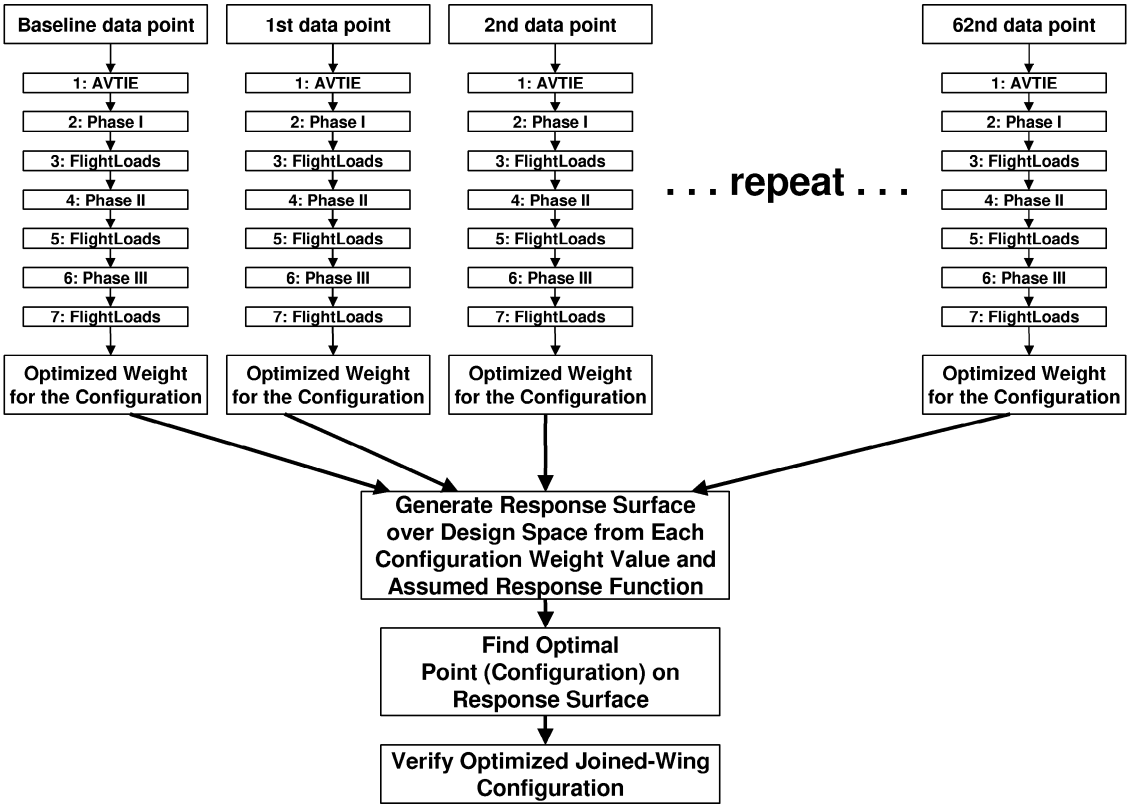

Figure 3.14 Overall Configuration Optimization Process

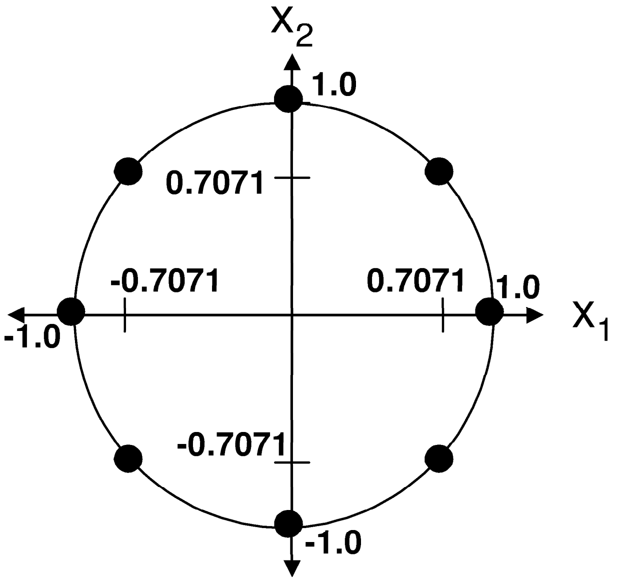

Figure 3.15 Example of a Two-Dimensional Sample Space

IV. Results

4.1 Non-Linear Comparative Analysis

To check the assumption that buckling constraints in the optimization model are adequate to estimate non-linear effects, a non-linear analysis was conducted on a converged baseline joined-wing model. The model was run through the entire single configuration weight minimization process using buckling and strain constraints. Non-linear tip deflection and strain relationships were compared with a linear analysis of the same joined-wing model. The two critical load cases were analyzed to ensure that the correct constraint design space was considered. For strain, the impact load case was the most critical. For buckling, the impact and turbulent load cases were both found to have local and global critical buckling eigenvalues. Strain results of the impact load case are shown in Figure 4.1.

The impact strain curve shows that the non-linear analysis indicates a reduction in strains as the load factor increases. The structure stiffens as the load factor increases. This makes the applied strain limits a conservative constraint.

The turbulent gust load cases are dependent upon aerodynamic forces. As the wing deflects, the aerodynamic forces change. To account for this in this non-linear analysis comparison, the aerodynamic forces were assumed to always be perpendicular with the wing to account for any level of vertical and lateral deflection. The tip deflections with respect to the load factor are shown in Figure 4.2.

As shown with the non-linear strain relationship of the impact load case, the tip deflections are less than the linear deflections. Again, the structure stiffens as the wing deflects and thus, the current design space is conservative. The aerodynamic loads were not updated through the load history. Instead, a single load case was scaled through a load factor range to determine non-linear deflections. As a wing deflects, the spanwise lift distribution changes and changes the overall forces acting

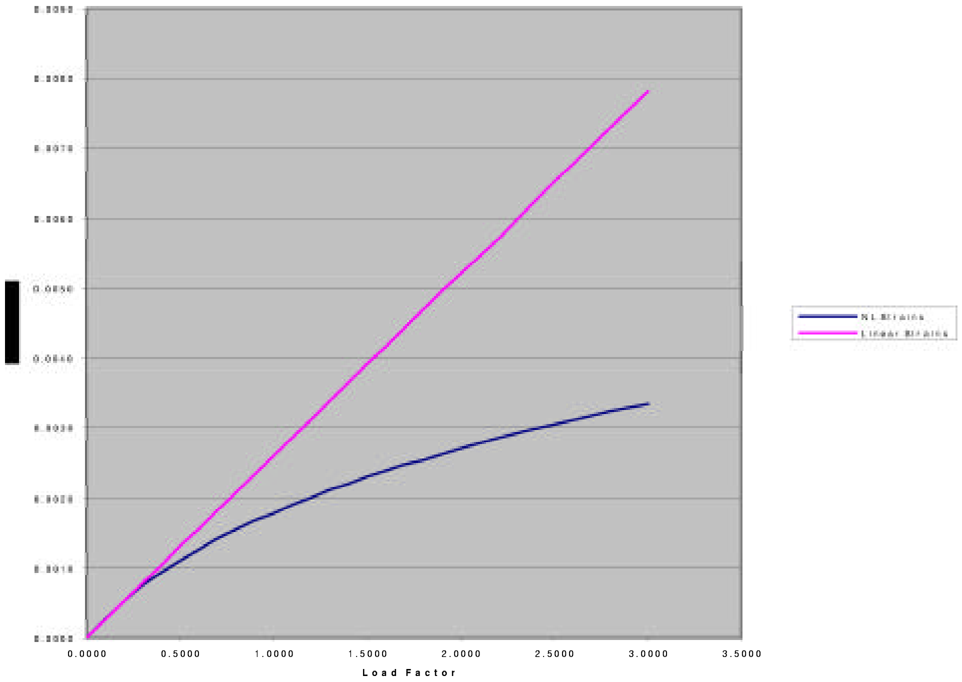

Figure 4.1 Impact Strain Relationships with Load Factor

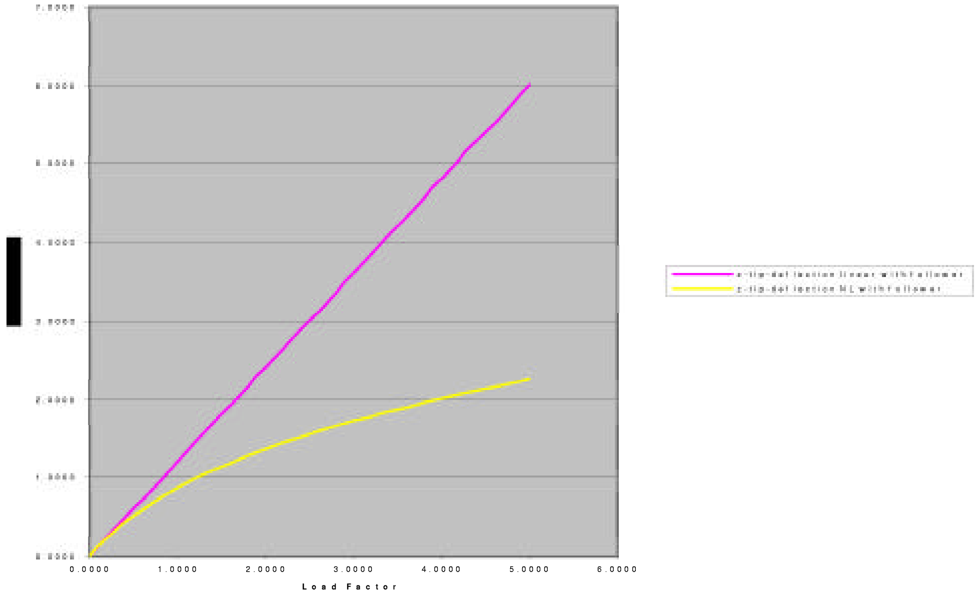

Figure 4.2 Turbulent Gust Tip Deflection Relationship with Load Factor

on the wing. These changes may result in various non-linear aeroelastic effects, which were not modeled. A global buckling instability corresponding to a stiffness softening was not observed with the nonlinear aeroelastic effect. That effect is examined for the optimal configuration in subsection 4.3.3.

4.2 Response Surfaces

4.2.1 Overview.

The response surface was generated through 74 observed configurations. Many more single configurations were optimized to establish a higher fit value for the response surface function. The R^2 value was 0.853. The average difference between the observed and fitted value is 6518 kg. The standard deviation was 24663. These values showed that the response surface only moderately fit the data, which implied that the response surface needed higher level interaction terms or higher order terms.

The response surface graphs are displayed in the next sections by plotting the fitted weight response with respect to two design variables. The two variables of interest were varied from their respective lower and upper bounds. The four other variables are set constant at their midpoints. This is similar to the two-level sampling space discussed in Section 3.15. An important point to consider is that the weight may show a high value for a particular pair of variable values, but the weight for the same two values may be different if the four other variables are not set at their respective normalized midpoint. The curves were well defined at the variables' midpoint regions. Moving a combination of the configuration variables away from the midpoint results in a region that is not as accurate.

4.2.2 Front Wing Sweep Angle vs. Outboard Sweep Angle.

The outboard wing sweep angle, with respect to any front wing sweep angle, drives towards a negative (forward) swept angle to create a lighter weight aircraft. Conversely, the front wing sweep angle minimizes weight towards 37° with respect to any outboard

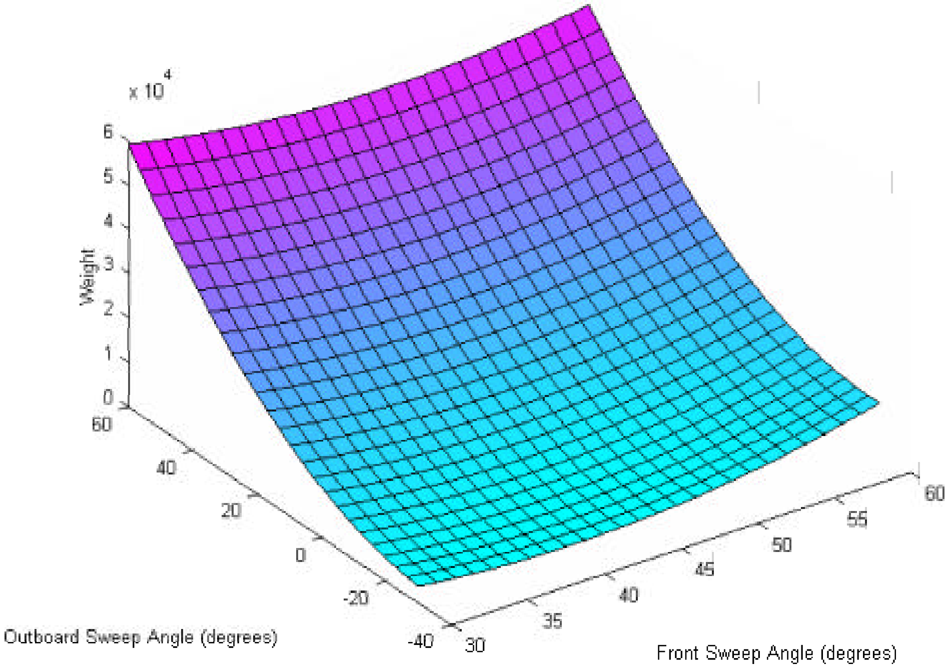

Figure 4.3 Response Surface of Front Wing Sweep vs. Outboard Wing Sweep

sweep angle. Figure 4.3 shows the response surface interaction between the front and outboard sweep.

4.2.3 Front Wing Sweep Angle vs. Aft Sweep Angle. Figure 4.4 shows that a high front and aft wing sweep angle produces a very heavy joined-wing sensor-craft. Since the front and aft wing control the majority of the wing surface area, higher sweep angles imply higher weight. Alternatively, lower sweep angles mean a lighter weight sensor-craft. These variables are highly coupled. Relative to the other, the variables both tend to move to an unswept angle to create the lowest weight configuration.

4.2.4 Front Wing Sweep Angle vs. Joint Location. As shown in Figure 4.5, as the front wing sweep angle increases, the position of the joint location becomes important. At a front wing sweep of 60 °, the joint location moves towards 0.5. At

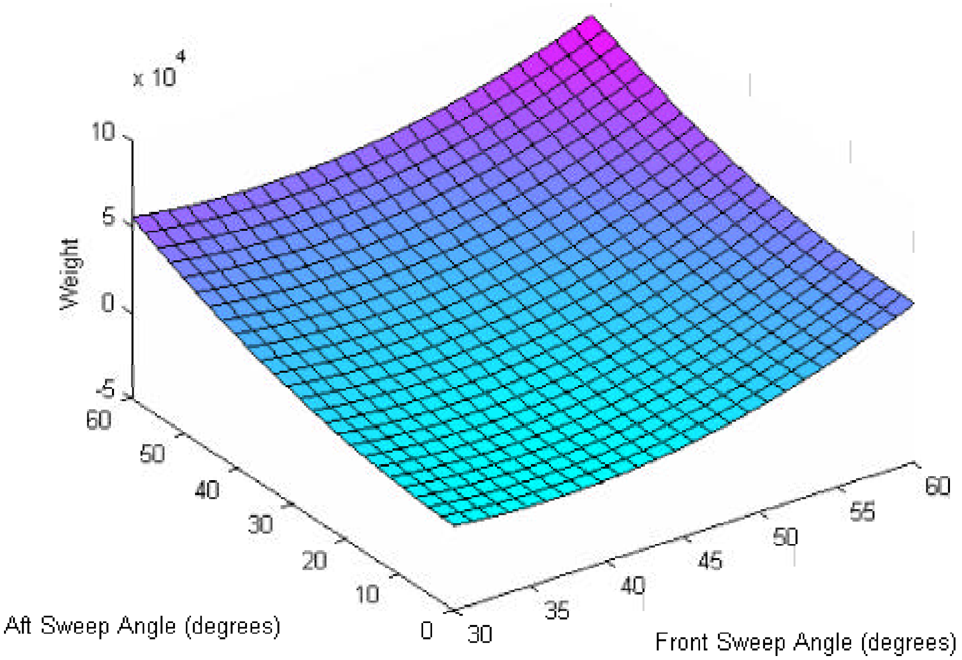

Figure 4.4 Response Surface of Front Wing Sweep vs. Aft Wing Sweep

a front wing sweep of 30°, the joint location is driven more to its midpoint rather than its minimum. Likewise, the front wing sweep angle at a high joint location is driven to its lower bound. At a low joint location value, the front wing sweep angle moves towards 42° rather than its lower bound. Additionally, a high front wing sweep angle and a high joint location creates a front and aft wing with long wing spans and thus, a higher total wing surface area and a higher weight sensor-craft.

4.2.5 Front Wing Sweep Angle vs. Vertical Offset. For a constant vertical offset, the front wing sweep angle does not vary significantly (Figure 4.6). In contrast, the vertical offset drives strongly towards 0.0m, no matter what the front wing sweep angle is. These two configuration design variables do not have noteworthy interaction.

4.2.6 Front Wing Sweep Angle vs. Airfoil Thickness to Chord Ratio. Figure 4.7 displays the minimal interaction between the outboard wing sweep angle

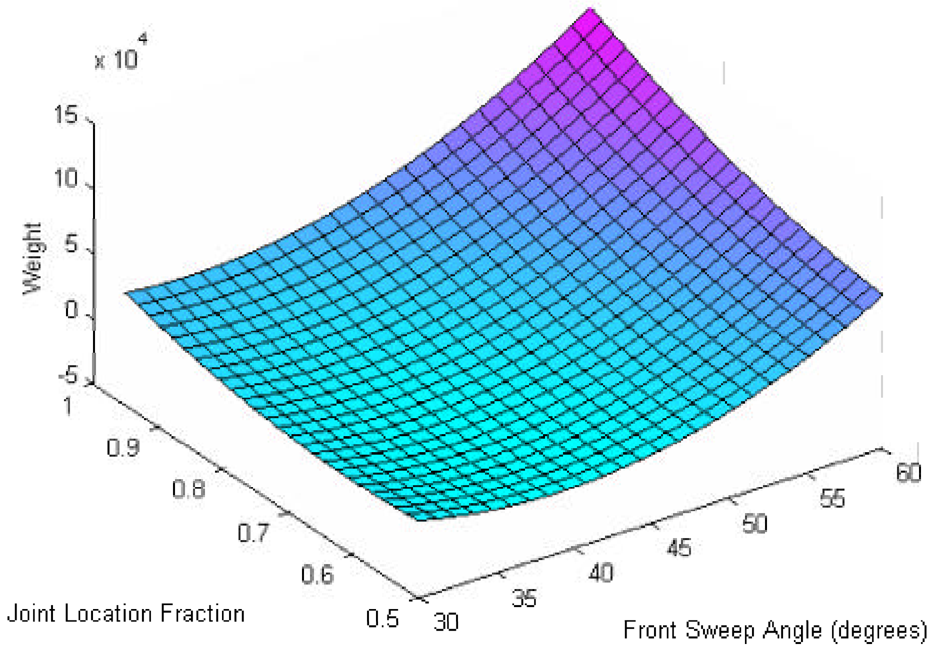

Figure 4.5 Response Surface of Front Wing Sweep vs. Joint Location

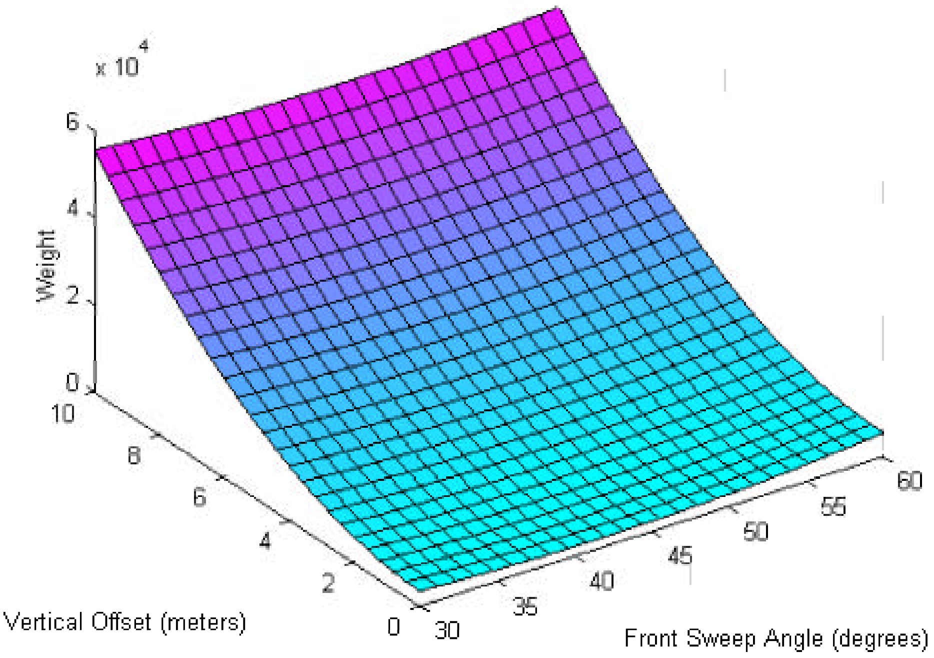

Figure 4.6 Response Surface of Front Wing Sweep vs. Vertical Offset

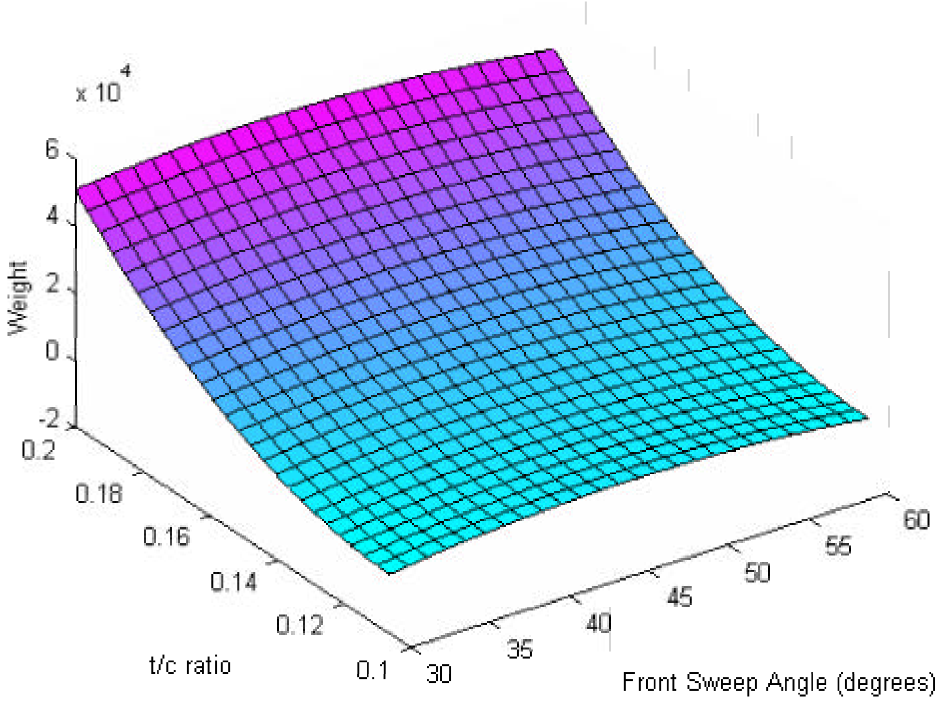

Figure 4.7 Response Surface of Front Wing Sweep vs. t/c

and the vertical offset. No matter what the constant value of the vertical offset is, the outboard wing sweep angle moves towards 14° to create the lightest weight configuration. For a set outboard wing sweep angle, the vertical offset stays at a constant value.

4.2.7 Outboard Sweep Angle vs. Aft Sweep Angle. As shown in Figure 4.8, a constant outboard wing sweep angle drives the aft wing sweep angle stays constant. Additionally, for a constant aft wing sweep angle, the outboard wing sweep angle moves towards its midpoint. There is very little interaction between these two configuration design variables.

4.2.8 Outboard Sweep Angle vs. Joint Location. A constant outboard wing sweep angle produces a constant joint location value (Figure 4.9). In contrast, for a constant joint location, the outboard wing sweep angle tends strongly towards its

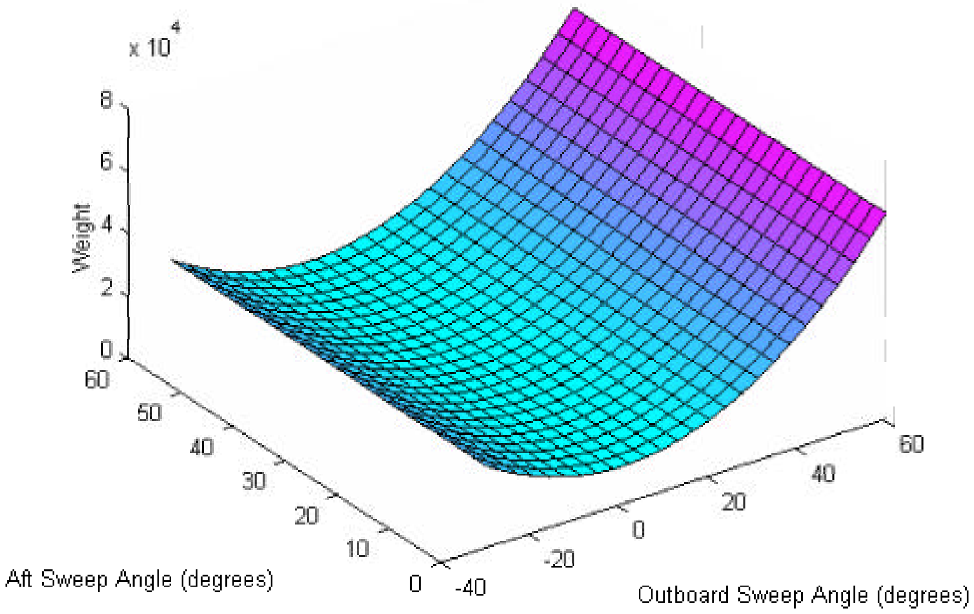

Figure 4.8 Response Surface of Outboard Wing Sweep vs. Aft Wing Sweep

midpoint to create a lightweight aircraft. Surprisingly, interactions between these two variables are almost non-existent. Convention says that as the joint location moves towards the tip, the outboard wing sweep angle requirements to create a lighter weight aircraft would be less significant.

4.2.9 Outboard Sweep Angle vs. Vertical Offset. The vertical offset does not change significantly for a constant outboard wing sweep angle (Figure 4.10). However, for a constant vertical offset value, the outboard wing sweep angle strongly tends toward 13 ° between its lower and upper bound. The two-level interaction between the outboard wing sweep and vertical offset is negligible.

4.2.10 Outboard Sweep Angle vs. Airfoil Thickness to Chord Ratio. Figure 4.11 shows that the weight response with respect to the outboard wing sweep angle diverges away from its midpoint in either direction when given a constant airfoil thickness to chord ratio. This shows that the outboard wing sweep angle is pushed

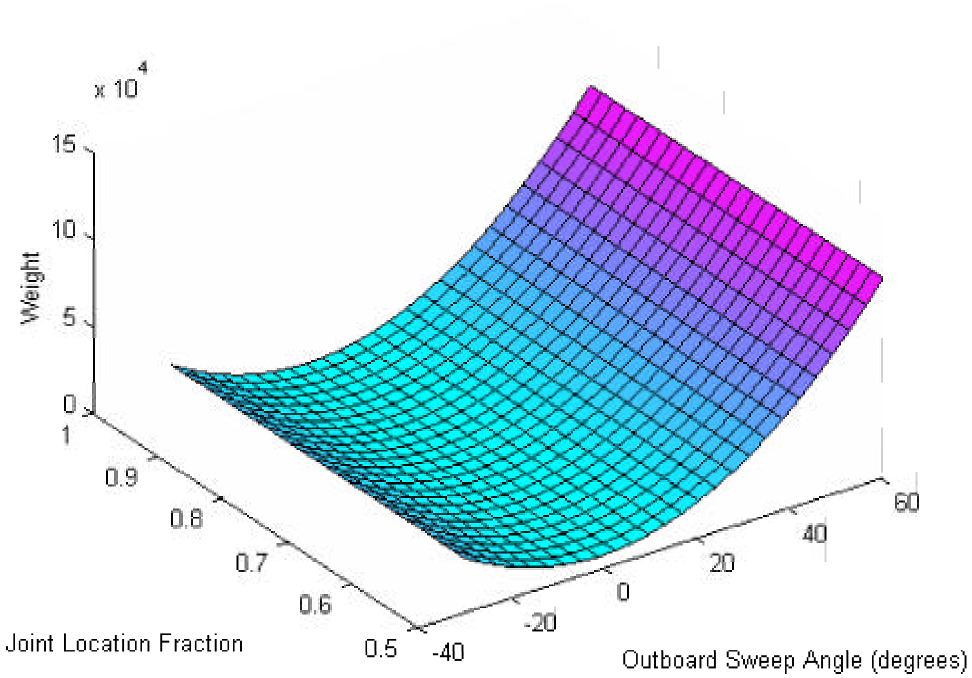

Figure 4.9 Response Surface of Outboard Wing Sweep vs. Joint Location

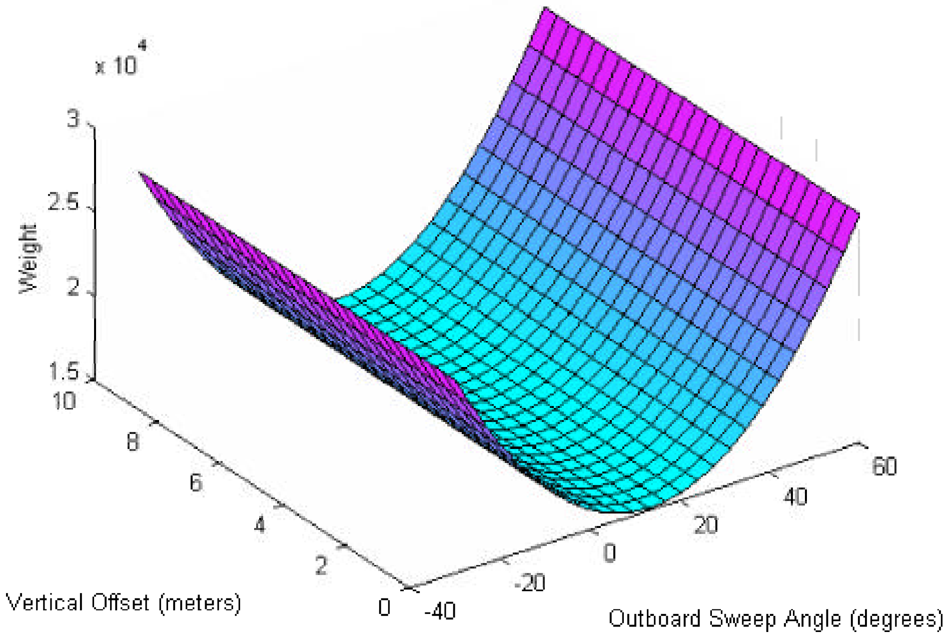

Figure 4.10 Response Surface of Outboard Wing Sweep vs. Vertical Offset

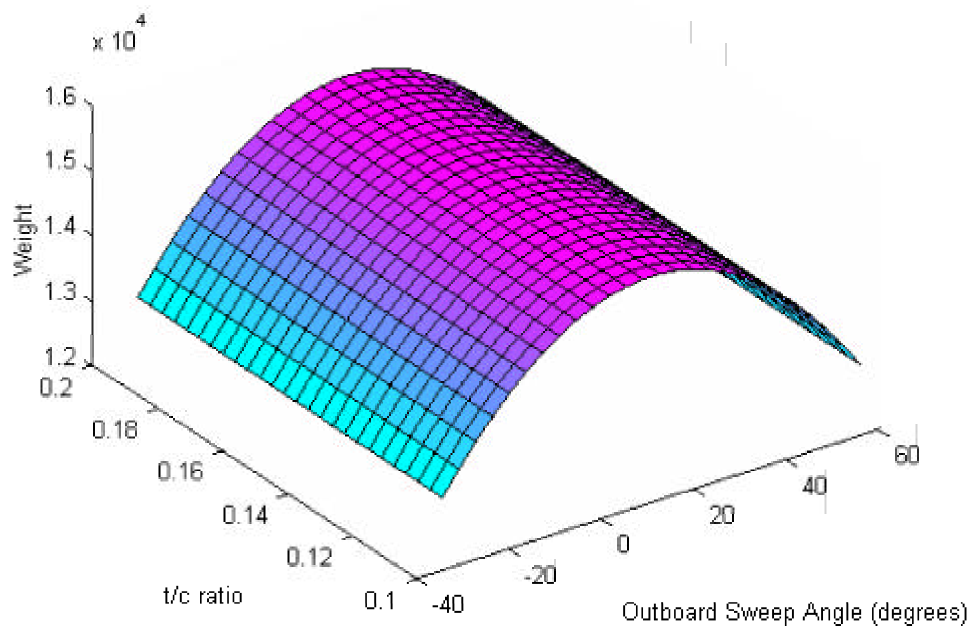

Figure 4.11 Response Surface of Outboard Wing Sweep vs. t/c

towards its upper or lower bound to create a lightweight aircraft. For a constant outboard wing sweep angle, the thickness to chord ratio remains constant.

4.2.11 Aft Sweep Angle vs. Joint Location. A high weight is created for a high aft wing sweep angle. Conversely, a low aft wing sweep angle has a much lower aircraft weight. This is true for any joint location value. Alternatively, for a constant joint location, the aft wing sweep angle moves towards a value lower than its midpoint. This is shown in Figure 4.12.

4.2.12 Aft Sweep Angle vs. Vertical Offset. Similarly to aft sweep vs. joint location (Section 4.2.11), the weight response for a high aft wing sweep value is much higher than when the aft wing sweep angle is low when the vertical offset is constant (Figure 4.13). For a constant aft wing sweep, the vertical offset does not change. Minimal interaction occurs between these two configuration variables.

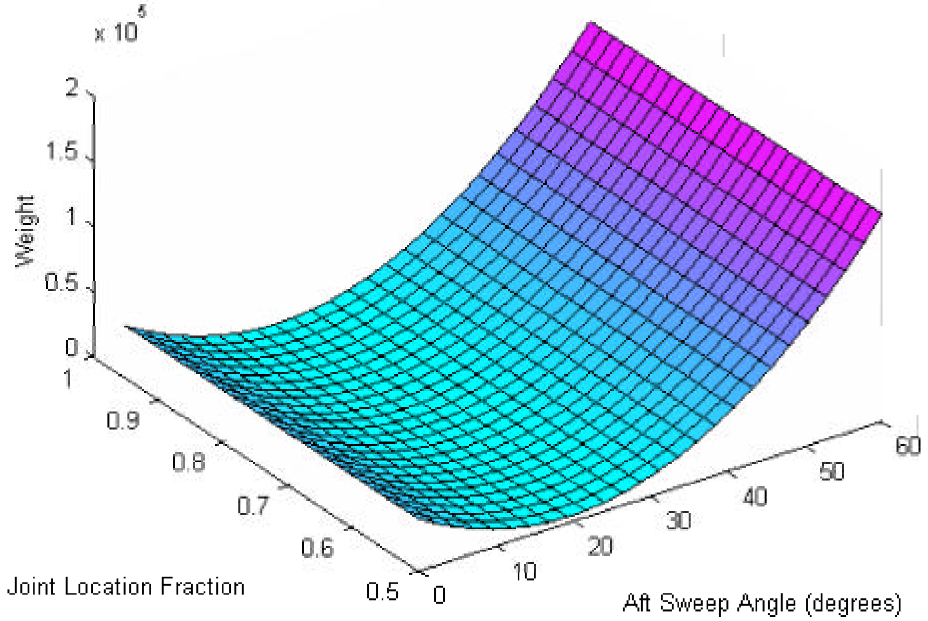

Figure 4.12 Response Surface of Aft Wing Sweep vs. Joint Location

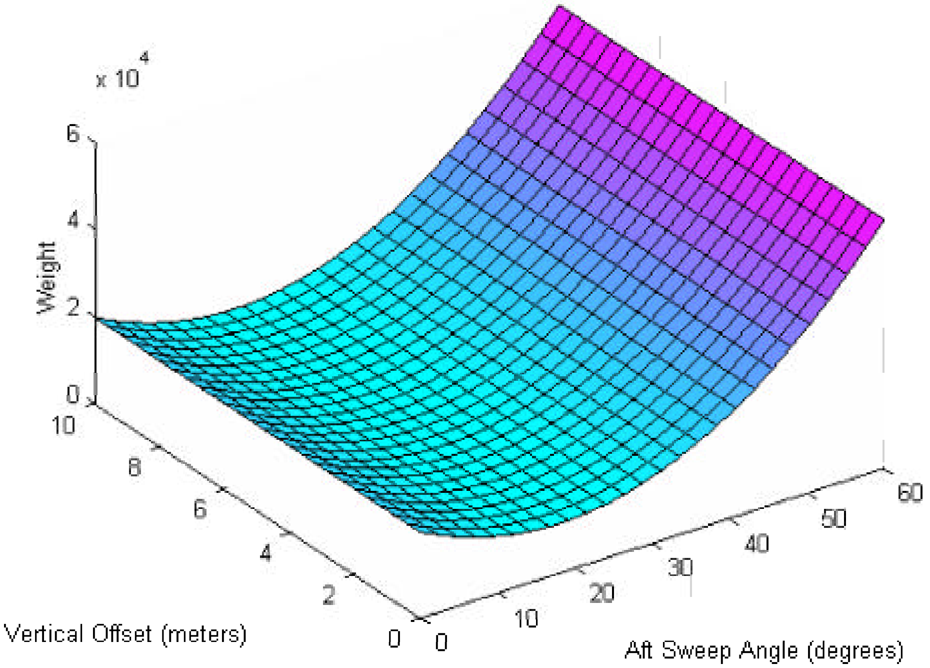

Figure 4.13 Response Surface of Aft Wing Sweep vs. Vertical Offset

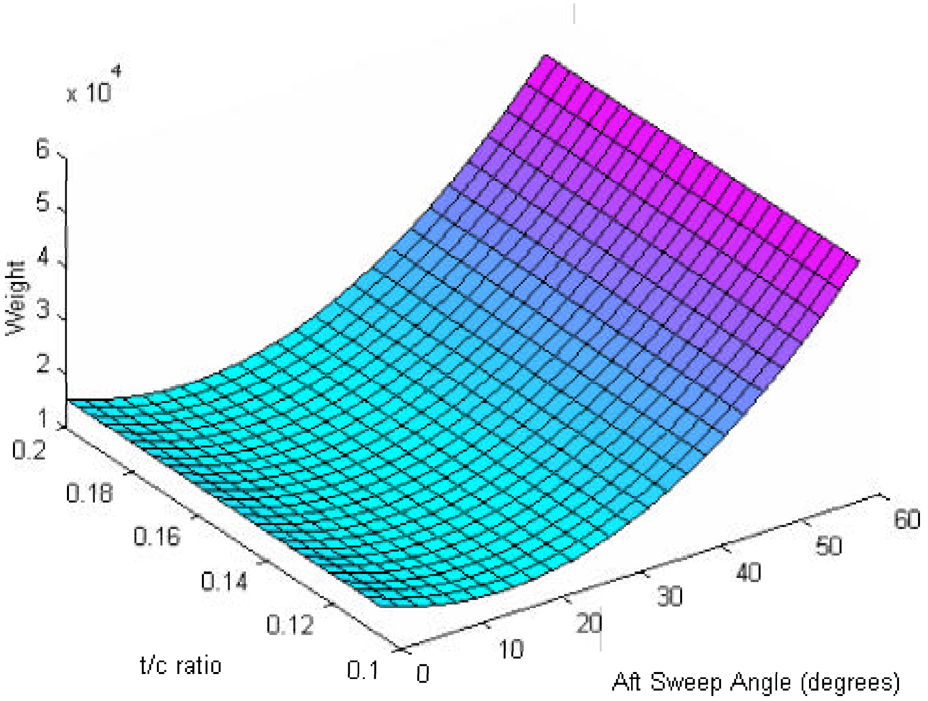

Figure 4.14 Response Surface of Aft Wing Sweep vs. t/c

4.2.13 Aft Sweep Angle vs. Airfoil Thickness to Chord Ratio. Similarly to Sections 4.2.11 and 4.2.12, a higher aft wing sweep angle produces a higher weight than a lower aft wing sweep angle for any value of t/c. It can also be determined that for a constant aft wing sweep angle, the thickness to chord ratio does not change. Very little interaction occurs when comparing aft wing sweep with the airfoil thickness to chord ratio (Figure 4.14).

4.2.14 Joint Location vs. Vertical Offset. The joint location tends towards its lower bound (0.5) for any constant vertical offset (Figure 4.15). For any constant joint location, the vertical offset does not produce a different weight. Very little interaction occurs between joint location and vertical offset.

4.2.15 Joint Location vs. Airfoil Thickness to Chord Ratio. A joint location increase, makes the weight of the aircraft increase for a constant t/c. For a

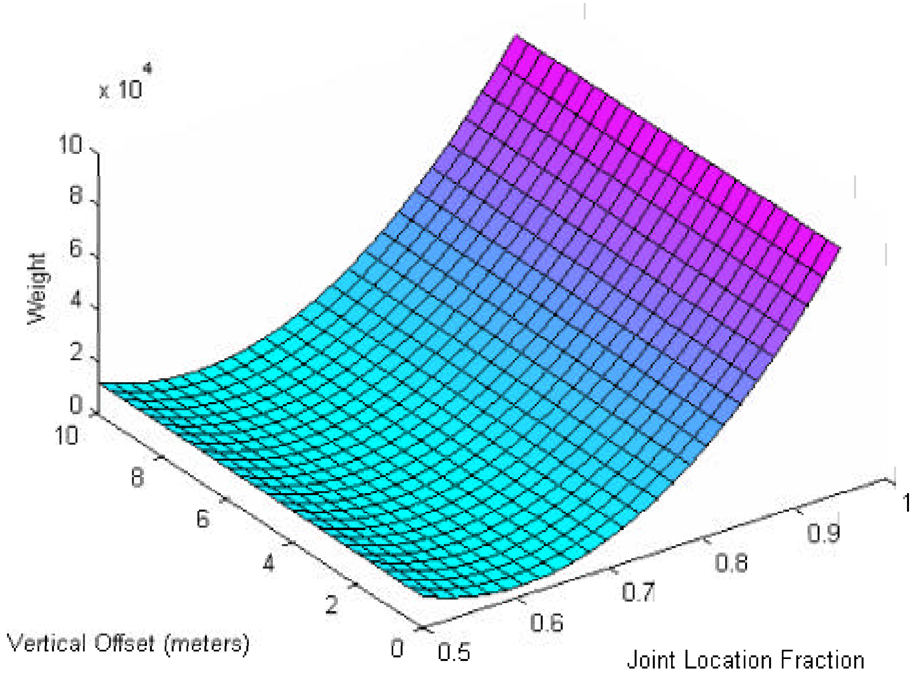

Figure 4.15 Response Surface of Joint Location vs. Vertical Offset

constant joint location, the thickness to chord ratio creates a constant weight. This is displayed in Figure 4.16. It is significant that the t/c ratio does not vary for any constant joint location. A high joint location would require a high airfoil thickness to resist high bending moments incurred from a long outboard wing section. More material placement in the skins can counteract this, but surprising it is still lightweight to do use that methodology.

4.2.16 Vertical Offset vs. Airfoil Thickness to Chord Ratio. With respect to t/c, a decreasing weight value is generated for a higher vertical offset value. The vertical offset can diverge from its midpoint for a set thickness to chord ratio. The vertical offset is pushed towards its lower or upper bound when t/c is constant (Figures 4.17 and 4.18). Surprisingly, minimal interaction occurs between these two variables. A higher vertical offset would require a lower airfoil thickness to resist bending since the front or aft wing would behave as a strut and provide a

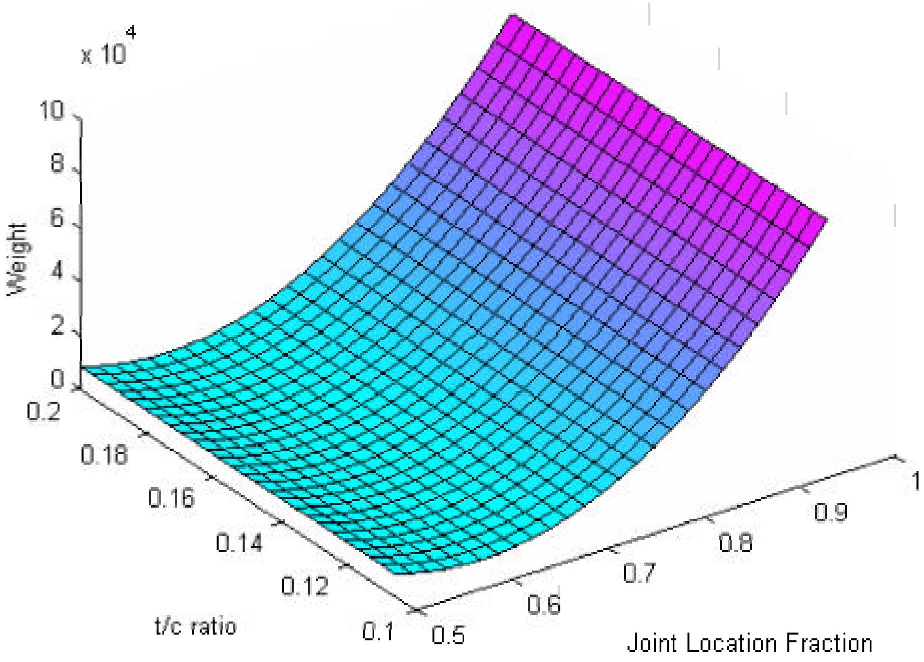

Figure 4.16 Response Surface of Joint Location vs. t/c

vertical resistance to bending. I high airfoil thickness should be required to create a lightweight aircraft when the vertical offset is low since a high airfoil thickness would be the only resistor to vertical bending. The model placed more material on the top skins to compensate for a vertical bending moment.

4.3 Optimal Point Verification

4.3.1 Determined Optimal Configuration. The response surface had three local optimal points, depending upon the initial starting position of the optimization. This was due to negative-definite and non–positive definite Hessians existing in the response surface. As shown in Figure 4.17, the relationship between the airfoil thickness to chord ratio and the vertical offset could push the minimal weight to either the lower or upper bound of the vertical offset variable. In these situations, the estimated optimal weight can be "trapped" at a lower or upper bound depending

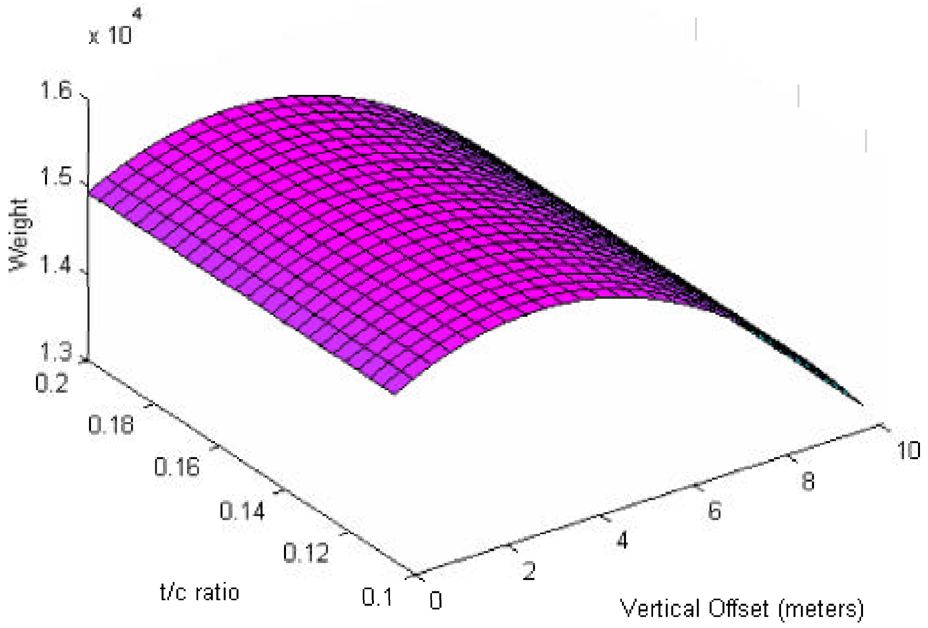

Figure 4.17 Response Surface of Vertical Offset vs. t/c (View 1)

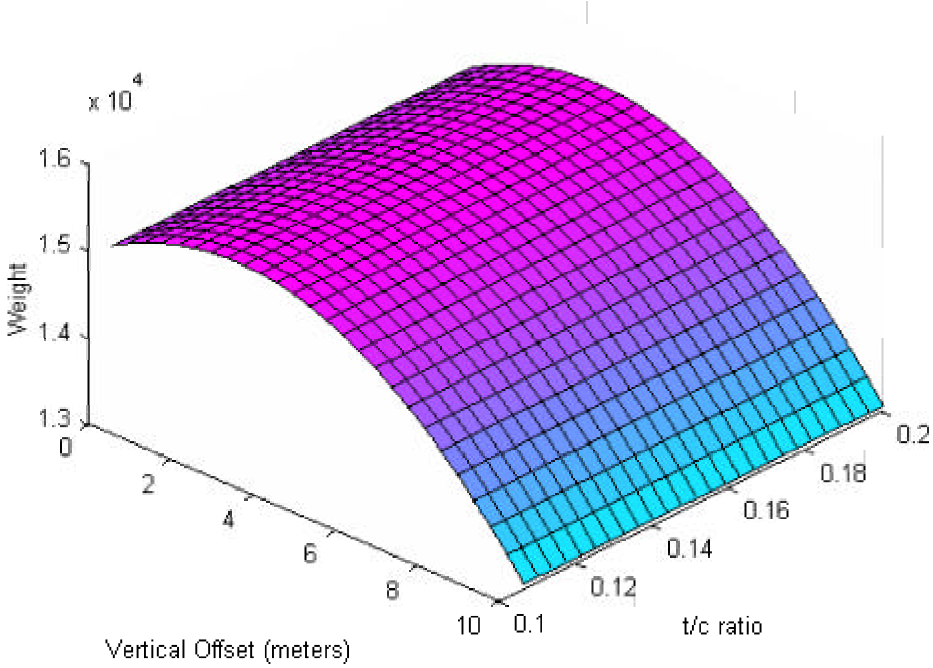

Figure 4.18 Response Surface of Vertical Offset vs. t/c (View 2)

Parameter	**1$^{\text{st}}$ Optimal**	**2$^{\text{nd}}$ Optimal**	**3$^{\text{rd}}$ Optimal**
Front Wing Sweep Angle (Λ_{ib})	34.89 °	30.00 °	34.33 °
Outboard Wing Sweep Angle (Λ_{ia})	60.00 °	-22.36 °	60.00 °
Aft Wing Sweep Angle (Λ_{ob})	20.40 °	19.52 °	28.01 °
Joint Location ($S_{ib}/[S_{ib}+S_{ob}]$)	0.594	0.716	0.581
Vertical Offset (z_{fa})	0.0 m	10.0 m	0.0 m
Thickness to Chord Ratio (t/c)	20%	10.6%	10.6%
Response Surface Half Wing Weight	-21006.64 kg	-9490.09 kg	-9353.99 kg
Observed Analysis Half Wing Weight	4011.69 kg	2913.16 kg	4363.23 kg

Table 4.1 Values for Optimal Configuration

upon the starting position of the optimization. Every configuration variable was set to its lower and upper bound in every possible combination as a starting point for the numerical search to find all possible minimal weights. The optimal configurations and their corresponding parameters are listed in Table 4.1.

The possible response surface optimal solutions have negative weights because the response surface fits the data poorly in these regions. The regions around the optimal configurations are not as well represented by the response surface as a point a the center of the design space. The primary goal of this study was to discover trends, not to find the exact optimal joined-wing configuration. The three possible solutions show three regions that should be explored in more detail.

Since the response surface has a level of error, the three optimal points were re-analyzed, using the single configuration optimization process. This method was used to find what the observed weights were for the optimal response surface weights. The smallest response surface weight came from the 1^{st} optimal point. However, the smallest observed weight came from the 2^{nd} optimal point. This confirms that the optimal points found in the response surface are optimal regions, not actual optimal points. A response surface refinement at each of these regions is required to truly determine the actual lightest-weight joined-wing sensor-craft configuration. For discussion purposes, the smallest observed configuration (2^{nd} optimal point) and the smallest fitted configuration (1^{st} optimal point) were used for comparison analysis.

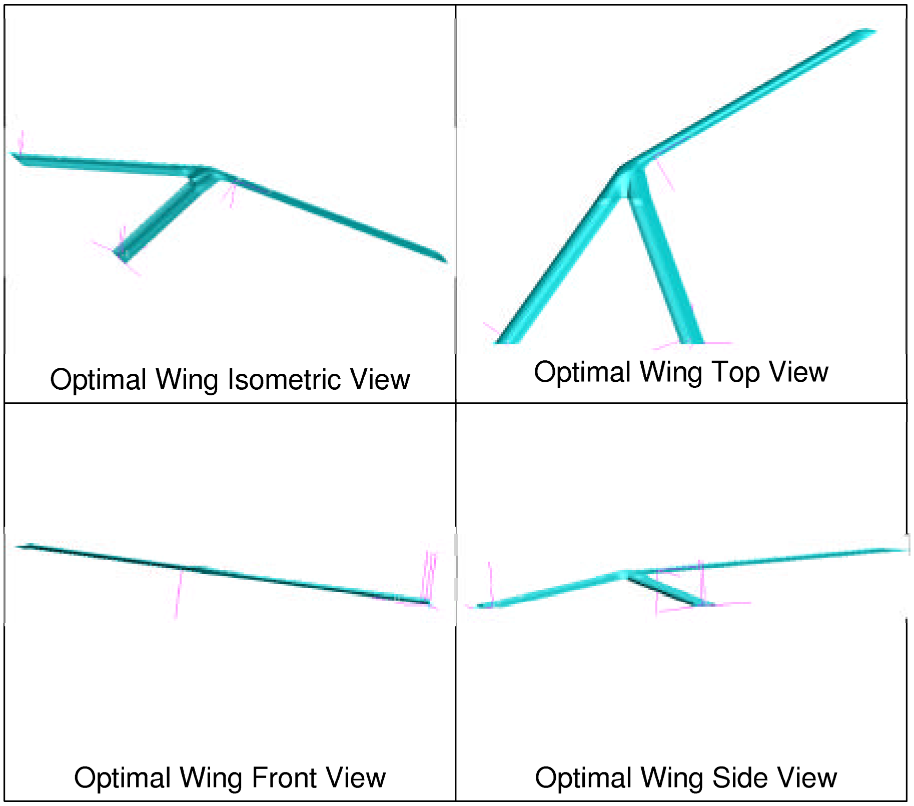

Figure 4.19 Various Views of the First Optimal Point (Smallest Fitted Weight)

These two configurations had the most significantly different design parameters which pointed out important key differences in results.

Figure 4.19 and Figure 4.20 show the two optimal points of interest in multiple views. The 1st optimal point's most significant parameters were the far backward swept outboard wing, no vertical offset, and a maximum airfoil thickness to chord ratio. The 2nd optimal point's most significantly different parameters were the forward swept outboard wing, a maximum vertical offset, and a minimum airfoil thickness.

4.3.2 Buckling Comparison. When a joined-wing has a vertical offset, the bending loads are alleviated by the front or aft wing behaving as a strut. When under a maneuver or gust loading, the aft wing acts as the support strut, while under

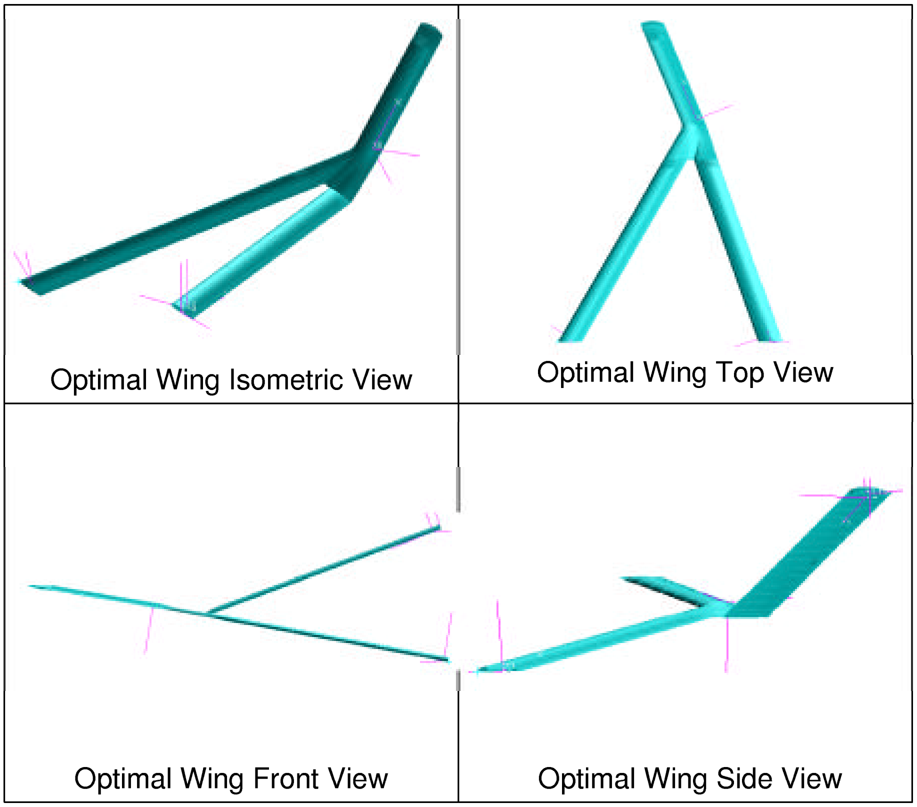

Figure 4.20 Various Views of the Second Optimal Point (Smallest Observed Weight)

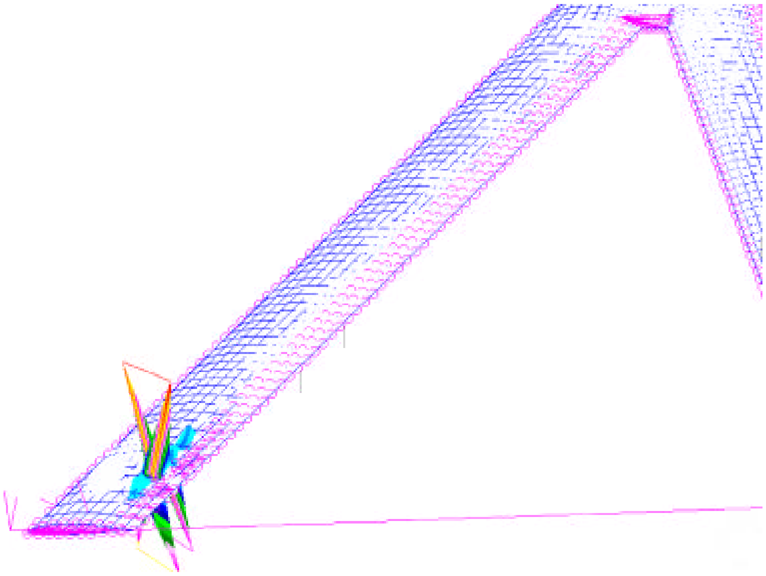

Figure 4.21 First Optimal Point Buckling Mode Shown Occurring on Front Wing Root Skin Panel

a impact loading, the front wing behaves as the support strut. These support struts behave as a resistor susceptible to global buckling behavior. However, when there is no vertical offset, the bending load is not alleviated and the wing is allowed to deflect more naturally. Under this condition, the skin panels become the buckling critical part of the wing and the buckling occurs locally instead of globally.

In this model, vertical posts that connect the top and bottom skins were added to create significant resistance to local buckling. Despite this, local buckling still occurred in the analysis. As shown in Figures 4.21 and 4.22, local buckling modes occurred on various skin panels of the 1^{st} optimal configuration. Figure 4.21 shows a sample buckling mode occurring globally on the aft wing of the 2^{nd} optimal configuration. The 2^{nd} optimal configuration still displayed local panel buckling modes similar to Figures 4.21 and 4.22, but the global buckling mode was present and drove the material sizing differently.

The two optimal points of interest were analyzed at their initial uniform thickness. Buckling modes were found at the beginning of the optimization when the

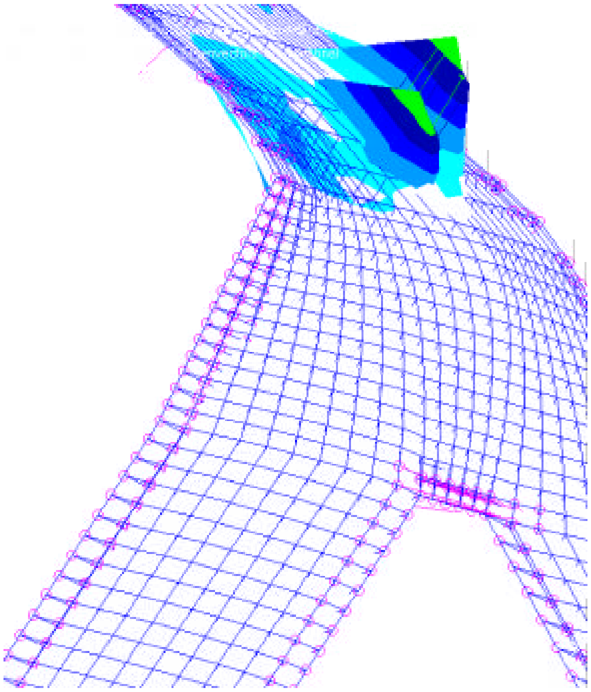

Figure 4.22 First Optimal Point Buckling Mode Shown Occurring on the Bottom of the Joint Wing Skin Panel

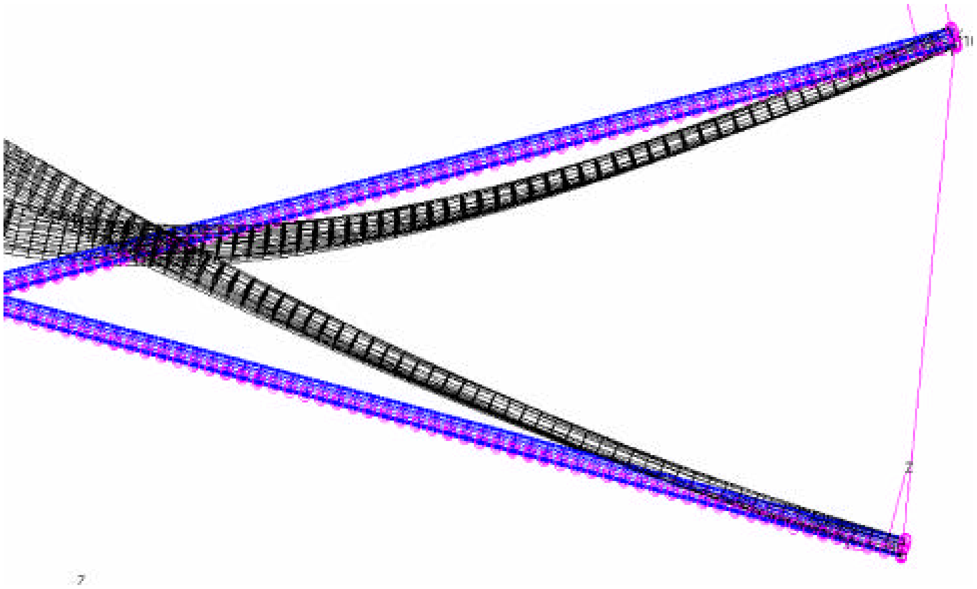

Figure 4.23 Second Optimal Point Buckling Mode Shown Across the Aft Wing (Front View)

Load Case	**1^{st} Optimal Critical Eigenvalue**	**2^{nd} Optimal Critical Eigenvalue**
2.5G Maneuver (Mission Start)	0.5429 (local)	0.4359 (local)
2.5G Maneuver (Mission End)	0.4353 (local)	1.1015 (global)
Turbulent Gust	0.4368 (local)	2.9564 (global)
Taxi Impact	0.4919 (local)	1.9618 (global)

Table 4.2 Buckling Eigenvalues of the First and Second Optimal Configurations

wing was not yet resized. Table 4.2 shows the buckling modes at each load case. The initial buckling eigenvalues, for the 1^{st} optimal configuration, were all local modes. All of these modes violated the buckling load limit of 1.5. The 2^{nd} optimal configuration showed two buckling safe load cases and two violated load cases. Only one critical load case proved to be significantly violated. The vertical offset creates global buckling situations, rather than local panel buckling, which avoids small buckling eigenvalues.

4.3.3 Non-linear Comparison. The optimal configurations were analyzed similarly to the baseline configuration (Section 4.1) to determine if a lighter weight aircraft would exhibit softening rather than stiffening. In Figure 4.24, the wing exhibits linear deflections up to a 1.0G load. The wing tip deflected more readily as the load factor increased from 1.0G to a full turbulent gust load case. After the turbulent gust case, the wing resisted non-linear deflections through extensive stiffening. This is similar to the initial non-linear comparative analysis (Section 4.1).

The lighter aircraft has less material and is less stiff overall and more susceptible to non-linear effects. The non-linear comparative analysis (Section 4.1) was conducted on a heavier aircraft structure which was not as susceptible to non-linear deflections.

The aerodynamic loads were updated and re-trimmed at 1.0G cruise, 100% of the turbulent gust, and at 150% of the turbulent gust. These loads were each applied

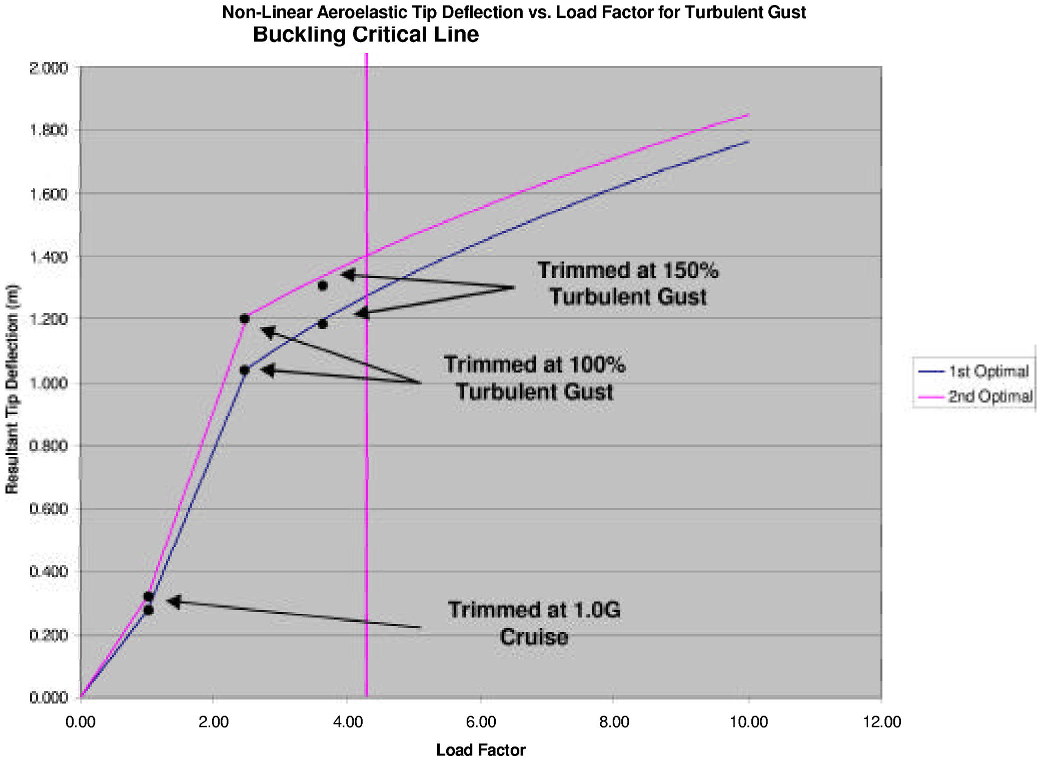

Figure 4.24 Non-Linear Aeroelastic Tip Deflection vs. Load Factor for Turbulent Load Case with Follower Forces

to a separate NASTRAN non-linear analysis. Each non-linear analysis provides tip deflection history between the three updated load points. The loads were then applied as follower forces where the direction of the lift would stay perpendicular to the wing surface. By updating the aerodynamic loads through the load history, the load distribution was properly updated for the current load factor wing deflections. This factored in possible non-linear aeroelasticity effects where the aerodynamic loads do not vary linearly with wing deformations.

4.3.4 Aerodynamic Force Distribution. Figures 4.25, 4.26, and 4.27 show the spanwise force distribution for the various joined-wing sections of the joined-wing configuration with the lowest optimal weight observed (2^{nd} optimal configuration). The spanwise distance was measured perpendicularly from the fuselage. The spanwise distribution was not measured with the longitudinal axes of the wings. The force distribution of the front wing displayed a classical elliptical profile. The joint and outboard wing sections showed a large distribution of forces in the joint section while the outboard wing section showed much less, because of the larger chord at the joint. The spikes in the aerodynamic load distribution graphs represented splining locations. The sudden increase in load was due from more wing material or fuel weight present at the specified span distance. A limited number of splines were used in the FlightLoads model (Section 3.11) and produced non-smooth curves. If a high number of splines were used, the distribution curve would be smooth and closer to a real-life aerodynamic lift distribution.

The sudden spike at the of joint-wing section's span is due to the transition from the joint wing, which contains 11 chordwise spline locations, to the outboard wing, which contains 3 chordwise spline locations. The aft wing section showed a negative elliptical shape. The aft-wing twist mechanism reversed the load on the aft wing to balance the loads for pitch and trim. Figure 4.28 shows the turbulent

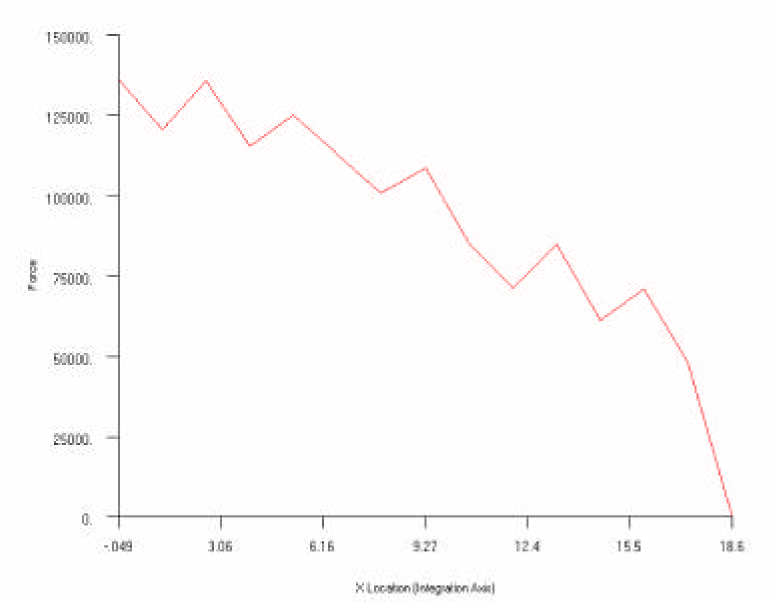

Figure 4.25 Aerodynamic Force Distribution of Front Wing Section Under 2.5G Maneuver Flight Condition for 2nd Optimal Configuration

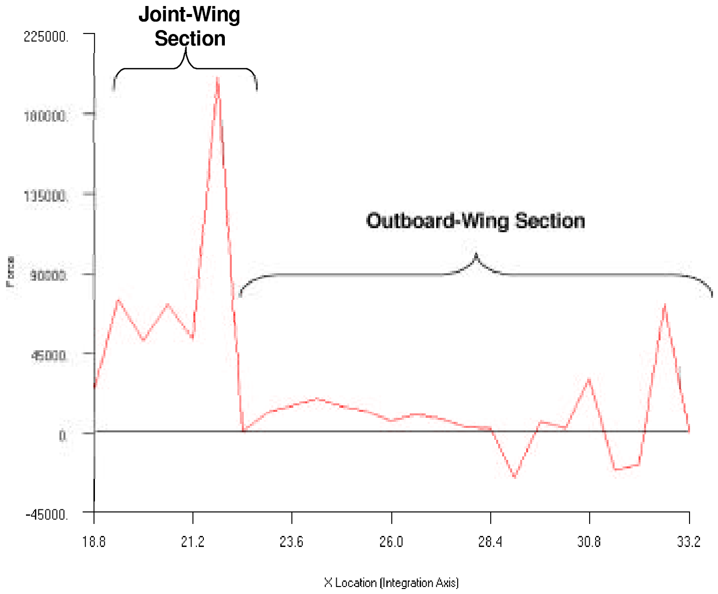

Figure 4.26 Aerodynamic Force Distribution of a Joint/Forward-Swept-Outboard Wing Section Under 2.5G Maneuver Flight Condition for 2nd Optimal Configuration

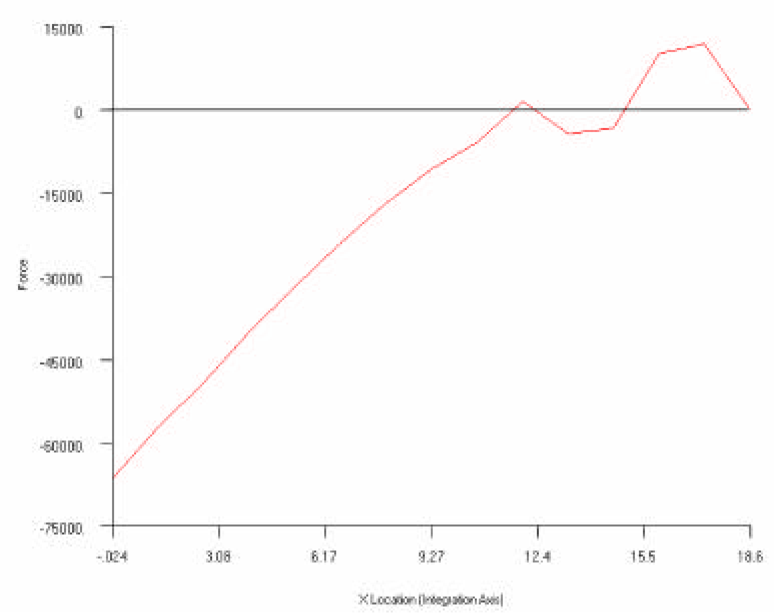

Figure 4.27 Aerodynamic Force Distribution of Aft Wing Section Under 2.5G Maneuver Flight Condition for 2nd Optimal Configuration

gust loads on the aft-wing. The negative elliptical lift profile on the aft wing shifts up, relative to the maneuver loads, since the aft-wing twist was set constant for the gust case and the angle of attack increased for the entire aircraft.

The outboard-wing on the 1^{st} optimal point (lightest fitted weight) showed a low net force distribution similar to the 2^{nd} optimal point (lightest observed weight). The joint/outboard-wing force distribution is shown in Figure 4.29.

Both of the forward swept (2^{nd} optimal point) and backward swept (1^{st} optimal point) outboard wing sections displayed small and flat force distributions. A zero outboard wing sweep model was analyzed for comparison purposes. As shown in Figure 4.30, the force distribution of a configuration with no outboard-wing sweep showed a much smaller drop from the joint section to the outboard section. In addition, the net force on the outboard wing was much higher than the distributions displayed from an extremely forward swept wing (Figure 4.26) and an extremely backward swept wing (Figure 4.29). The calculated average force per spanwise

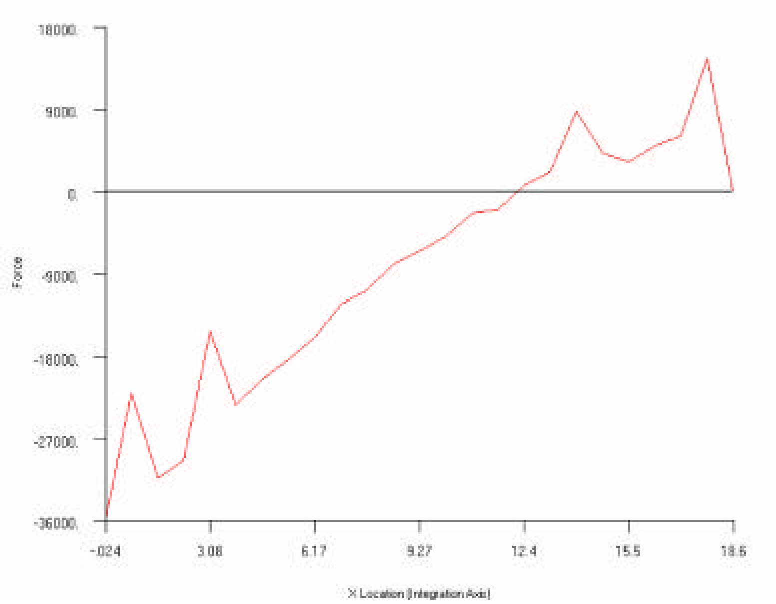

Figure 4.28 Aerodynamic Force Distribution of Aft Wing Section Under Turbulent Gust Flight Condition for 2nd Optimal Configuration

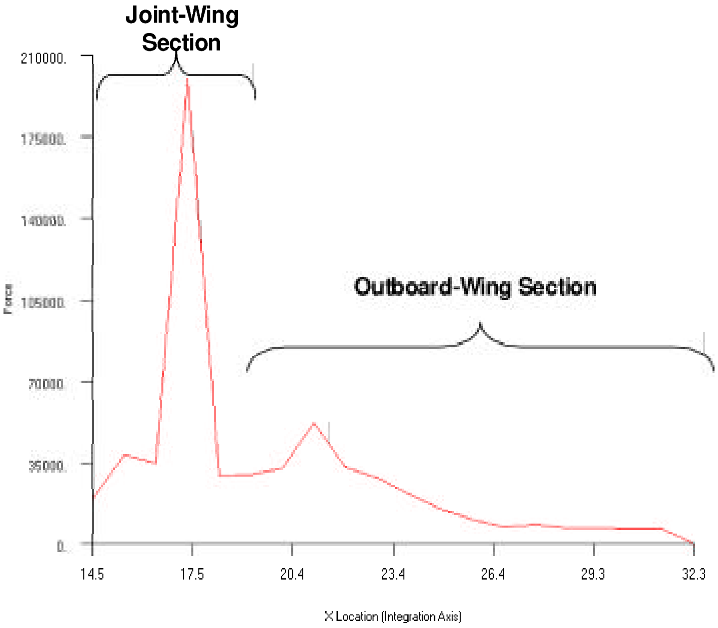

Figure 4.29 Aerodynamic Force Distribution of a Joint/Aft-Swept-Outboard Wing Section Under 2.5G Maneuver Flight Condition for 1st Optimal Configuration

Configuration	**Wing Sweep Angle**	**Average Force**
1st Optimal	60.0° Aft	24,329.8 N/m
1st Optimal (Adjusted)	0.0°	17,642.3 N/m
2nd Optimal	22.36° Forward	22,136.5 N/m

Table 4.3 Average Force Distribution per Spanwise Length for Varying Outboard Wing Sweep Angles

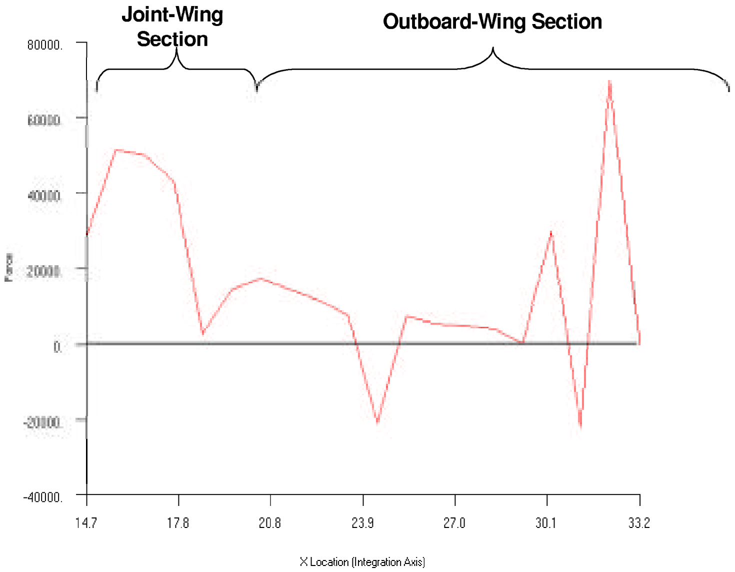

Figure 4.30 Aerodynamic Force Distribution of a Non-Swept Joint/Outboard Wing Section Under 2.5G Maneuver Flight Condition

distance is shown in Table X. This provides an explanation as to why the outboard wing sweep was either far forward or far aft.

A forward swept wing moved the center of pressure forward for the entire vehicle. It moved the overall center of pressure forward and closer to the center of gravity. This resulted in a more equal distribution of forces acting on the front wing and aft wing. If the center of gravity and center of pressure were at the same position, the moment generated by the difference in net forces acting on the aft and front wing is small. In contrast, a swept backward outboard wing would move the total vehicle's center of pressure backward. This was an unfavorable condition, except that the outboard wing will twist downward creating a negative angle of attack for the outboard wing. This reduces the load acting on the outboard wing.

The orientation of the composite plies can also make a forward swept wing twist in a favorable direction. If the 45° composite ply is very stiff, the wing will still deflect upward, but it will twist downward keeping the forward swept wing's angle of attack low. As shown in Subsection 4.3.5, the majority of the material was placed in the 45.0°/-45.0°, composite ply direction. Aeroelastic tailoring of a forward swept outboard wing was apparent in the structural optimization. The thicker 45.0°/-45.0° plies provided favorable bending-twist coupling. Again, the up-wing bending gave twist to alleviate outboard loads and reduce the root-wing bending moment of the front wing.

4.3.5 Material Placement Comparison. The plies shown in Figures 4.31, 4.32, and 4.33 show that the thickness distributions are larger for the 45.0°/-45.0° plies than for the 0.0° and 90.0° plies. This is consistent across all wing sections. The aft chordwise distribution includes the skin elements near the aft spar. The center chordwise distribution includes the skin elements in the middle of the panel. The forward chordwise distribution includes the skin elements near the front spar. The normalized span distance is represented as 0.0 being at the wing root and 1.0 being at the wing joint. The normalized ply thickness is represented as a multiplier of the minimum gauge thickness, or rather, the number of plies. The minimum gauge was 0.000284m for each ply.

The 45.0°/-45.0° plies primarily resist twisting rather than pure tension or compression. It was concluded that since these plies are much larger than the other plies, the torsional moment acting on the wing is significant compared to compression or tension resulting from the bending moment.

As shown in Figure 4.32, the middle thickness panel (second chordwise distribution) shows the largest thicknesses. This is the distribution for the 1^{st} optimal

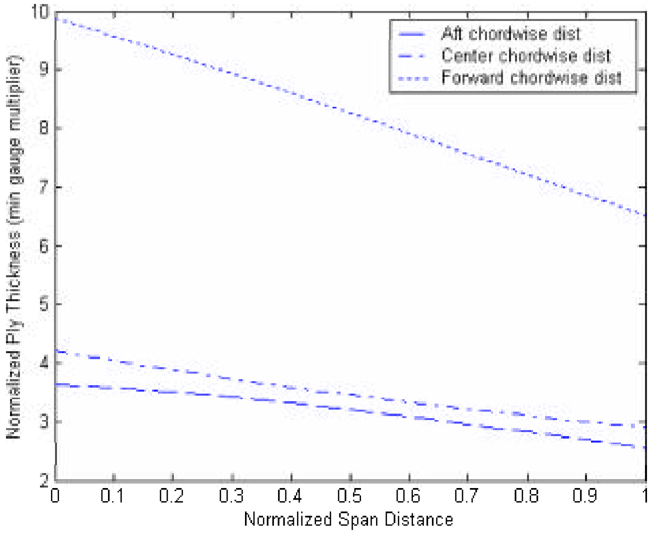

Figure 4.31 Thickness Distribution of 0.0 Degree Plies on the Front-Wing Top Skins for 1st Optimal Configuration

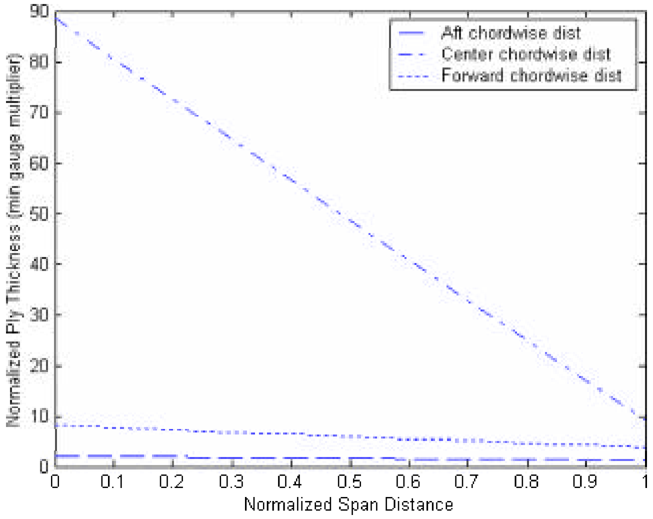

Figure 4.32 Thickness Distribution of -45.0/45.0 Degree Plies on the Front-Wing Top Skins for 1st Optimal Configuration

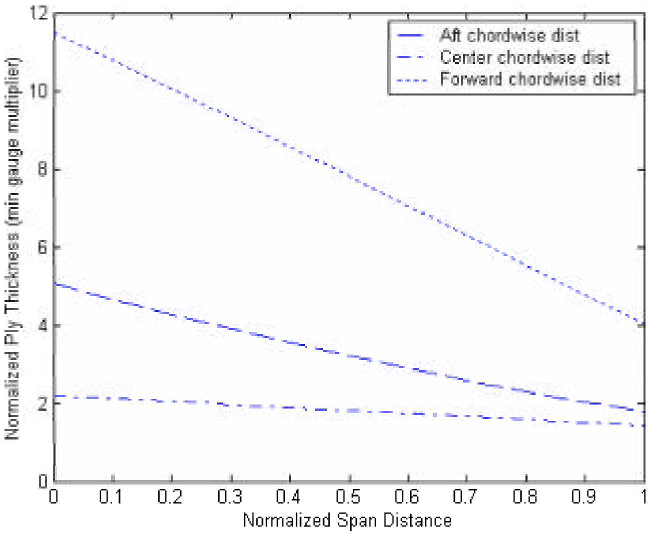

Figure 4.33 Thickness Distribution of 90.0 Degree Plies on the Front-Wing Top Skins for 1st Optimal Configuration

point (smallest fitted weight). The 2^{nd} optimal point (smallest observed weight) displays a slightly different profile (Figure 4.34).

The joint wing showed flat distribution shapes over its span. As shown above, the force distribution plots in the joint sections are usually large with peaks varying across the joint-wing span distance. This creates a more uniform distribution plot overall. Figures 4.35, 4.36, 4.37, and 4.38 show the joint-wing thickness distributions for various parts of the wing. The 45.0°/-45.0° plies are shown since they display the largest and most varying thickness distributions.

The outboard-wing thickness distribution on the top skins were found to be aft rather than a centered or forward distribution (Figure 4.39). This implies that the majority of the chordwise loads on the aft wing acted on the aft portion of the forward swept wing. A complete set of figures showing thickness distributions across all wing regions for the lowest observed weight joined-wing configuration is shown in Appendix C.

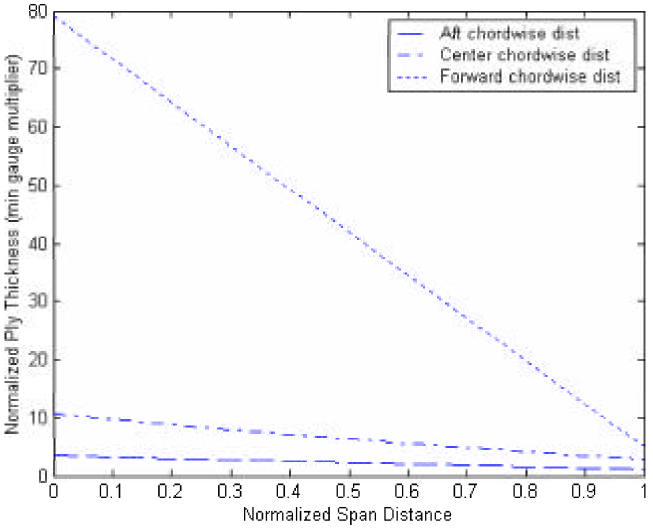

Figure 4.34 Thickness Distribution of -45.0/45.0 Degree Plies on the Front-Wing Top Skins for 2nd Optimal Configuration

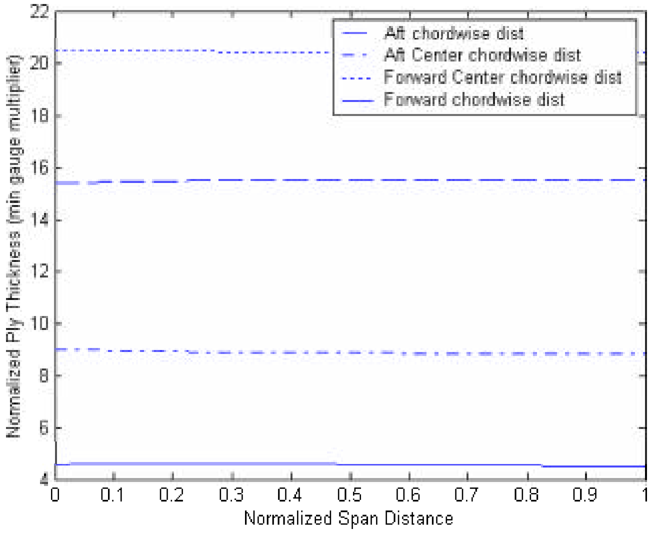

Figure 4.35 Thickness Distribution of -45.0/45.0 Degree Plies on the Joint-Wing Top Skins for 1st Optimal Configuration

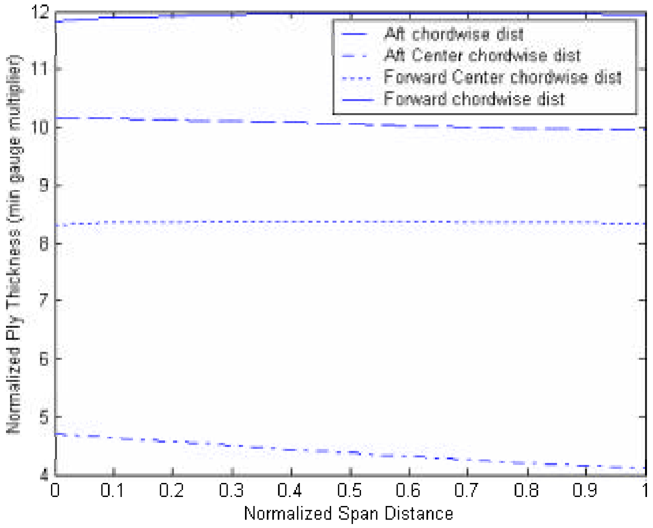

Figure 4.36 Thickness Distribution of -45.0/45.0 Degree Plies on the Joint-Wing Bottom Skins for 1st Optimal Configuration

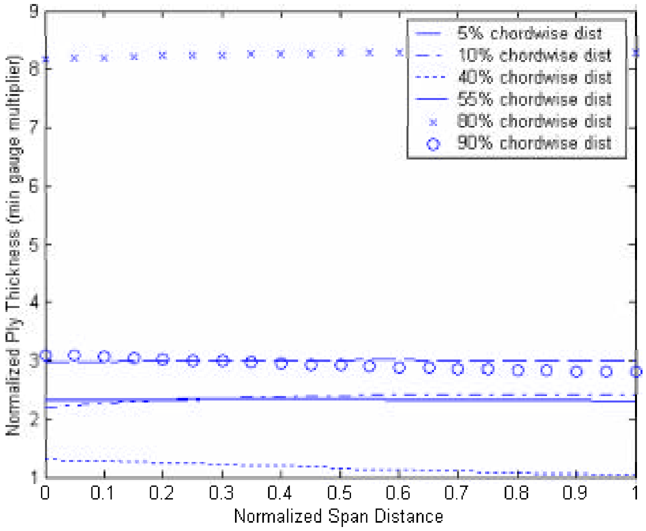

Figure 4.37 Thickness Distribution of -45.0/45.0 Degree Plies on the Joint-Wing Spars for 1st Optimal Configuration

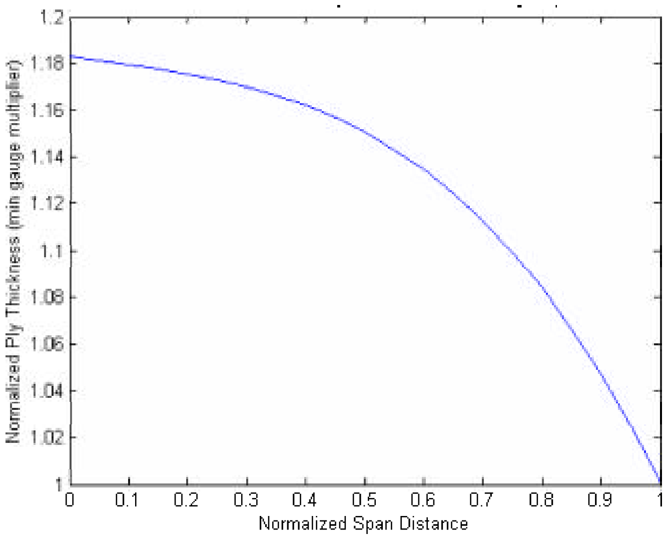

Figure 4.38 Thickness Distribution of -45.0/45.0 Degree Plies on the Joint-Wing Ribs for 1st Optimal Configuration

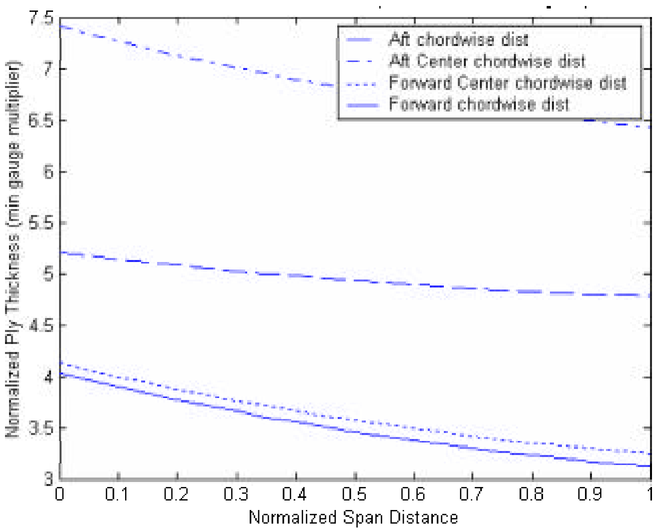

Figure 4.39 Thickness Distribution of -45.0/45.0 Degree Plies on the Outboard-Wing Top Skins for 2nd Optimal Configuration

V. Conclusions and Recommendations

5.1 Configuration Optimization

This study presented general trends for the configuration design of a joined-wing sensor-craft concept. The response surfaces displayed several pairs of design variables that have very little interaction, but more importantly it displayed which variable pairs create a minimum weight design where a configuration variable must be at its maximum or minimum.

The optimal configuration points, as determined by the response surfaces, showed the trade-off of airfoil thickness to chord ratio in relation to vertical offset. Since the optimal weight aircraft was found to either have a high vertical offset and a low t/c or a low vertical offset and a high t/c, the true optimal design space could be either one. Designers should explore both types of optimal solutions for their mission needs while still including buckling as a key constraint. Buckling and non-linear deflections are essential in designing either type of joined-wing concepts.

The response surface also showed the trade off from a forward sweeping outboard wing to a backward sweeping outboard wing. The placement of -45.0 °/45.0 ° plies produced a wing that would bend up but twist downward.

The trends showed that the joint location should be in the half span to three-quarters span distance. The joint location would not provide a lighter weight solution at a low joint location or at a high joint location. This created a design space region where the front and aft wings were long enough to support the other, but not too long to create too much surface area and material.

The front and aft wings were found not to reside at highly swept angles. This allowed the wings a moderate angle of separation between the other and provided one to act as a support strut for given load case. A large angle between the two wings would create a front and aft wing with large sweep angles and a large surface area with too much material.

For a wing that was designed for strain and buckling, the wing deflected in a stiffening manner for a constant set of loads. Conversely, the aerodynamic loads associated with a non-linearly deflected wing do not stay constant, but rather increase in a non-linear manner. The interaction between the updating aerodynamic loads and updating the structural deflections is non-linear.

5.2 Model/Process Recommendations

The response surfaces determined in this study only provided a good understanding for general design trends. The optimal regions found from the response surface are ill-defined and should be locally sampled. This would create a better defined optimal region in which to determine a true optimal configuration. An iterative process between finding new optimal regions and creating better defined response surfaces would be beneficial and more conclusive.

The iterative process between structural deformations and the recalculating of aerodynamic loads creates a coupling effect that can be poorly estimated. This effect can not be truly seen unless the structure loads and deflections are iterated between a non-linear aerodynamic model and non-linear structural model until the wing deflections and aerodynamic loads do not change between iterations. This study used three structural updates and three aerodynamic updates. More updates would have been beneficial for accuracy.

5.3 Recommendations for Future Work

A refinement of the determined optimal regions would provide finer accuracy into a local joined-wing configuration design. The process used in this study could be used again, but around a smaller range that surrounds the optimal regions. This would redefine a better defined local response surface. Additionally, an inspection into the FlightLoads model or a computational fluids analysis around the outboard wing would be beneficial to compare before continuing to use the same FlightLoads to model. The sectional center of pressure acting on the wing should be estimated properly and match typical solutions for a far forward swept wing.

Structural configurations of the joint section, that combines front, aft, and outboard wings together, could provide insight into the transfer of loads through the joint region. A more lightweight rib and spar concept could be devised around this wing area.

The front and aft spar could be oriented at an angle so that the joined-wing material placement described by Wolkovich could be done more directly. If a spar was exactly perpendicular to a canted bending plane, material of the spar would be placed such that it resists the bending directly instead of at an angle.

An analysis on a skin panel could better define local buckling modes and eigenvalues. The number of nodes and elements used in this model were not significant enough, in a skin panel region, to correctly model local buckling. A model which combines a globally represented joined-wing and a local skin panel could prove different skin sizing and buckling alleviation.

Appendix A. Conversion of AVTIE Fuel Loads for FlightLoads Application

To complete a NASTRAN optimization with both FlightLoads and buckling analyses, the fuel weight was applied as a distributed force to the body instead of as a point mass. Fuel weight information was provided through a single AVTIE run for a particular wing weight. The full fuel weight was taken from the beginning of the ingress mission leg. The required fuel weight varied significantly through a change in wing weight. The model's wing weight changed the overall fuel weight requirement and thus provided new appropriately scaled fuel forces.

The fuel requirements were calculated using the Breguet range equation (Equation 1.1). For a specific range, time, lift over drag, velocity and specific fuel consumption, the total change in weight ratio was calculated for each mission leg. The total weight requirement was determined by multiplying all three mission legs (ingress, loiter, and egress) weight ratios.

$$\frac{W_{takeoff}}{W_{landing}} = \frac{W_{total}}{W_{structure}} = \left(\frac{W_{0-00}}{W_{1-00}}\right)\left(\frac{W_{1-00}}{W_{2-00}}\right)\left(\frac{W_{2-00}}{W_{2-98}}\right) \tag{A.1}$$

The fuel was assumed to be completely exhausted by landing. This implies that the landing weight will equal the total structural weight. The fuel weight is then the difference between the total weight (fuel and structure) and the total structural weight.

$$W_{fuel} = W_{total} - W_{structure} \tag{A.2}$$

This is convenient, since the total structural weight did not vary except for the weight of the wing.

$$W_{structure}\left(x\right) = W_{wing}\left(x\right) + W_{fuslage} + W_{tail} + W_{payload} \tag{A.3}$$

Where the weight of the wing will vary with respect to the vector of optimization design variables x_i.

The overall analysis was conducted so the fuel weight requirements were constant for each phase. This was because fuel weight forces could not change with internal design variables within a single optimization. This means that the total structural weight was constant for each phase. The total structural weight was updated before each phase.

The structural weight was determined from an initial wing weight guess. The initial wing weight guess was determined from test optimization runs. The total AVTIE aluminum model structural weight and fuel weight were given through the AVTIE interface. The total weight requirements for both the composite and the aluminum baseline mode were calculated utilizing the total change in weight ratio using Equation A.1. Once the total weight was determined for each model, the fuel weight was then calculated through Equation A.2. The initial fuel weight scalar at takeoff can now be calculated as:

$$B_{0-00} = \frac{W_{fuel-composite}}{W_{fuel-AVTIE}} \tag{A.4}$$

This value was applied as a load scalar for the first subcase in NASTRAN.

The subsequent fuel weights, for each load case, were also scaled similarly. The total weight at any mission point, W_{x-xx}, for the composite model is given as

$$W_{x-xx} = \frac{W_{fuel-composite} + W_{structure}}{\left(\frac{W_{0-00}}{W_{1-00}}\right)^{f_{ingress}} \left(\frac{W_{1-00}}{W_{2-00}}\right)^{f_{loiter}} \left(\frac{W_{2-00}}{W_{2-98}}\right)^{f_{egress}}} \tag{A.5}$$

where $f_{ingress}$ is the fraction complete of the ingress mission leg, f_{loiter} is the fraction complete of the loiter mission leg, and f_{egress} is the fraction complete of the egress mission leg.

The total weight at any mission point can be determined, since the weight ratios for each mission can be fractionalized for every mission leg and every mission leg fraction. For example, at mission case 1-50, the ingress fraction complete is 1.0, the loiter fraction complete is 0.5, and the egress fraction complete is 0.0. Taking the result from Equation A.4, the fuel weight for the composite model can be put in known terms

$$W_{fuel-composite} = B_{0-00} \cdot W_{fuel-AVTIE} \tag{A.6}$$

resulting in

$$W_{fuel-x-xx} = \frac{B_{0-00} \cdot W_{fuel-AVTIE} + W_{structure}}{\left(\frac{W_{0-00}}{W_{1-00}}\right)^{f_{ingress}} \left(\frac{W_{1-00}}{W_{2-00}}\right)^{f_{loiter}} \left(\frac{W_{2-00}}{W_{2-98}}\right)^{f_{egress}}} - W_{structure} \tag{A.7}$$

The actual AVTIE fuel forces must be in terms of a scalar. The structural weight is then placed in terms of the AVTIE fuel weight

$$k = \frac{W_{structure}}{W_{fuel-AVTIE}} \tag{A.8}$$

to obtain

$$W_{fuel-x-xx} = \frac{B_{0-00} \cdot W_{fuel-AVTIE} + k \cdot W_{fuel-AVTIE}}{\left(\frac{W_{0-00}}{W_{1-00}}\right)^{f_{ingress}} \left(\frac{W_{1-00}}{W_{2-00}}\right)^{f_{loiter}} \left(\frac{W_{2-00}}{W_{2-98}}\right)^{f_{egress}}} - k \cdot W_{fuel-AVTIE} \tag{A.9}$$

through substitution.

The scalar to be applied to the AVTIE fuel loads can expressed as

$$B_{x-xx} = \frac{W_{x-xx}}{W_{fuel-AVTIE}} \tag{A.10}$$

After dividing Equation A.9 by the fuel weight of AVTIE, a scalar B_{x-xx} can be calculated for any mission case and accurately applied to the AVTIE fuel weight input deck

$$B_{x-xx} = \frac{B_{0-00} + k}{\left(\frac{W_{0-00}}{W_{1-00}}\right)^{f_{ingress}} \left(\frac{W_{1-00}}{W_{2-00}}\right)^{f_{loiter}} \left(\frac{W_{2-00}}{W_{2-98}}\right)^{f_{egress}}} - k$$

Appendix B. MatLab Software Integration

MatLab code was the code used to integrate multiple NASTRAN runs and to complete the pre- and post-processing before and after each phase [9, 18]. Correct formatting of bulk data card entries is required for proper NASTRAN runs. Figure **??** shows the flow how each subroutine written in MatLab work together and within the overall master routine.

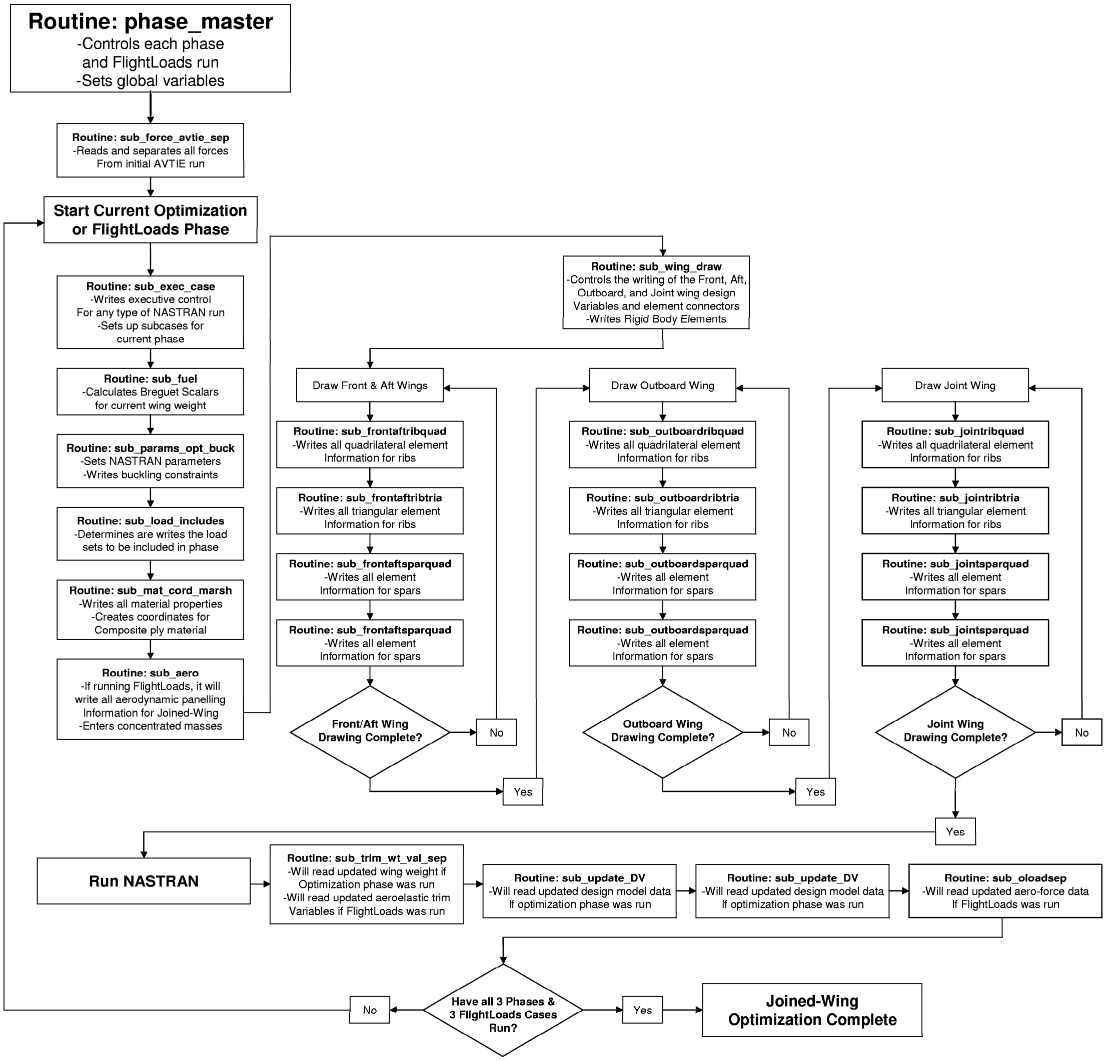

Software Flow for Single Optimization Run in MatLab

Appendix C. Thickness Distributions for Lowest Observed Configuration

This appendix includes all the thickness distributions from the lowest observed optimal configuration. The thicknesses were plotted for each ply and for each region of the joined-wing.

The aft chordwise distribution includes the skin elements near the aft spar. The center chordwise distribution includes the skin elements in the middle of the panel. The forward chordwise distribution includes the skin elements near the front spar.

The normalized span distance is represented as 0.0 being at the wing root and 1.0 being at the wing joint or tip. The normalized ply thickness is represented as a multiplier of the minimum gauge thickness, or rather, the number of plies. The minimum gauge was 0.000284m for each ply.

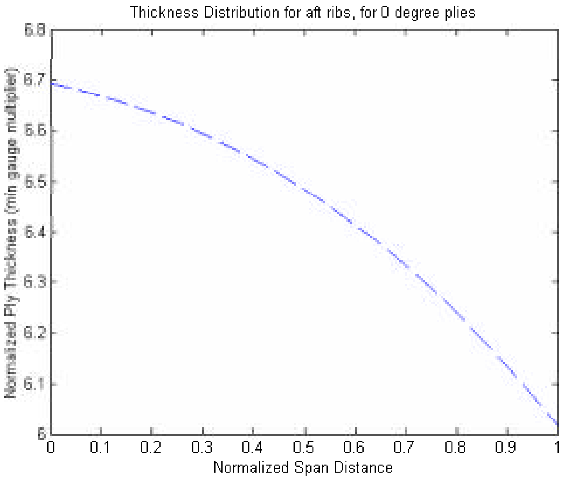

Thickness Distribution of 0.0 Degree Plies on the Aft-Wing Ribs

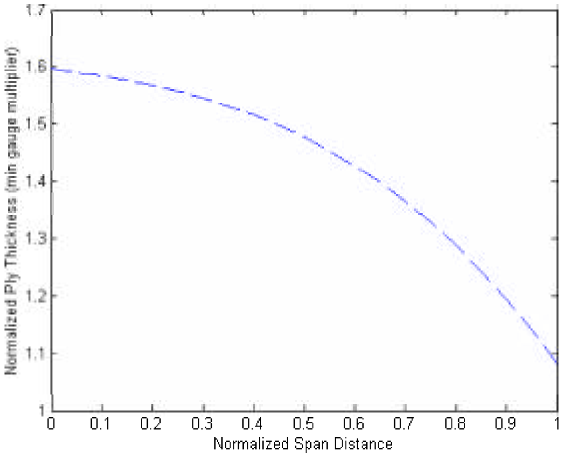

Thickness Distribution of 45.0 Degree Plies on the Aft-Wing Ribs

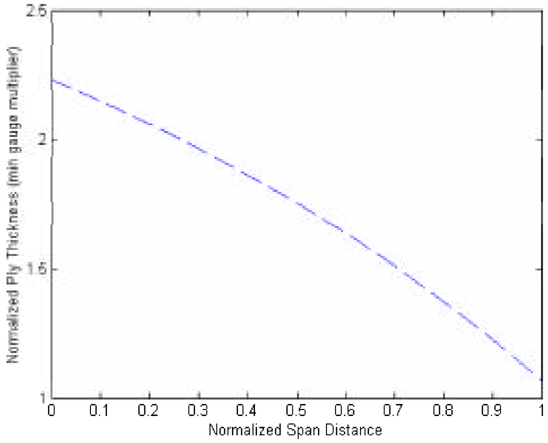

Thickness Distribution of 90.0 Degree Plies on the Aft-Wing Ribs

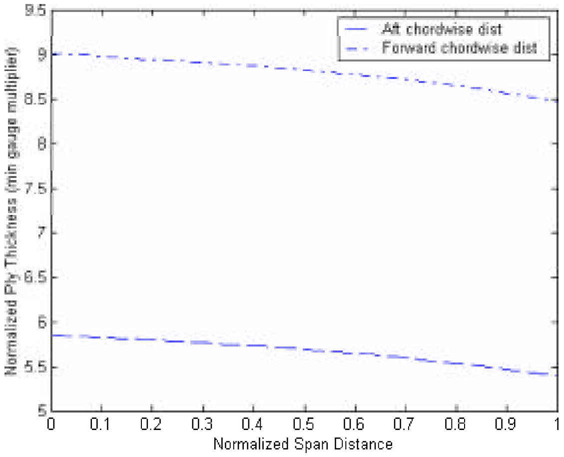

Thickness Distribution of 0.0 Degree Plies on the Aft-Wing Spars

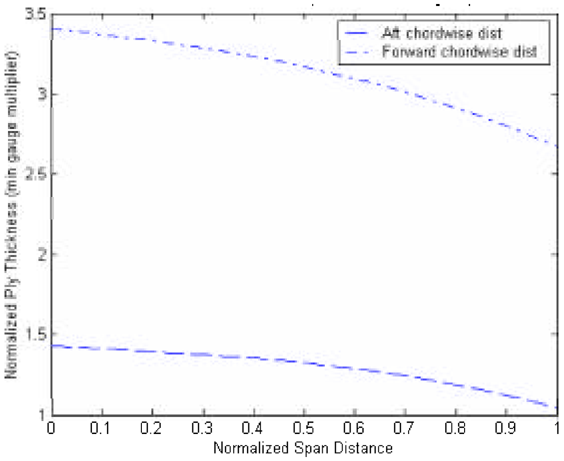

Thickness Distribution of 45.0 Degree Plies on the Aft-Wing Spars

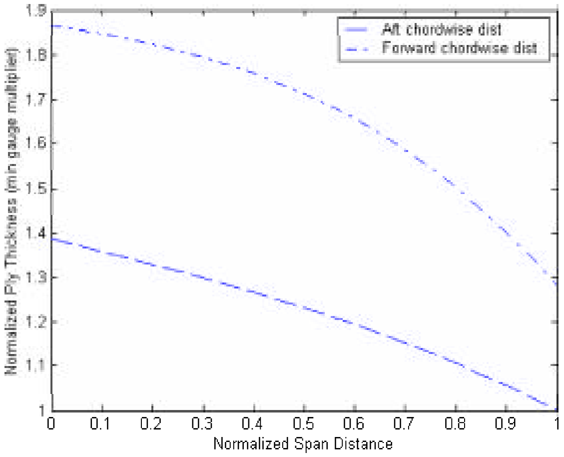

Thickness Distribution of 90.0 Degree Plies on the Aft-Wing Spars

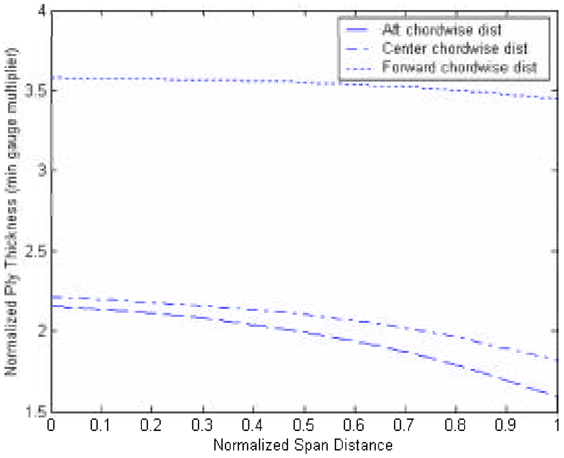

Thickness Distribution of 0.0 Degree Plies on the Aft-Wing Top Skins

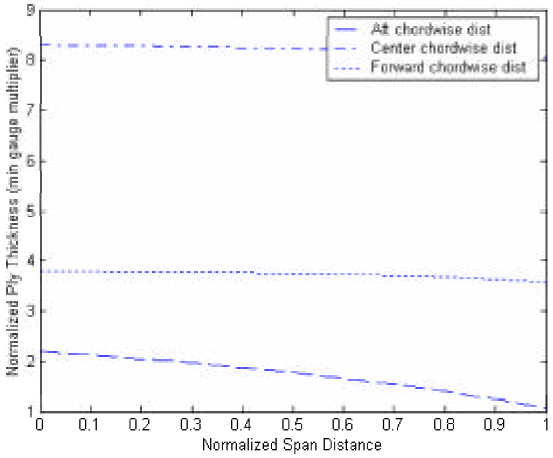

Thickness Distribution of 45.0 Degree Plies on the Aft-Wing Top Skins

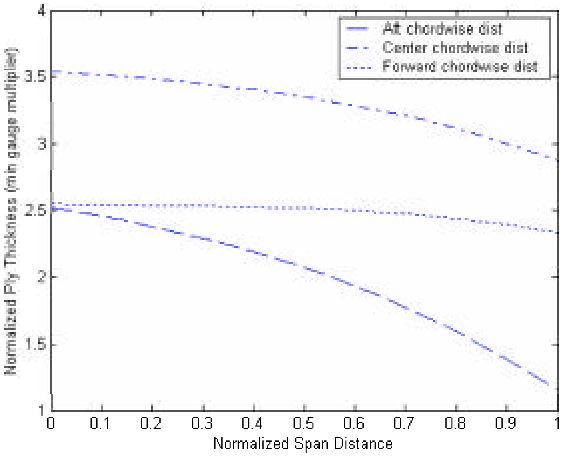

Thickness Distribution of 90.0 Degree Plies on the Aft-Wing Top Skins

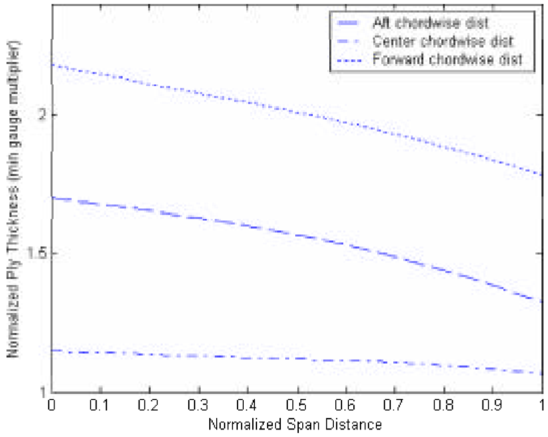

Thickness Distribution of 0.0 Degree Plies on the Aft-Wing Bottom Skins

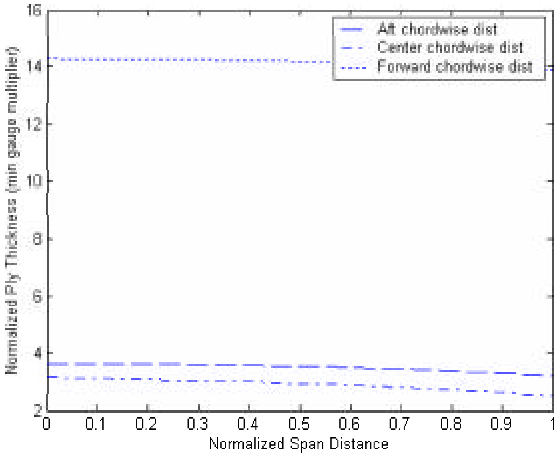

Thickness Distribution of 45.0 Degree Plies on the Aft-Wing Bottom Skins

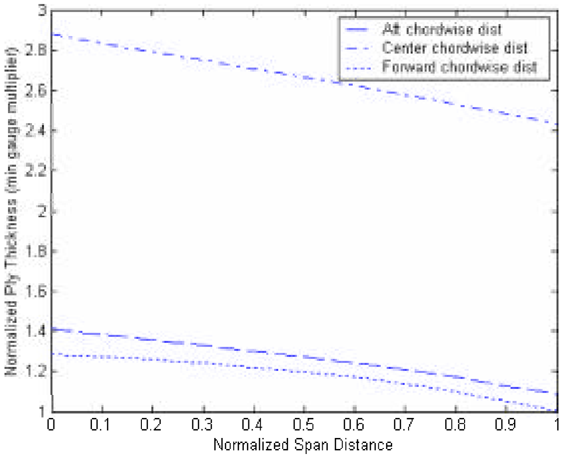

Thickness Distribution of 90.0 Degree Plies on the Aft-Wing Bottom Skins

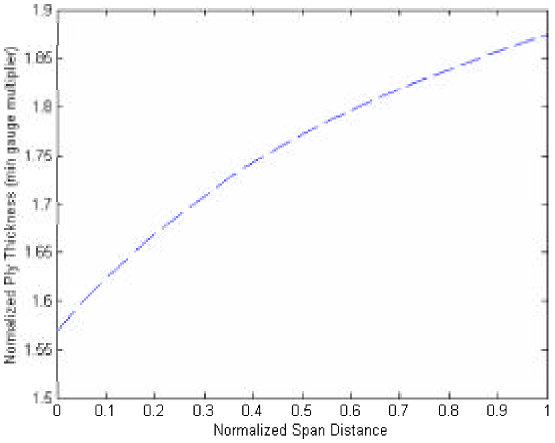

Thickness Distribution of 0.0 Degree Plies on the Front-Wing Ribs

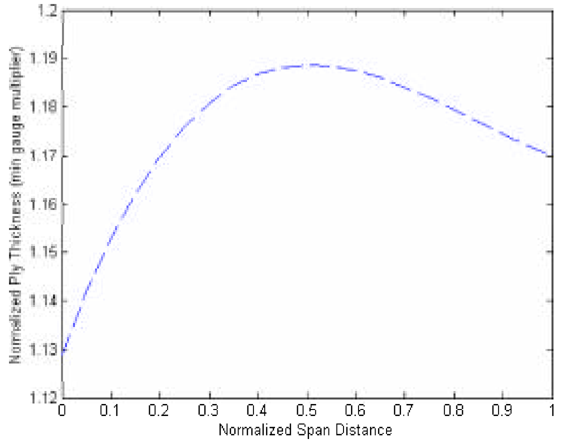

Thickness Distribution of 45.0 Degree Plies on the Front-Wing Ribs

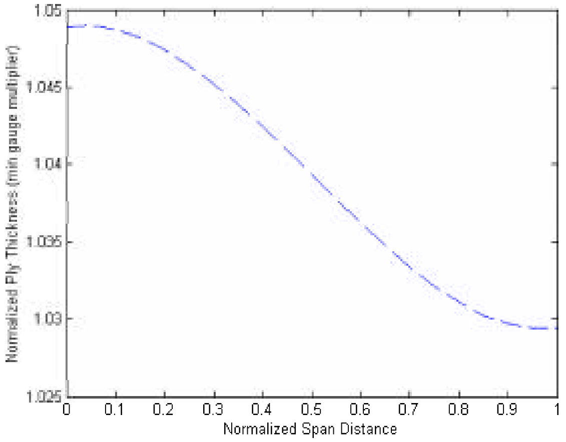

Thickness Distribution of 90.0 Degree Plies on the Front-Wing Ribs

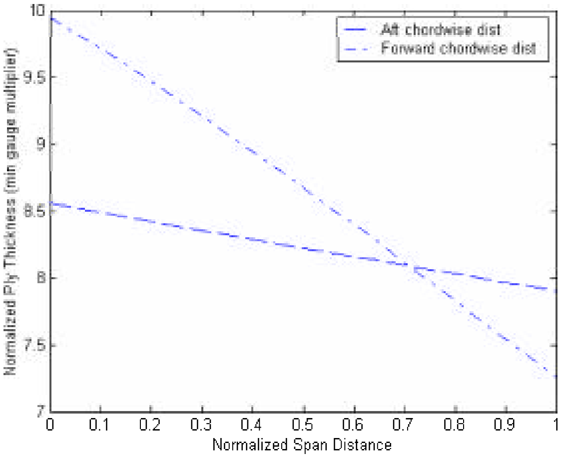

Thickness Distribution of 0.0 Degree Plies on the Front-Wing Spars

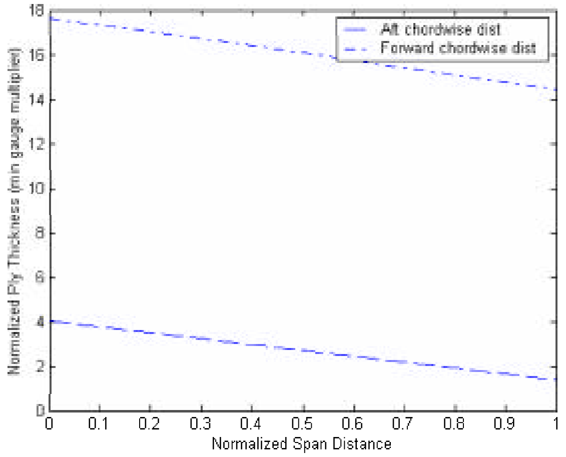

Thickness Distribution of 45.0 Degree Plies on the Front-Wing Spars

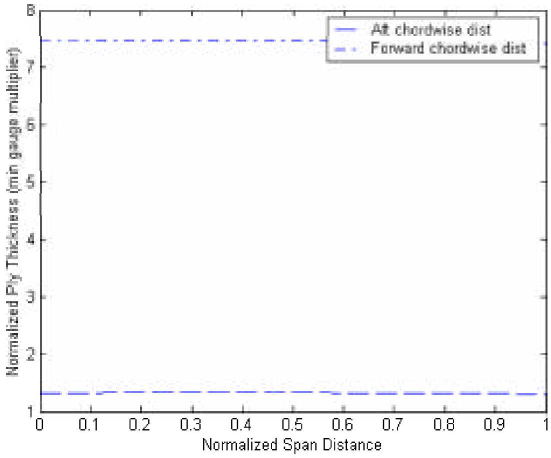

Thickness Distribution of 90.0 Degree Plies on the Front-Wing Spars

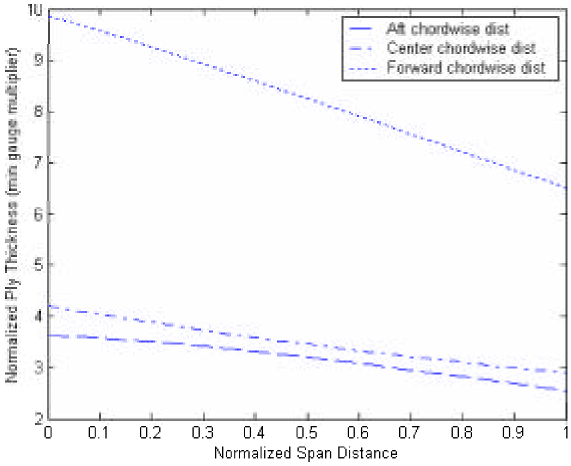

Thickness Distribution of 0.0 Degree Plies on the Front-Wing Top Skins

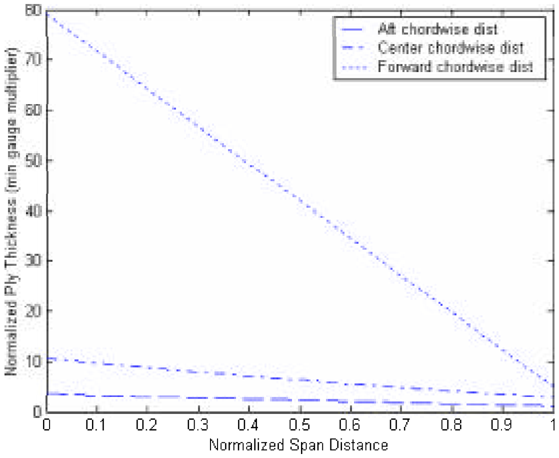

Thickness Distribution of 45.0 Degree Plies on the Front-Wing Top Skins

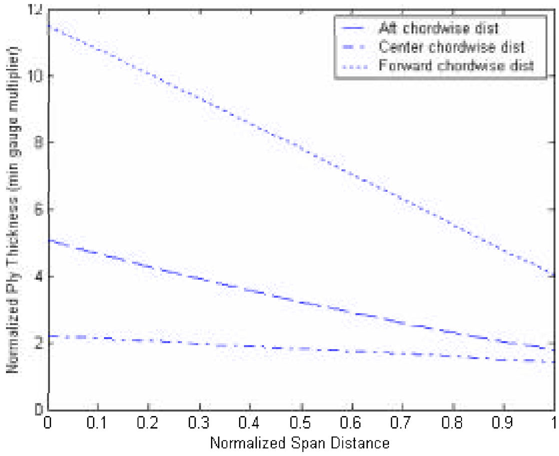

Thickness Distribution of 90.0 Degree Plies on the Front-Wing Top Skins

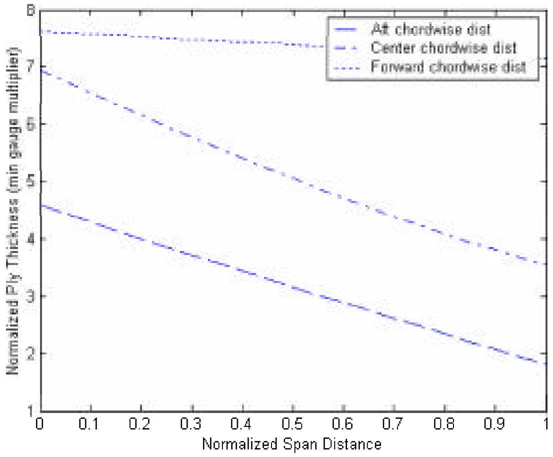

Thickness Distribution of 0.0 Degree Plies on the Front-Wing Bottom Skins

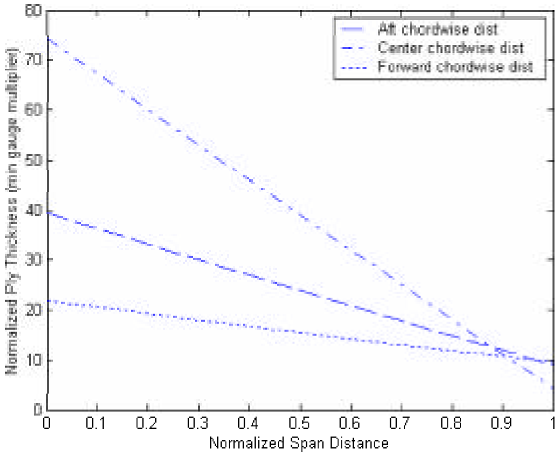

Thickness Distribution of 45.0 Degree Plies on the Front-Wing Bottom Skins

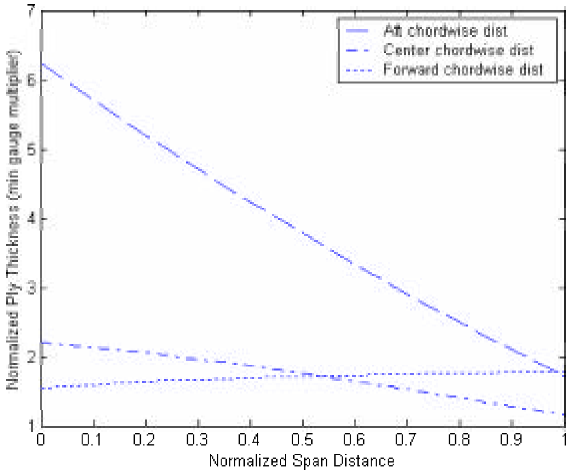

Thickness Distribution of 90.0 Degree Plies on the Front-Wing Bottom Skins

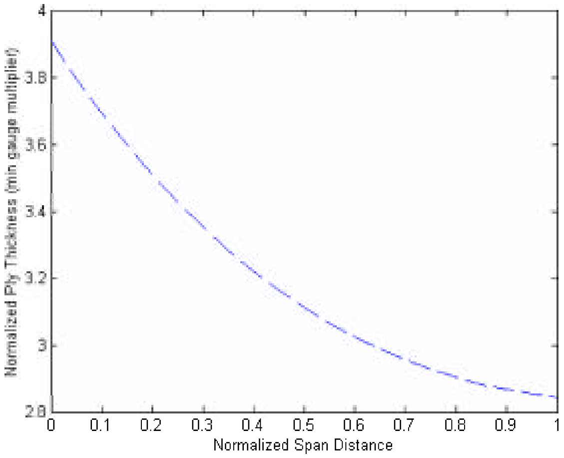

Thickness Distribution of 0.0 Degree Plies on the Outboard-Wing Ribs

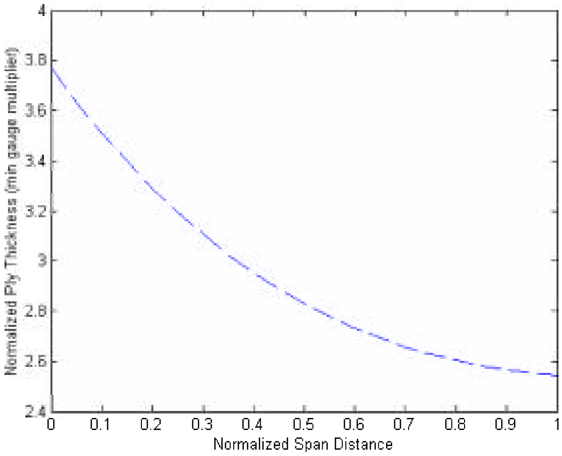

Thickness Distribution of 45.0 Degree Plies on the Outboard-Wing Ribs

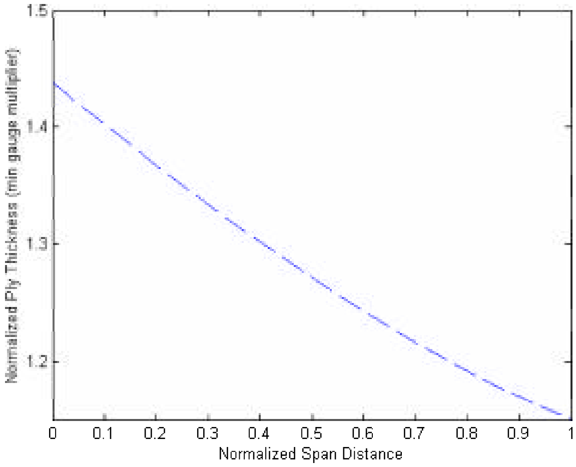

Thickness Distribution of 90.0 Degree Plies on the Outboard-Wing Ribs

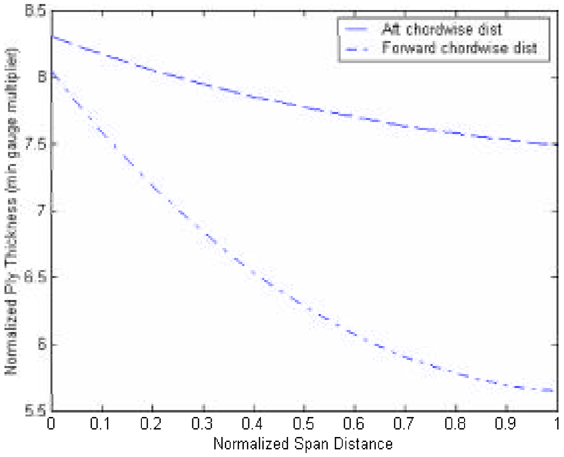

Thickness Distribution of 0.0 Degree Plies on the Outboard-Wing Spars

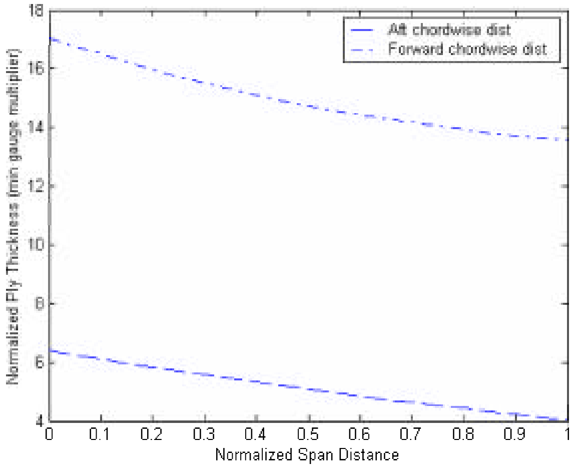

Thickness Distribution of 45.0 Degree Plies on the Outboard-Wing Spars

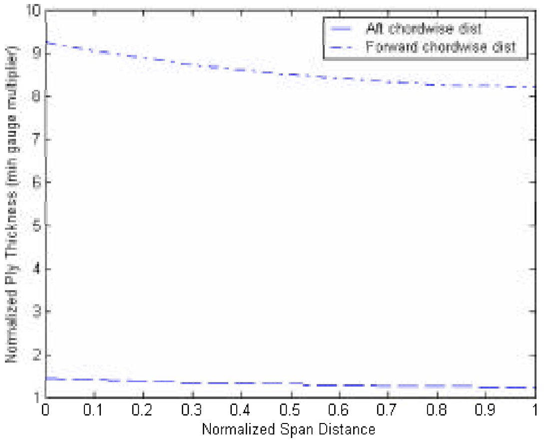

Thickness Distribution of 90.0 Degree Plies on the Outboard-Wing Spars

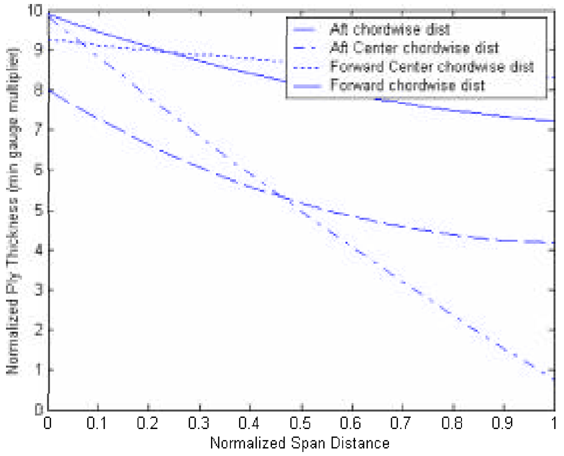

Thickness Distribution of 0.0 Degree Plies on the Outboard-Wing Top Skins

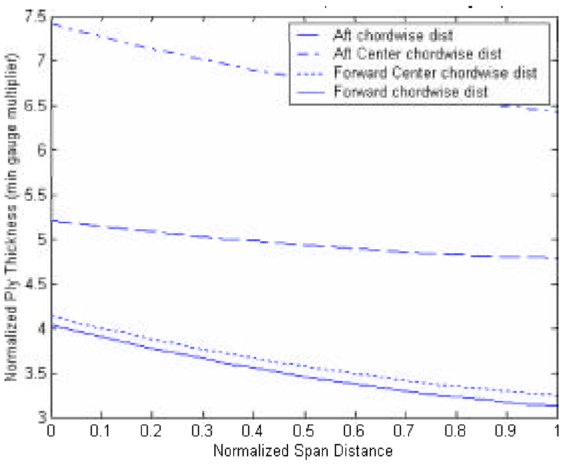

Thickness Distribution of 45.0 Degree Plies on the Outboard-Wing Top Skins

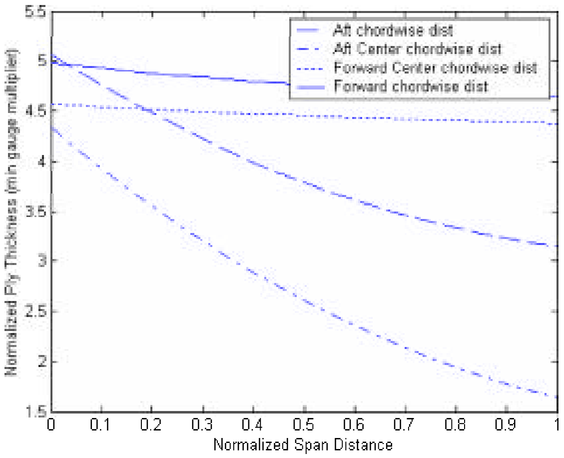

Thickness Distribution of 90.0 Degree Plies on the Outboard-Wing Top Skins

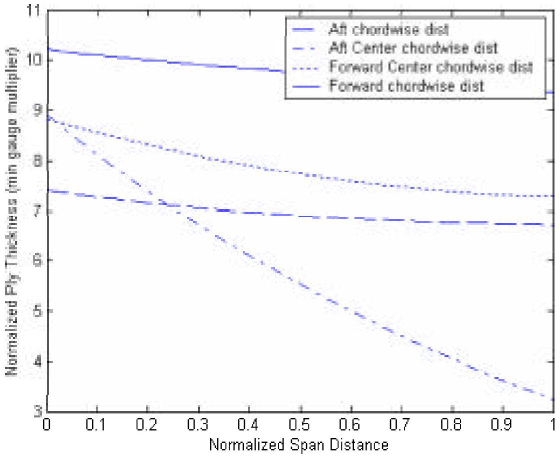

Thickness Distribution of 0.0 Degree Plies on the Outboard-Wing Bottom Skins

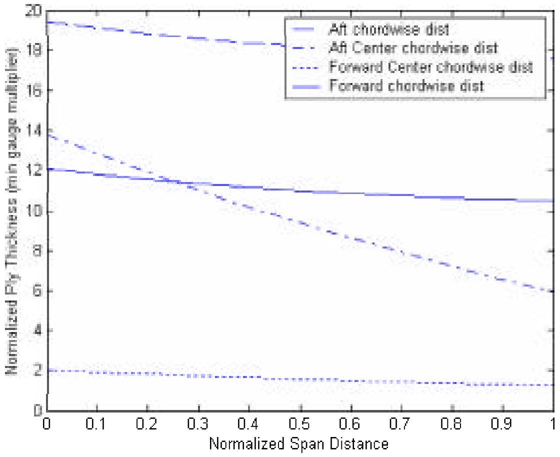

Thickness Distribution of 45.0 Degree Plies on the Outboard-Wing Bottom Skins

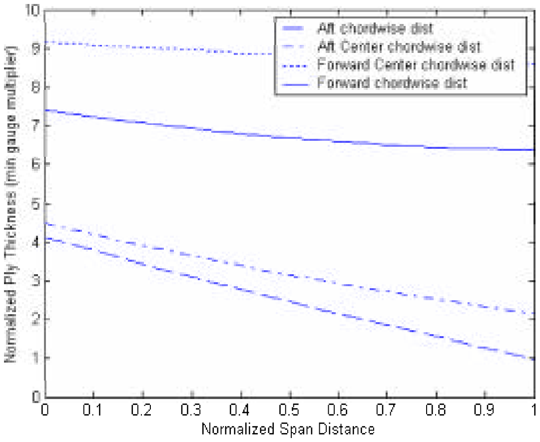

Thickness Distribution of 90.0 Degree Plies on the Outboard-Wing Bottom Skins

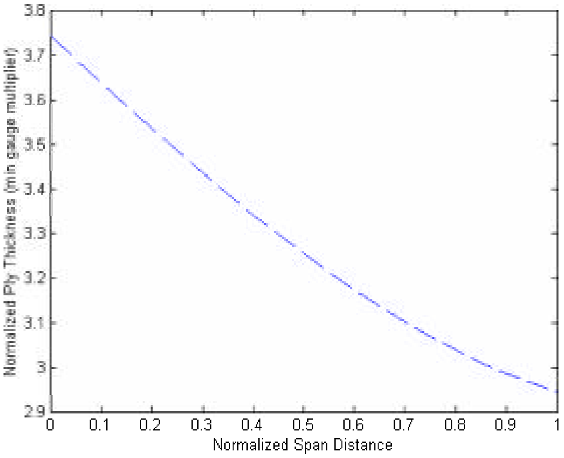

Thickness Distribution of 0.0 Degree Plies on the Joint-Wing Ribs

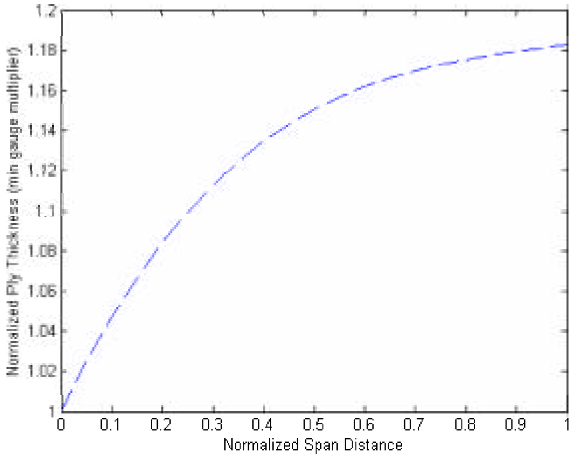

Thickness Distribution of 45.0 Degree Plies on the Joint-Wing Ribs

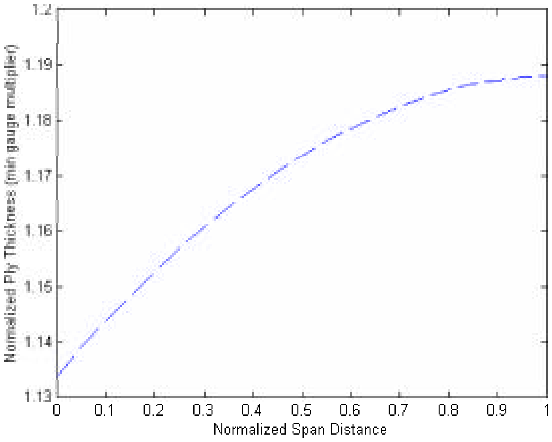

Thickness Distribution of 90.0 Degree Plies on the Joint-Wing Ribs

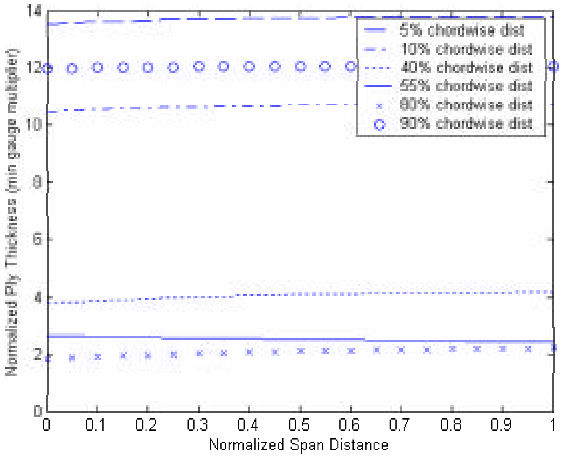

Thickness Distribution of 0.0 Degree Plies on the Joint-Wing Spars

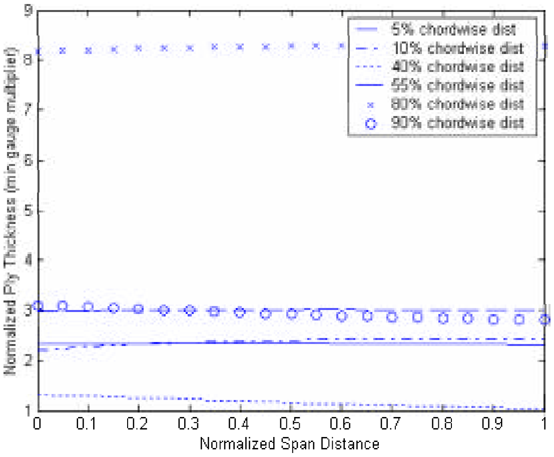

Thickness Distribution of 45.0 Degree Plies on the Joint-Wing Spars

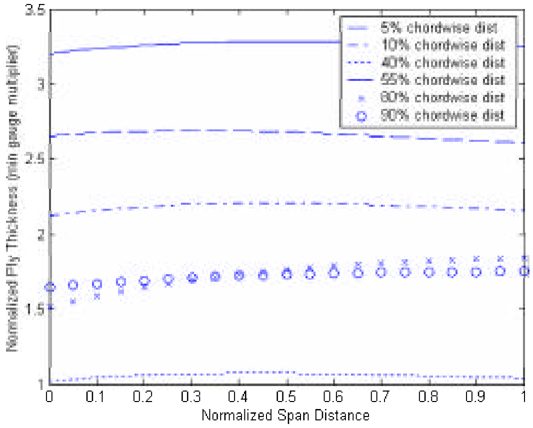

Thickness Distribution of 90.0 Degree Plies on the Joint-Wing Spars

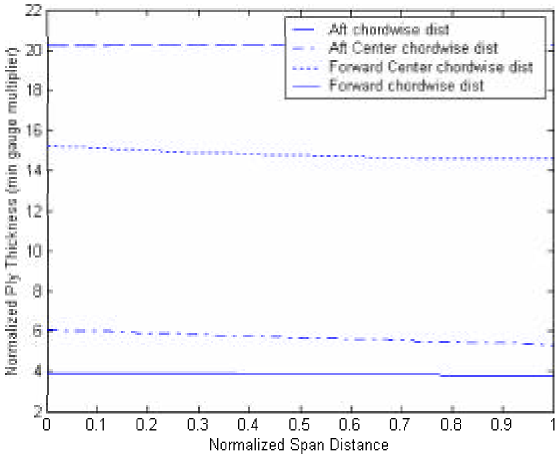

Thickness Distribution of 0.0 Degree Plies on the Joint-Wing Top Skins

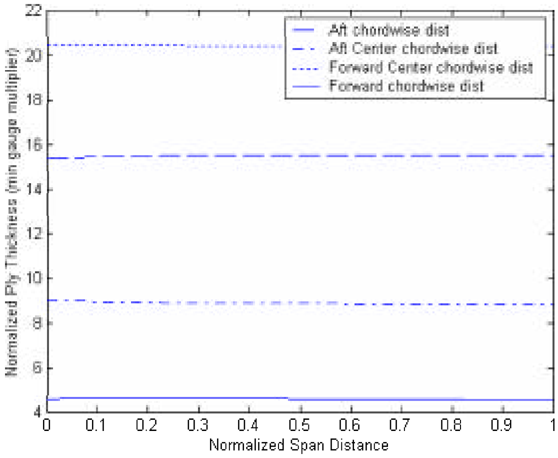

Thickness Distribution of 45.0 Degree Plies on the Joint-Wing Top Skins

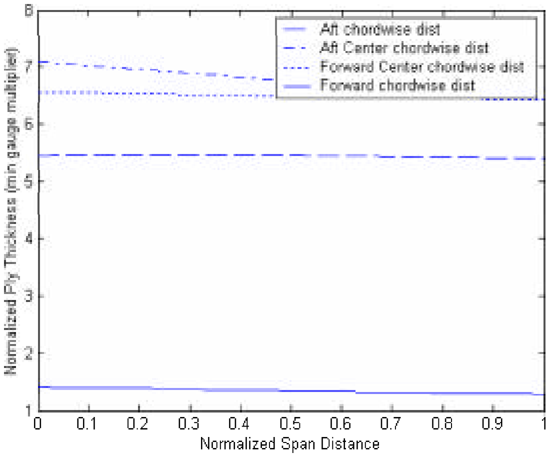

Thickness Distribution of 90.0 Degree Plies on the Joint-Wing Top Skins

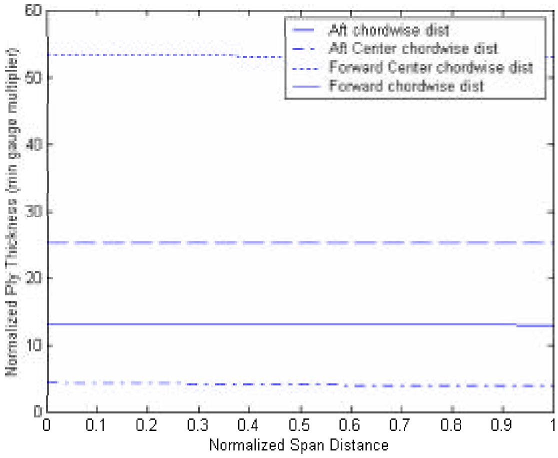

Thickness Distribution of 0.0 Degree Plies on the Joint-Wing Bottom Skins

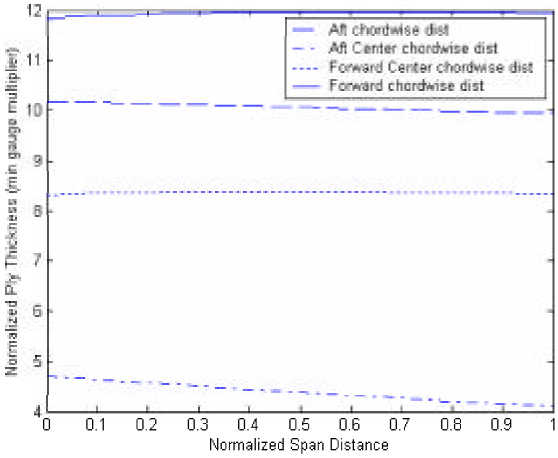

Thickness Distribution of 45.0 Degree Plies on the Joint-Wing Bottom Skins

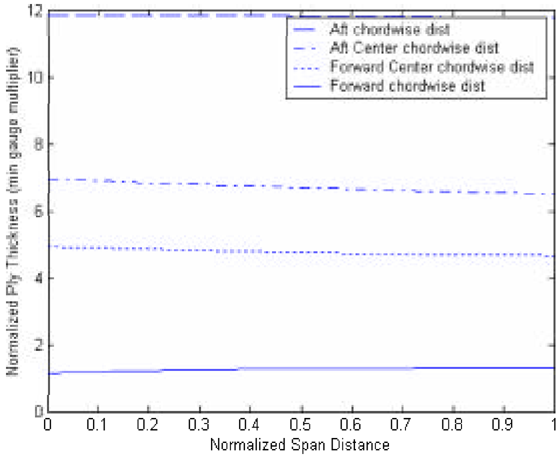

Thickness Distribution of 90.0 Degree Plies on the Joint-Wing Bottom Skins

Appendix D. Contour Thickness Distributions for Lowest Observed Configuration

The following contour plots show the total thickness distributions on the top and bottom skins of the lowest observed configuration. The contour plots account for all composite plies of Graphite/Epoxy, Astroquartz, and Carbon foam material.

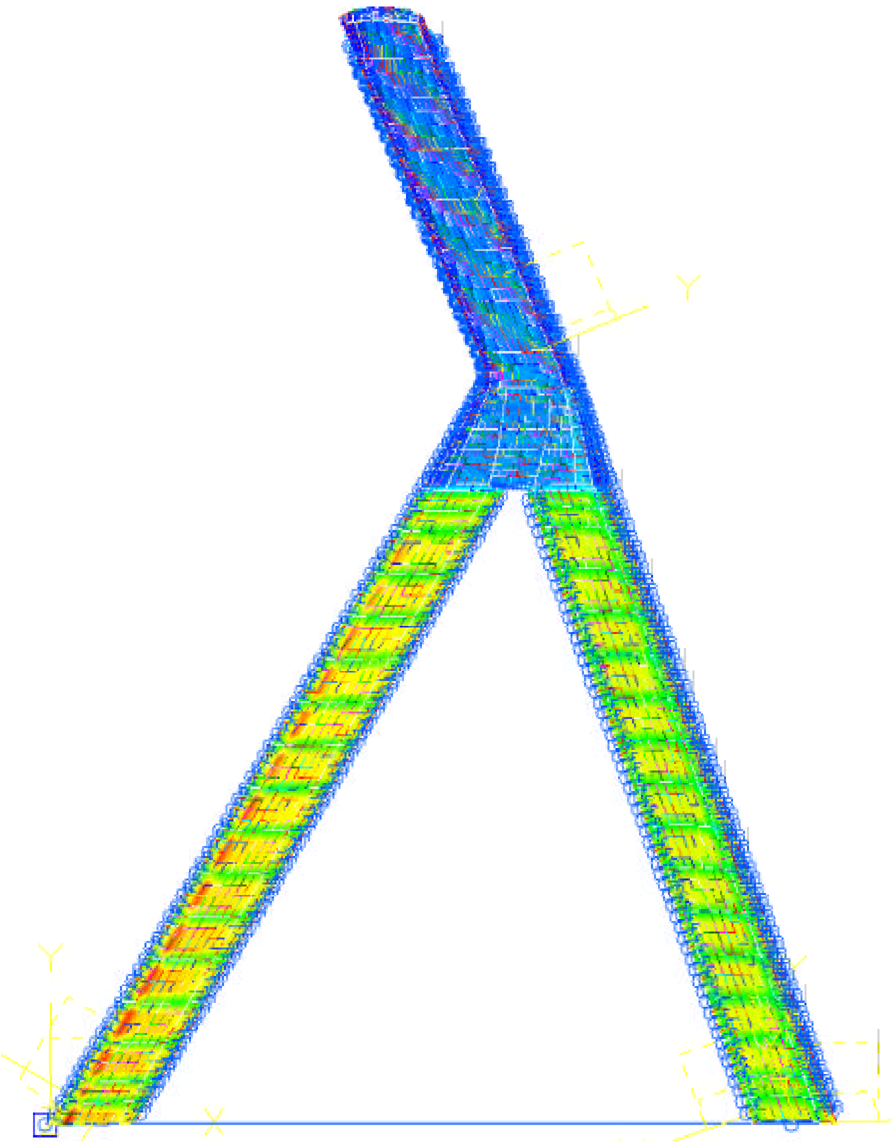

Contour Plot of Total Thickness Distributions on Lowest Observed Weight Configuration (Top View)

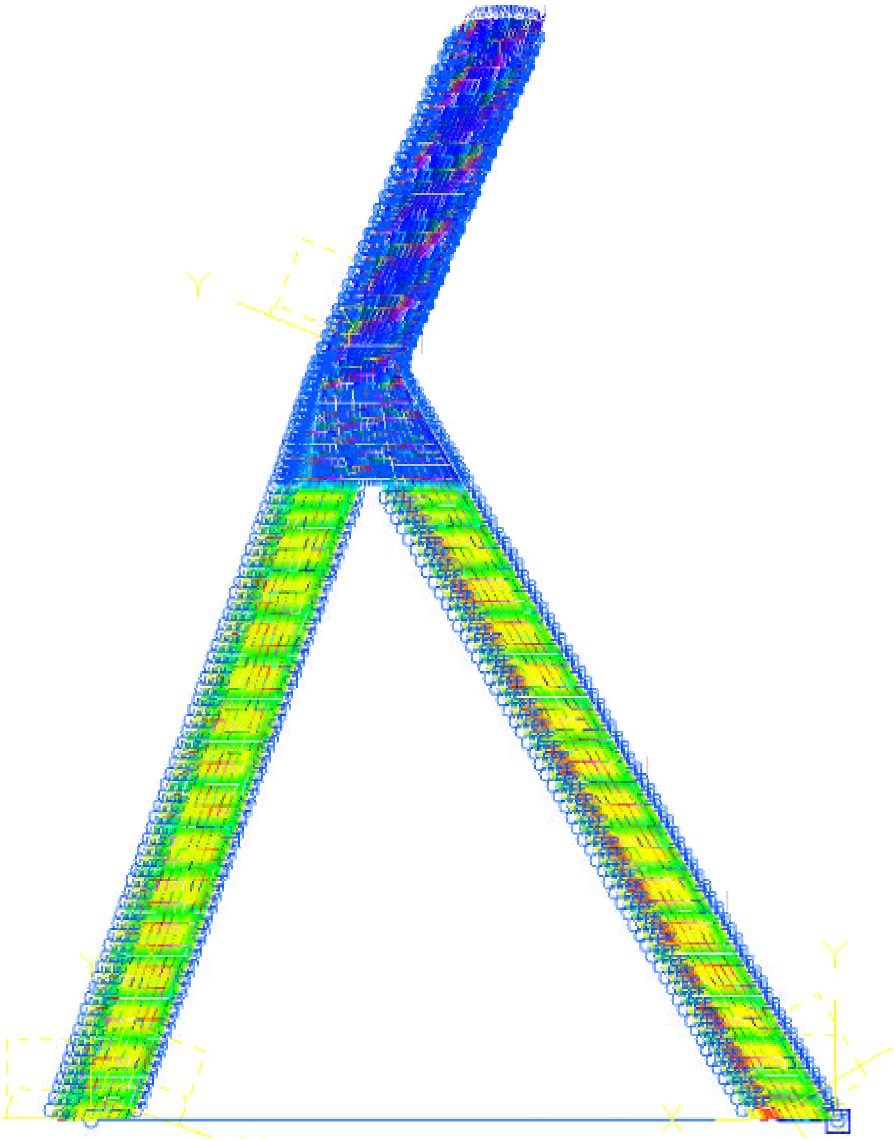

Contour Plot of Total Thickness Distributions on Lowest Observed Weight Configuration (Bottom View)

Appendix E. Tabulation of All Single Configuration Weights

		Joined-Wing
#	File Name	Weight
0	zzzzzz	13277.870
1	llzzzz	4627.078
2	luzzzz	5298.396
3	lzlzzz	2990.591
4	lzuzzz	6006.826
5	lzzlzz	3009.852
6	lzzuzz	8487.740
7	lzzzlz	3917.484
8	lzzzuz	4459.076
9	lzzzzl	4456.386
10	lzzzzu	4083.819
11	ulzzzz	51533.000
12	uuzzzz	50940.070
13	uzlzzz	49995.330
14	uzuzzz	41878.000
15	uzzlzz	42197.550
16	uzzuzz	72039.100
17	uzzzlz	44836.160
18	uzzzuz	47999.010
19	uzzzzl	9271.360
20	uzzzzu	40661.310
21	zllzzz	9186.990
22	zluzzz	28717.560
23	zlzlzz	3207.147
24	zlzuzz	52052.300
25	zlzzlz	16027.490
26	zlzzuz	9068.510
27	zlzzzl	13283.190
28	zlzzzu	13302.910
29	zulzzz	12369.060
30	zuuzzz	48364.520
31	zuzlzz	3914.610
32	zuzuzz	86223.930
33	zuzzlz	8576.310
34	zuzzuz	10704.470
35	zuzzzl	9063.760
36	zuzzzu	10323.070
37	zzllzz	4161.304
38	zzluzz	60989.590
39	zzlzlz	9778.680
40	zzlzuz	8224.830
41	zzlzzl	9756.560
42	zzlzzu	8731.650
43	zzulzz	5165.568
44	zzuuzz	121973.800
45	zzuzlz	28661.980
46	zzuzuz	34096.280
47	zzuzzl	45611.410
48	zzuzzu	41371.630
49	zzzllz	3772.972
50	zzzluz	4118.725
51	zzzlzl	4131.617
52	zzzlzu	3171.184
53	zzzulz	62375.370
54	zzzuuz	61246.080
55	zzzuzl	57423.850
56	zzzuzl	60887.540
57	zzzzll	23095.580
58	zzzzlu	12848.540
59	zzzzul	12794.470
60	zzzzuu	10913.380
61	uzzzzz	38543.640
62	lzzzzz	5680.998
63	zuzzzz	17072.400
64	zlzzzz	13711.440
65	zzuzzz	38242.520
66	zzlzzz	8078.680
67	zzzuzz	78024.710
68	zzzlzz	4204.043
69	zzzzuz	11067.020
70	zzzzlz	17142.400
71	zzzzzu	11296.750
72	zzzzzl	14792.130
73	optimal 1	4011.696
74	optimal 2	2913.161
75	optimal 3	4363.225
99	baseline	6023.981

Bibliography

1. Blair, M. and R. Canfield. “A Joined–Wing Structural Weight Modeling Study.” Number AIAA-2002-1337. Denver, CO: 43rd AIAA/ASME/ASCE/AHS/ASC Structure, Structural Dynamics and Materials Conference, April 2002.
2. Cook, R. *Concepts and Applications of Finite Element Analysis* (4th Edition). John Wiley and Sons, Inc., 2002.
3. Gallman, J. and I. Kroo. “Structural Optimization for Joined-Wing Synthesis,” *Journal of Aircraft*, *33*(1):214–223 (January–February 1996).
4. Lan, C.T. and J. Roskam. *Airplane Aerodynamics and Performace* (2nd Edition). Washington DC: American Institute of Aeronatautics and Astronautics, Inc., 1992.
5. Lee, D.H. “Aeroelastic Tailoring and Structural Optimization of Joined-Wing Configurations.” Briefing, July 2001.
6. Lee, D.H. and Chen P.C. “Nonlinear Aeroelastic Studies on a Joined-Wing with Wing Buckling Effects.” Number AIAA-2004-1944. Palm Springs, CA: 45th AIAA/ASME/ASCE/AHS/ASC Structure, Structural Dynamics and Materials Conference, April 2004.
7. Lin, H.H. Jhou J. and Stearman R. “Influence of Joint Fixiti on the Aeroelastic Characteristics of a Joined-Wing Structure.” Number AIAA-90-0980. 1442–1454. Long Beach, CA: 31st AIAA/ASME/ASCE/AHS/ASC Structure, Structural Dynamics and Materials Conference, April 1990.
8. Livne, E. “Aeroelasticity of Joined-Wing Airplane Configurations: Past Work and Future Challenges–A Survey.” Number AIAA-2001-1370. Seattle, WA: 42nd AIAA/ASME/ASCE/AHS/ASC Structure, Structural Dynamics and Materials Conference, April 2001.
9. The MathWorks Inc. *MATLAB Reference Guide: Version 6.1*, 2001.
10. Moore, G. *MSC/NASTRAN Design Sensitivity and Optimization.* The MacNeal Schwendler Corporation, 1994.
11. Myers, R. and D. Montgomery. *Response Surface Methodology* (2nd Edition). John Wiley and Sons, Inc., 2002.
12. Nangia, R.K. and M.E. Palmer. “Unconventional High Aspect Ratio Joined-Wing Aircraft with Aft and Forward Swept Wing-Tips.” Number AIAA-2003-0506. Reno, NV: 41st AIAA Aerospace Sciences Meeting and Exhibit, January 2003.

13. Nelson, R. *Flight Stability and Automatic Control* (2nd Edition). McGraw Hill, 1998.

14. Patil, M. "Nonlinear Aeroelastic Analysis of Joined-Wing Aircraft." Number AIAA-2003-1487. Norfolk, VA: 44th AIAA/ASME/ASCE/AHS/ASC Structure, Structural Dynamics and Materials Conference, April 2003.

15. Roberts, R. *Sensor-Craft Analytical Certification.* MS thesis, Graduate School of Engineering, Air Force Institute of Technology (AETC), Wright-Patterson AFB OH, March 2003. AFIT/GAE/ENY/03-06.

16. Rodden, W. and E. Johnson. *MSC/NASTRAN Aeroelastic Analysis.* The MacNeal-Schwendler Corporation, 1994.

17. Sang, L. *MSC/NASTRAN Handbook for Nonlinear Analysis.* The MacNeal-Schwendler Corporation, 1992.

18. Sigmon, K. and T. Davis. *MATLAB Primer: Sixth Edition.* Chapman and Hall/CRC, 2002.

19. Smallwood, B. *Structurally Integrated Antennas on a Joined-Wing Aircraft.* MS thesis, Graduate School of Engineering, Air Force Institute of Technology (AETC), Wright-Patterson AFB OH, March 2003. AFIT/GAE/ENY/03-07.

20. Smith, S.C. Cliff S.E. and I.M. Kroo. "The Design of a Joined-Wing Flight Demonstrator Aircraft." Number AIAA-87-2930. St. Louis, MO: AIAA/AHS/ASEE Aircraft Design, Systems and Operations Meeting, September 1987.

21. TechnoSoft Incorporated. *Adaptive Modeling Language Basic Training Manual: Version 2.07*, 2001.

22. VMA Engineering. *DOT Users Manual*, 1993.

23. Weisshaar, T. and D.H. Lee. "Aeroelastic Tailoring of Joined-Wing Configurations." Number AIAA-2002-1207. Denver, CO: 43rd AIAA/ASME/ASCE/AHS/ASC Structure, Structural Dynamics and Materials Conference, April 2002.

24. Wolkovich, J. "The Joined Wing: An Overview," *Journal of Aircraft*, *23*(3):161–178 (1986).

Vita

Captain Cody C Rasmussen graduated from Cottonwood High School in Salt Lake City, Utah. He entered undergraduate studies at the United States Air Force Academy, Colorado where he graduated with a Bachelor of Science degree in Engineering Mechanics and was commissioned in the United States Air Force in June 1999.

He was stationed at Los Angeles Air Force Base immediately after being commissioned. He worked as a Mechanical Engineer in the Space-Based Laser Project Office under the command of the Space and Missile Systems Center. In August 2002, he entered the Graduate School of Engineering and Management, Air Force Institute of Technology.

REPORT DOCUMENTATION PAGE

Form Approved
OMB No. 074-0188

1. REPORT DATE *(DD-MM-YYYY)* 23 Mar 04	**2. REPORT TYPE** **Master's Thesis**	**3. DATES COVERED** *(From – To)* 4 Oct 02 – 23 Mar 04

4. TITLE AND SUBTITLE

OPTIMIZATION PROCESS FOR CONFIGURATION OF FLEXIBLE JOINED-WING

5a. CONTRACT NUMBER

5b. GRANT NUMBER

5c. PROGRAM ELEMENT NUMBER

6. AUTHOR(S)

Rasmussen, Cody C, Captain, USAF

5d. PROJECT NUMBER

5e. TASK NUMBER

5f. WORK UNIT NUMBER

7. PERFORMING ORGANIZATION NAMES(S) AND ADDRESS(S)

Air Force Institute of Technology
Graduate School of Engineering and Management (AFIT/EN)
2950 Hobson Way
WPAFB OH 45433-7765

8. PERFORMING ORGANIZATION REPORT NUMBER

AFIT/GAE/ENY/04-M14

9. SPONSORING/MONITORING AGENCY NAME(S) AND ADDRESS(ES)

AFOSR/NM
Attn: Dr. Fariba Fahroo
4015 Wilson Blvd, Room 817-A
Arlington, VA 22203-1954 DSN: 426-8429

AFRL/VASD
Attn: Dr. Maxwell Blair
2210 Eighth Street, Room 220
WPAFB, OH 45433-7531 Comm : (937)255-8430

10. SPONSOR/MONITOR'S ACRONYM(S)

11. SPONSOR/MONITOR'S REPORT NUMBER(S)

12. DISTRIBUTION/AVAILABILITY STATEMENT

APPROVED FOR PUBLIC RELEASE; DISTRIBUTION UNLIMITED.

13. SUPPLEMENTARY NOTES

14. ABSTRACT

This study established a weight optimized configuration design of a joined-wing sensor-craft. The joined-wing aircraft concept fulfills a proposed long-endurance surveillance mission that contains an antenna structure embedded in the wing skin. The analysis was completed utilizing structural optimization, aerodynamic analyses, and response surface methodology. A sample of 74 joined-wing configurations were weight optimized. Each optimized structure was determined through a change of skin, spar, and rib thickness in the wing box by determining trimmed maneuver and gust conditions for critical flight mission points. Since the joined-wing concept has non-linear deformation characteristics, the structural optimization used both strain and buckling limits. The collection of the optimized data points was combined to create a response surface to predict the best joined-wing geometric configuration. Each configuration varied one of six key geometric variables. The geometric configuration variables included front wing sweep, aft wing sweep, outboard wing sweep, joint location, vertical offset, and thickness to chord ratio.

15. SUBJECT TERMS

Sensor-Craft, Joined-Wing, Gradient-Based Design, Non-Linear Analysis, Response Surface, Configuration Design, Multi-Discipline Optimization

16. SECURITY CLASSIFICATION OF:			**17. LIMITATION OF ABSTRACT**	**18. NUMBER OF PAGES**	**19a. NAME OF RESPONSIBLE PERSON**
					Canfield, Robert A., Lieutenant Colonel, USAF
REPORT U	**ABSTRACT** U	**c. THIS PAGE** U	UU	142	**19b. TELEPHONE NUMBER** *(Include area code)* (937) 255-3636; e-mail: robert.canfield@afit.edu